UNIVERSITÀ DEGLI STUDI DI PARMA
DIPARTIMENTO DI INGEGNERIA DELL'INFORMAZIONE
PARMA (I) - VIALE G.P. USBERTI
TEL. 0521-905800 • FAX 0521-905758

Dottorato di Ricerca in Tecnologie dell'Informazione
XX Ciclo

Matteo Foroni

FANTASIES USING OPTICAL FIBERS

Dissertazione presentata per il conseguimento
del titolo di Dottore di Ricerca

Gennaio 2008

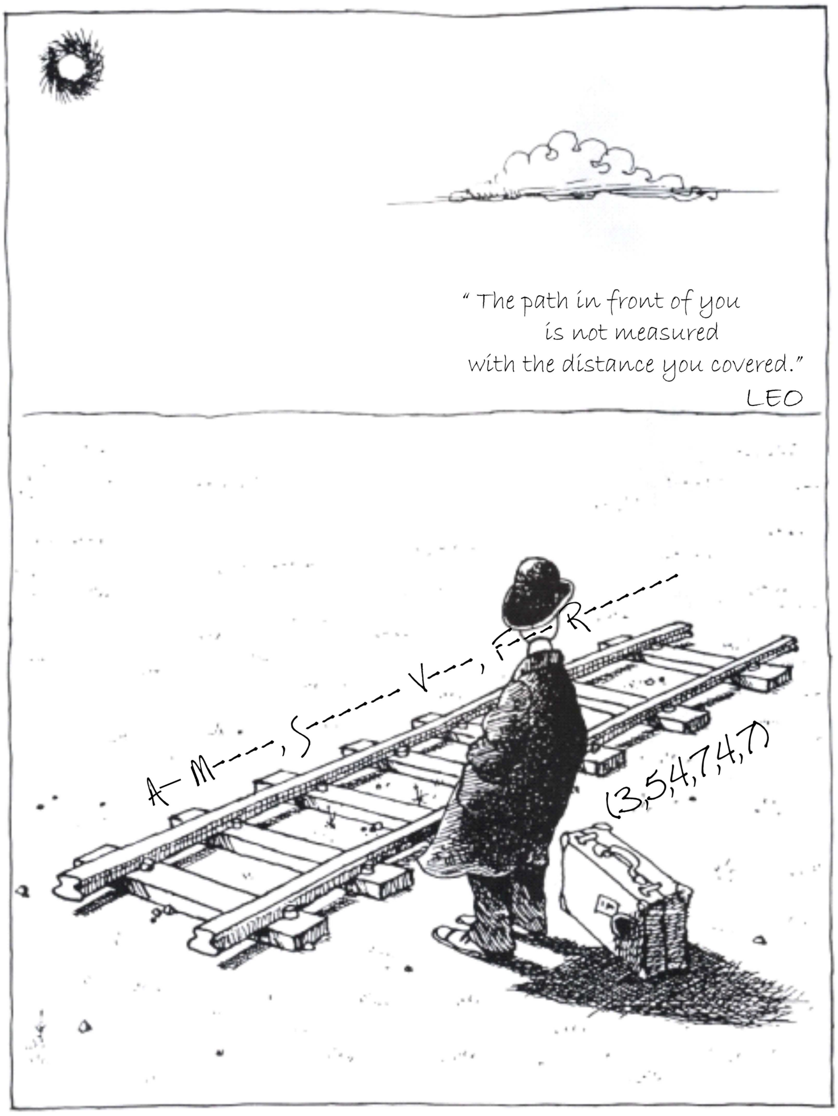
" The path in front of you
is not measured
with the distance you covered."
LEO
A– M-----, S-------- V---, F--- R-------
(3,5,4,7,4,7)

Contents

Introduction

The optical fiber invention has been one of the most noticeable technological breakthroughs in the recent history. In fact, optical fibers have steadily replaced copper wires and satellite links in the telecommunication systems industry and, along with the development of microelectronics and of advanced IT software, have laid the foundations for the information society. Since the first low-loss single-mode waveguides in 1970, after 30 years of intensive research, incremental steps have refined the fabrication technology and the optical fiber performances nearly as far as they can go. Now it is the time of *fantasy*. In fact, innovative optical fibers with unusual geometric and dielectric properties, like photonic crystal fibers or erbium-doped depressed-cladding fibers, as well as unconventional way to exploit the advantages offered by these lightguides, like in sensors or industrial applications, have been proposed.

The recent introduction of *fantasy* in the cross-section profile of optical fibers has provided researchers with new possibilities to harness light and to tailor its properties. In particular, Photonic Crystal Fibers (PCFs), which have been first demonstrated in 1995, are optical fibers with a periodic arrangement of a low-index material in a background one with higher refractive index. The background material in PCFs is usually undoped silica and the low index region is typically provided by air-holes running along their entire length. Two main categories of PCFs exist, that is high-index guiding fibers and low-index guiding ones. PCFs belonging to the first category are more similar to conventional optical fibers, because light is confined in a solid core by exploiting the modified total internal reflection mechanism. In fact, there is a positive refractive index difference between the core region and the photonic crystal cladding, where the air-hole presence causes a lower average refractive index. The guiding mechanism is defined as "modified" because the cladding refractive index is not a constant value, as in standard optical fibers, but it changes significantly with the wavelength. This characteristic, as well as the high refractive index contrast between silica and air, provides a range of new interesting features. Moreover, a high design flexibility is one of the distinctive properties of PCFs. In particular, by changing the geometric characteristics of the air-holes in the fiber cross-section, that is their dimension and/or position, it is possible to obtain PCFs with diametrically opposite properties. On the contrary, when the PCF core region has a lower refractive index than the surrounding photonic crystal cladding, light is guided by a mechanism different from total internal reflection, that is by exploiting the presence of the photonic bandgap (PBG) in the cladding. In fact, the air-hole microstructure which constitutes the PCF cladding is a two-dimensional photonic crystal, that is a material with periodic dielectric properties characterized by a PBG, where light in certain wavelength ranges can not propagate. In PCFs with a low index core, created by introducing a defect in the photonic crystal structure, for example an extra air-hole or an enlarged one, light is confined because the PBG effect makes propagation in the microstructured cladding region impossible. This guiding mechanism can not be obtained in conventional optical fibers and it opens a whole new set of interesting possibilities. In particular, light can be guided in a hollow core, thus providing numerous promising applications, such as low-loss guidance and high power delivery, without the risk of fiber damage. Moreover, air-guiding PCFs are almost insensitive to bending, even for small bending diameter values, and they present extreme dispersion properties, highly dominated by the waveguide component. Finally, when filled with proper gases or liquids, hollow-core PCFs can be successfully employed in sensor applications or for nonlinear optics.

The same *fantasy* used to invent the PCFs has been exploited to realize optical fibers with a depressed-cladding, or W profile, which traditionally provides particular dispersion properties, and an erbium-doped core for the amplification of signals in an unconventional band with respect to the well-established erbium-doped fiber amplifiers (EDFAs). A fiber with a depressed-cladding structure consists of a core, an inner cladding and an outer one. The inner cladding is the region with the lower refractive index in the fiber cross-section. These particular transverse section characteristics provide some interesting properties with respect to conventional fibers. In fact, W fibers can be designed to have anomalous dispersion in the single-mode wavelength range and single-mode operation can be maintained even with a relatively large core size. Moreover, in the single-mode regime the W fiber fundamental mode is more tightly confined within the core, in comparison with standard single-mode fibers. Another important characteristic is that W fibers can be designed such that the fundamental mode of the fiber experiences a non-zero cutoff wavelength. When this occurs, the mode field is no longer truly guided and its loss significantly increases. This characteristic of W fiber can be successfully combined with the amplification properties of erbium, thus obtaining EDFAs for S band, 1450 $nm \div 1530\ nm$, with good performances. In fact, in depressed-cladding erbium-doped fibers the amplified spontaneous emission in the C band can be properly suppressed by exploiting the fiber bending losses.

Fantasy is the only limit also to the possible applications of optical fiber lasers and amplifiers. In particular, for high power applications, like material processing, micro-machining, cutting, scribing, marking, welding, and so on, the industry has focused on the development of lasers and amplifiers based on fibers doped with Ytterbium (Yb), which offers several unique advantages with respect to other rare-earth elements. More specifically, ytterbium-doped fibers offer high output powers tunable over a broad range of wavelengths, from around 975 to 1200 nm. Moreover, ytterbium-doped fiber lasers and amplifiers are characterized by a high electrical to optical conversion efficiencies, low thermal load, reliable fiber geometry and ability to provide high gains. Research on such laser systems is progressing rapidly in continuous-wave format, as well as in pulsed configurations. The achievements so far obtained might give the impression that Yb-doped fiber laser and amplifier technology has reached a high level of maturity and that constructing systems is a straightforward process. However, it is to be appreciated that Yb-doped fiber lasers and amplifiers are quite difficult to design and optimize in practice. In fact, recently these lasers and amplifiers have progressively replaced mechanical and electrical tools in different applications, so these devices have permanently to be improved and adapted to new requirements. Naturally, also cost- and energy-efficiency are of highest priority. As a consequence, cascaded fiber amplifier chains are frequently used to amplify the output from a well-conditioned seed laser to high average powers. In these circumstances, the Yb-doped fiber amplifiers consists basically of a first module with one or more pre-amplifier stages with a short length of a single-mode single-cladding Yb-doped fiber, and then a booster stage.

Another figment in optical fiber context concerns the development of Plastic Optical Fibers (POFs), which are made out of plastic. Traditionally Poly-Methyl-Methacrylate (PMMA) is the core material, and fluorinated polymers are the cladding material. As in glass-based fibers, light is transmitted through the POF core, whose size is, in some cases, 100 times larger with respect to the one of conventional silica fibers. For this reason and for the high value of the numerical aperture, light coupling into the POF core is extremely easy. Moreover, these fibers can be simply connected to optical devices, like light emitting diodes or photodiodes, and can be employed in low cost systems, due to the inexpensive opto-electronic components and low tolerance plastic connectors which can be used. The POF main drawback with respect to silica optical fibers is the high attenuation, which is typically 200 dB/km at 650 nm for POFs with a PMMA core. The traditional PMMA fibers are commonly used for low-speed, short-distance applications in digital home appliances, home networks, industrial networks, and car networks. However, the advantages offered by POFs can be successfully exploited also in sensing applications to measure different kinds of parameters, like temperature, pressure, distance, refractive index, and so on.

The activity carried out during the PhD course and described in the present thesis has concerned special optical fibers with particular refractive index profiles, from PCFs to POFs, which is a research topic in continuous evolution and characterized by a great scientific excitement. The aim of the research of the three year PhD course has been to accurately study, and thus to deeply understand the light guiding mechanisms exploited in these kinds of optical fibers. The unusual guiding properties of PCFs with different air-hole arrangements in the fiber cross-section have been investigated both numerically, through a full-vector modal solver based on the FEM, and experimentally, by considering samples of large mode area PCFs, as well as of nonlinear fibers. Moreover, the properties of Erbium-Doped Fibers (EDFs) with a particular refractive index profile, that is with a depressed-cladding, have been experimentally characterized. By exploiting the bending loss of these active fibers, amplifiers with different configurations have been realized, which cover larger bandwidths with respect to conventional ones, as well as tunable lasers in S, C and L band. Then, in order to design and realize the pre-amplifier stage for a pulsed high power laser useful for industrial applications, single-mode ytterbium-doped fibers with different doping concentrations, with either a single or a double-cladding, have been considered with the aim to optimize the gain performances. Finally, low cost sensors based on the inexpensive plastic fibers have been proposed as an effective solution to the problem of the liquid level measurement. Sensors for both point and continuous measurements of the liquid level, which can be also exploited to distinguish fluids according to their refractive index.

The thesis is organized in five Chapters, as it follows. Chapter 1 is a general presentation of the PCF innovative characteristics. Starting from the description of the properties of photonic crystals, materials with a refractive index periodic distribution, the passage from conventional optical fibers to photonic crystal ones is explained. After describing the two light guiding mechanisms exploited in PCFs, the advantages offered by this new fiber type with respect to the conventional ones are discussed. Then, some meaningful examples of PCFs with unusual guiding, dispersion and nonlinear properties, proposed in literature and successfully used in many applications, are reported. Moreover, the different loss mechanisms are presented for both solid- and hollow-core PCFs, since attenuation is still the main drawback which affects this new kind of optical fibers. A significant loss reduction can be obtained by improving the fabrication process of PCFs, reported in the final part of the first Chapter.

Chapter 2 summarizes the results concerning the PCF guiding properties, which derive directly from the complex propagation constant of the guided modes. First of all, the modal cut-off analysis of a new kind of PCFs, with a square lattice of air-holes in a silica matrix, is reported. It is important to underline that this study, already reported in literature for triangular PCFs, has been done for the first time for fibers with a square lattice of air-holes. The same method has been successfully applied to study the single-mode regime of a new kind of triangular PCFs, which have a wide silica core and a large modal area. In fact, it is important to investigate the trade-off between the effective area and the cut-off of the fundamental guided mode, in order to successfully exploit these large mode area fibers in practical applications. The accuracy of the effective area values and of the guided mode field distribution numerically evaluated through the simulations has been checked by comparing the results obtained with the finite element method with those of the experimental measurements made with a Scanning Near-Field Optical Microscope (SNOM) for some samples of large mode area PCFs available in laboratory. As regards the experimental measurements, the spectral broadening of the fs pulses of a Ti:Sapphire laser into a short length of a nonlinear highly birefringent PCF made of silicate glass has been observed. In the final part of the Chapter the study of the guiding properties of realistic hollow-core Bragg fibers has been reported. The dispersion curves, the confinement loss spectra and the field distribution of the guided modes have been calculated, showing the significant influence of the silica bridges on the fundamental mode characteristics. Then, it has been deeply investigated how each geometric characteristic in the hollow-core Bragg fiber cross-section influences the fiber guiding properties, showing which parameter it is better to change in order to properly modify the values or the spectral behaviour of the losses. Finally, among the different possible applications, the feasibility of a DNA bio-sensor based on a hollow-core Bragg fiber has been demonstrated.

The study of Erbium-Doped Fiber Amplifiers (EDFAs), carried out as an important part of the PhD research activity, is described in Chapter 3. The bending loss of a depressed-cladding EDF, which has been deeply experimentally characterized, has been exploited to realize efficient EDFAs for S band in single pass configuration and in double pass one. The amplifier performances have been measured by changing the signal input power,the pump power, the fiber bending diameter and the fiber length. Moreover, by combining in a new parallel scheme a S band amplifier and a C band one, both with a double pass configuration and realized with the same depressed-cladding EDF, bent with two different diameter values, an EDFA for S+C band has been demonstrated. By adding a L band module, a triple band all-silica EDFAs has been developed. In the second part of the Chapter, a tunable narrow-linewidth triple-wavelength EDF Ring Laser (EDFRL) has been experimentally demonstrated, where the bending losses of the depressed-cladding fiber have been exploited to tune the laser wavelength in S, C and L band. This tuning method has been also exploited to shift the wavelength of a single frequency EDFRL in S band

and in C band. Finally, a tunable single frequency S band depressed-cladding EDFRL, where the doped fiber has been used as the active medium, as well as the tunable filter, has been proposed and experimentally demonstrated.

An important part of the research activity, developed in the last part of the PhD course, concerns the design and the experimental realization of a pre-amplifier based on single-mode ytterbium-doped fibers, which will be employed for the pulse amplification at 1064 nm to high power levels in a master oscillator power amplifier, which has become more and more relevant in the last years for a lot of industrial applications. Chapter 4 is completely devoted to this topic. The output power of the two-stage pre-amplifier realized has been measured by considering different ytterbium-doped fibers and by changing the active fiber length and the pump power of single-mode grating-stabilized lasers at 976 nm, in order to optimize the gain performances. Measurement results regarding the performances of each stage and of the whole system are reported and discussed in the Chapter.

In the final Chapter of the thesis, that is the fifth, the possibility to exploit POFs for sensor applications is discussed. In particular, low cost POF-based sensors, which are simple, effective and inexpensive solutions to the problem of the liquid level measurements, are presented. An intrusive POF sensor based on the total internal reflection principle has been developed for point measurements of the liquid level. The liquid presence can be detected by evaluating the light back-reflected by a probe, realized with a POF tip-shaped at one end. A further study, described in the Chapter, has been performed on a non-intrusive POF sensor for continuous liquid level measurements. The solution proposed is based on a POF pair. One of the fiber is connected to a LED and transmits the light towards the liquid under test. The beam reaches the liquid surface, and it is reflected back, being collected by the second POF belonging to the pair and transmitted to a photodiode, where it is converted into an electronic signal. In the final part of the Chapter it is highlighted that the proposed sensor can be used also for refractive index measurements. In fact, liquids with a high refractive index presents also high value of the reflection coefficient and, as a consequence, their surface can better reflect the incident light.

A final Appendix reports some significant informations about the method used for all the numerical analyses reported in this thesis, that is the finite element method. This numerical method is particularly suitable to study the properties of fibers with any refractive index profile, as well as any geometry in the transverse section. In particular, a full-vector modal solver with proper boundary conditions has been exploited to calculate the guided mode complex propagation constant and the magnetic field distribution, which have been used as the starting point to evaluate all the parameters which characterize the optical fiber guiding properties.

Starting from the results of the PhD course simulation and experimental activities, related to the properties of specialty optical fibers, useful for amplification and sensing applications, conclusions will be drawn on *fantasy* with optical fibers, that is on the effectiveness of the innovative ideas and solutions proposed and discussed in the present thesis.

Chapter 1

Photonic crystal fibers

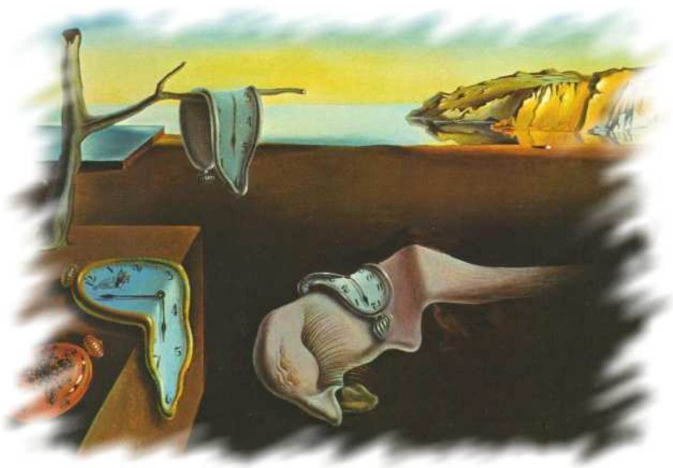

Photonic Crystal Fibers (PCFs), which represent a new kind of optical fibers with innovative properties, are widely described in this Chapter.

Starting from the description of the characteristics and the properties of photonic crystals, materials with a refractive index periodic distribution, the passage from conventional optical fibers to photonic crystal ones, introduced for the first time in 1995, is explained.

Then, the two light guiding mechanisms used in photonic crystal fibers are presented. In solid-core fibers, where light is confined in a higher refractive index region, modified total internal reflection is exploited, which is quite similar to the guiding mechanism in standard optical fibers. When the light is confined in a region with a refractive index lower than that of the surrounding area, as in hollow-core fibers, it is necessary the presence of the photonic bandgap to provide the light confinement.

One of the most important advantages offered by photonic crystal fibers is the high design flexibility. In fact, by changing the geometric characteristics of the fiber cross-section, such as the air-hole dimension or disposition, it is possible to obtain fibers with diametrically opposed properties. Photonic crystal fibers with unusual guiding, dispersion and nonlinear properties can be designed and successfully used in various applications, as reported in this Chapter.

The main drawback which affects this new kind of fibers is related to the attenuation, which is higher than that of conventional optical fibers. The different loss mechanisms are here analyzed for both solid- and hollow-core photonic crystal fibers.

A significant loss reduction can be obtained by improving the fabrication process of photonic crystal fibers, called stack-and-draw, reported in the final part of the Chapter.

1.1 From conventional optical fibers to PCFs

Optical fibers, which transmit information in the form of short optical pulses over long distances at exceptionally high speeds, are one of the major technological successes of the 20th century. This technology has developed at an incredible rate, from the first low-loss single-mode waveguides in 1970 to being key components of the sophisticated global telecommunication network. Optical fibers have also non-telecom applications, for example in beam delivery for medicine, machining and diagnostics, sensing and a lot of other fields. Modern optical fibers represent a careful trade-off between optical losses, optical nonlinearity, group velocity dispersion and polarization effects. After 30 years of intensive research, incremental steps have refined the capabilities of the system and the fabrication technology nearly as far as they can go.

The interest of researchers and engineers in several laboratories, since the 1980s, has been attracted by the ability to structure materials on the scale of the optical wavelength, that is a fraction of a micrometer or less, in order to develop new optical materials, known as photonic crystals. Photonic

Figure **1.1**: Photonic crystals in butterfly wings [3].

crystals rely on a regular morphological microstructure, incorporated into the material, which radically alters its optical properties [1]. They represent the extension of the results obtained for semiconductors into optics. In fact, the band structure of semiconductors is the outcome of the interactions between electrons and the periodic variations in potential created by the crystal lattice. By solving the Schrödinger's wave equation for a periodic potential, electron energy states separated by forbidden bands are obtained. Photonic bandgaps can be obtained in photonic crystals, where periodic variations in dielectric constant, that is in refractive index, substitute variations in electric potential, as well as the classical wave equation for the magnetic field replaces the Schrödinger's equation [2].

Photonic bandgap, originally predicted in 1987 by Sajeev John, from University of Toronto, and Eli Yablonovitch, from Bell Communications Research, has become the really hot topic in optics in the early 1990s. The idea was to build the right structures, in order to selectively block the transmission of photons with energy levels, that is wavelengths, corresponding to the photonic bandgaps, while allowing other wavelengths to pass freely. Moreover, slight variations in the refractive index periodicity would introduce new energy levels within the photonic bandgap, as it happens with the creation of energy levels within the bandgap of conventional semiconductors.

Unfortunately, building the right structures has proved extremely difficult. The first photonic bandgap material was created in 1991 by Yablonovitch and his colleagues by drilling holes with a diameter of 1 mm in a block of material with a refractive index of 3.6. Since the bandgap wavelength is of the order of the spacing between the air-holes in the photonic crystal, this structure had a

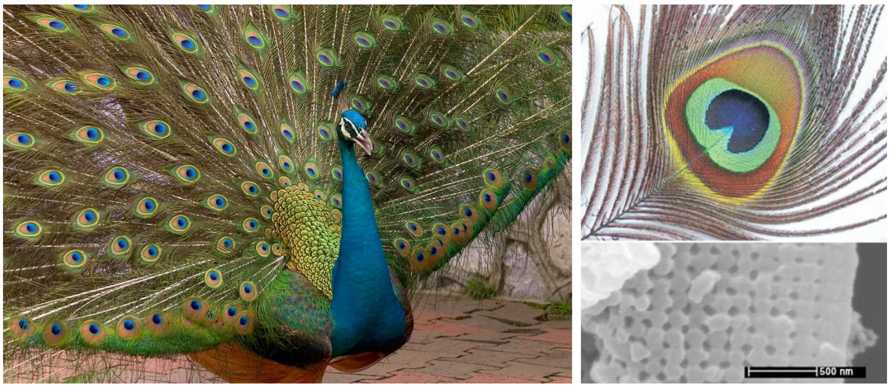

Figure **1.2**: Photonic crystals in peacock feathers [3].

bandgap in the microwave region.

In 1991 Philip Russell, who was interested in Yablonovitch's research, got his big "crazy" idea for "something different", during CLEO/QELS conference [2]. Russell's idea was that light could be trapped inside a fiber hollow-core by creating a two-dimensional photonic crystal in the cladding, that is a periodic wavelength-scale lattice of microscopic air-holes in the glass. The basic principle is the same which is the origin of the colour in butterfly wings and peacock feathers, reported in Fig. 1.1 and Fig. 1.2, that is all wavelength-scale periodic structures exhibit ranges of angle and colour, stop bands, where incident light is strongly reflected. When properly designed, the photonic crystal cladding, running along the entire fiber length, can prevent the escape of light from the hollow core. These new fibers are called photonic crystal fibers, since they rely on the unusual properties of photonic crystals.

The first fiber with a photonic crystal structure was reported by Russell and his colleagues in 1995. Even if it was a very interesting research development, the first PCF did not have a hollow core, as shown in Fig. 1.3, and, consequently, it did not rely on a photonic bandgap for optical confinement. In fact, in 1995 Russell's group could produce fiber with the necessary air-hole triangular lattice, but the air-holes were too small to achieve a large air-filling fraction, which is fundamental to realize a photonic bandgap. Measurements have shown that this solid-core fiber formed a waveguide that was single-mode, that is only the fundamental mode was transmitted, over a wide wavelength

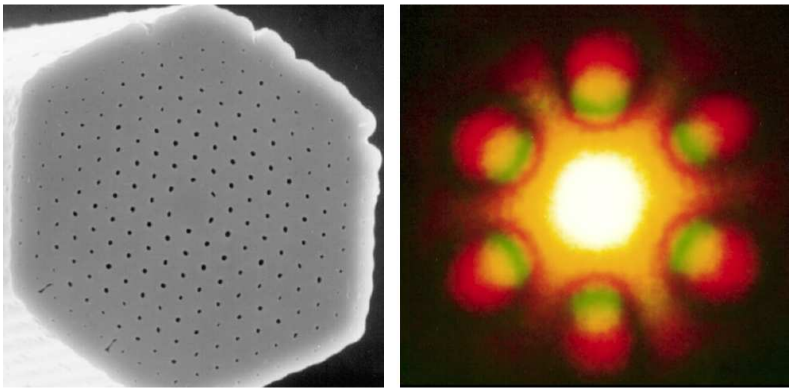

(a) (b)

Figure **1.3**: (a) Solid-core fiber with photonic crystal structure. The air-holes are 300 nm in diameter and spaced 2.3 μm apart. (b) Field pattern of the transmitted light [2].

range. Moreover, the first PCF had very low intrinsic losses, due to the absence of doping elements in the core, and a silica core with an area about ten times larger than that of a conventional Single-Mode Fiber (SMF), thus permitting a corresponding increase in optical power levels.

After moving his research group to the University of Bath in 1996, where PCF fabrication techniques were steadily refined, Russell and his co-workers were able to report, in 1999, the first single-mode hollow-core fiber, in which confinement was due by a full two-dimensional photonic bandgap, as reported in Fig. 1.4. They realized that the photonic bandgap guiding mechanism is very robust, since light remains well confined in the hollow core even if tight bends are formed in the fiber. However, it is highly sensitive to small fluctuations in the fiber geometry, for example to variations in the air-hole size.

Initial production techniques were directed simply at the task of making relatively short lengths of fiber in order to do the basic science, but many research teams are now working hard to optimize their PCF production techniques, in order to reduce the losses.

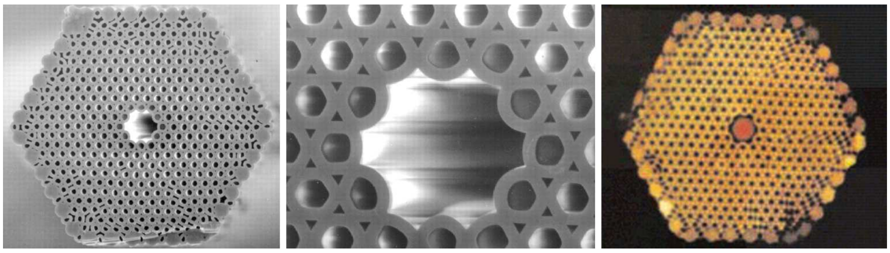

(a) (b) (c)

Figure **1.4**: Scanning electron micrograph of the (a) hollow-core PCF and (b) of its central region. The interhole spacing is 4.9 μm, and the core has a diameter of 14.8 μm. (c) Field pattern [2].

1.2 Guiding mechanisms

In order to form a guided mode in an optical fiber, it is necessary to introduce light into the core with a value of β, that is the component of the propagation constant along the fiber axis, which cannot propagate in the cladding. The highest β value that can exist in an infinite homogeneous medium with refractive index n is $\beta = nk_0$, being k_0 the free-space propagation constant. All the smaller values of β are allowed. A two-dimensional photonic crystal, like any other material, is characterized by a maximum value of β which can propagate. At a particular wavelength, this corresponds to the fundamental mode of an infinite slab of the material, and this β value defines the effective refractive index of the material.

1.2.1 Modified total internal reflection

It is possible to use a two-dimensional photonic crystal as a fiber cladding, by choosing a core material with a higher refractive index than the cladding effective index. An example of this kind of structures is the PCF with a silica solid core surrounded by a photonic crystal cladding with a triangular lattice of air-holes, shown in Fig. 1.5a. These fibers, also known as index-guiding PCFs, guide light through a form of Total Internal Reflection (TIR), called modified TIR. However, they have many different properties with respect to conventional optical fibers.

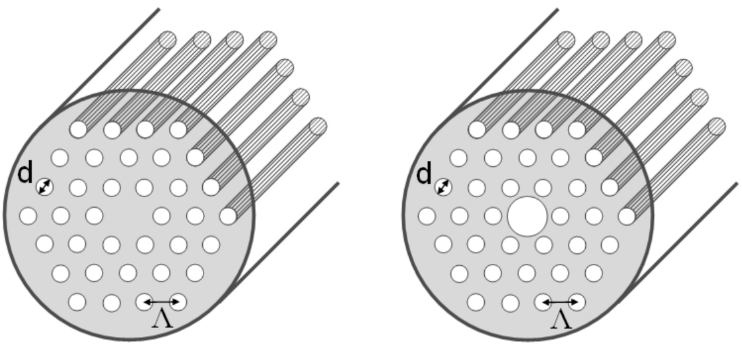

(a) (b)

Figure **1.5**: (a) Schematic of a solid-core PCF with a triangular lattice of air-holes, which guides light for modified total internal reflection. The air-hole diameter is d, while the hole-to-hole spacing, or pitch, is Λ [4]. (b) Schematic of a hollow-core PCF with a triangular lattice of air-holes, which guides light through the photonic bandgap effect [5].

Endlessly single-mode property

As already stated, the first solid-core PCF, shown in Fig. 1.3, which consisted of a triangular lattice of air-holes with a diameter d of about 300 nm and a hole-to-hole spacing Λ of 2.3 μm, did not ever seem to become multi-mode in the experiments, even for short wavelengths. In fact, the guided mode always had a single strong central lobe filling the core [6].

Russell has explained that this particular endlessly single-mode behaviour can be understood by viewing the air-hole lattice as a modal filter or “sieve” [6]. Since light is evanescent in air, the air-holes act like strong barriers, so they are the “wire mesh” of the sieve. The field of the fundamental mode, which fits into the silica core with a single lobe of diameter between zeros slightly equal to 2Λ, is the “grain of rice” which cannot escape through the wire mesh, being the silica gaps between the air-holes belonging to the first ring around the core too narrow. On the contrary, the lobe dimensions for the higher order modes are smaller, so they can slip between the gaps. When the ratio d/Λ, that is the air-filling fraction of the photonic crystal cladding, increases, successive higher order modes become trapped [6]. A proper geometry design of the fiber cross-section thus guarantees that only the fundamental mode is guided. More detailed studies of the properties of triangular PCFs have shown that this occurs for $d/\Lambda < 0.4$ [7, 8].

By exploiting this property, it it possible to design very large mode area fibers, which can be successfully employed for high-power delivery, amplifiers and lasers. Moreover, by doping the core in order to slightly reduce its refractive index, light guiding can be turned off completely at wavelengths shorter than a certain threshold value.

1.2.2 Photonic bandgap guidance

Optical fiber designs completely different form the traditional ones result from the fact that the photonic crystal cladding have gaps in the ranges of the supported modal index β/k_0 where there are no propagating modes. These are the photonic bandgaps of the crystal, which are similar to the two-dimensional bandgaps which characterize planar lightwave circuits, but in this case they have propagation with a non-zero value of β. It is important to underline that gaps can appear for values of modal index both greater and smaller than unity, enabling the formation of hollow-core fibers with bandgap material as a cladding, as reported in Fig. 1.5b. These fibers, which cannot be made using conventional optics, are related to Bragg fibers, since they do not rely on TIR to guide light. In fact, in order to guide light by TIR, it is necessary a lower-index cladding material surrounding the core, but there are no suitable low-loss materials with a lower refractive index than air at optical frequencies [1].

The first PCF which exploited the photonic bandgap effect to guide light was reported in 1998 [6, 9], and it is shown in Fig. 1.6. Notice that its core is formed by an additional air-hole in a honeycomb lattice. This PCF could only guide light in silica, that is in the higher-index material.

Hollow-core guidance had to wait until 1999, when the PCF fabrication technology had advanced to the point where larger air-filling fractions, required to achieve a photonic bandgap for air-guiding, became possible [6]. Notice that an air-guided mode must have $\beta/k_0 < 1$, since this condition guarantees that light is free to propagate and form a mode within the hollow core, while being unable to escape into the cladding. The first hollow-core PCF, reported in Fig. 1.4, had a simple triangular lattice of air-holes, and the core was formed by removing seven capillaries in the center of the fiber cross-section. By producing a relatively large core, the chances of finding a guided mode were improved. When white light is launched into the fiber core, coloured modes

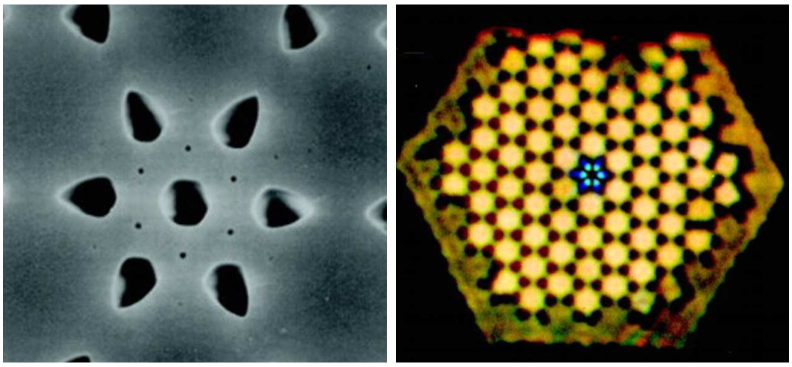

(a) (b)

Figure **1.6**: (a) SEM of the first photonic bandgap PCF. (b) Near-field of the six-leaved blue mode that appears when the fiber is excited by white light [6].

are transmitted, thus indicating that light guiding existed only in restricted wavelength ranges, which coincide with the photonic bandgaps [6].

1.3 Properties and applications

Due to the huge variety of air-holes arrangements, PCFs offer a wide possibility to control the refractive index contrast between the core and the photonic crystal cladding and, as a consequence, novel and unique optical properties.

Since PCFs provide new or improved features, beyond what conventional optical fibers offer, they are finding an increasing number of applications in ever-widening areas of science and technology.

1.3.1 Solid-core fibers

Index-guiding PCFs, with a solid glass region within a lattice of air-holes, offer a lot of new opportunities, not only for applications related to fundamental fiber optics. In fact, it is possible to exploit some special properties of the photonic crystal cladding, which are due to the large refractive index contrast and the two-dimensional nature of the microstructure, thus affecting the dispersion, the smallest attainable core size, the number of guided modes, the numerical aperture and the birefringence.

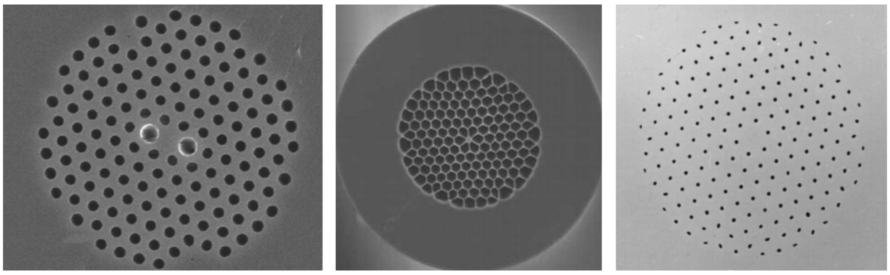

(a) (b) (c)

Figure **1.7**: (a) Example of a highly birefringent PCF presented in [2]. (b) Highly nonlinear PCF with small-silica core and large air-holes [10]. (c) Dispersion-flattened triangular PCF presented in [11].

Highly birefringent fibers

Birefringent fibers, where the two orthogonally polarized modes carried in a single-mode fiber propagate at different rates, are used to maintain polarization states in optical devices and sub-systems. The guided modes become birefringent if the core microstructure is deliberately made two-fold symmetric, for example by introducing capillaries with different wall thicknesses above and below the core. By slightly changing the air-hole geometry, it is possible to produce levels of birefringence that exceed the performance of conventional birefringent fiber by an order of magnitude. It is important to underline that, unlike traditional polarization maintaining fibers, such as bow-tie, elliptical-core or Panda, which contain at least two different glasses each with a different thermal expansion coefficient, the birefringence obtainable with PCFs is highly insensitive to temperature, which is an important feature in many applications. An example of a highly birefringent PCF is reported in Fig. 1.7a.

Fibers with unusual dispersion properties

The tendency for different light wavelengths to travel at different speeds is a crucial factor in the telecommunication system design. A sequence of short light pulses carries the digitized information. Each of these is formed from a spread of wavelengths and, as a result of chromatic dispersion, it broadens as it travels, thus obscuring the signal. The magnitude of the dispersion changes with the wavelength, passing through zero at 1.3 μm in conventional optical fibers.

In PCFs the dispersion can be controlled and tailored with unprecedented freedom. In fact, due to the high refractive index difference between silica and air, and to the flexibility of changing air-hole sizes and patterns, a much broader range of dispersion behaviours can be obtained with PCFs rather than with standard fibers.

For example, as the air-holes get larger, the PCF core becomes more and more isolated, until it resembles a strand of silica glass suspended by six thin webs of glass, as it is shown in Fig. 1.7b. If the whole structure is made very small, the zero-dispersion wavelength can be shifted to the visible, since the group velocity dispersion is radically affected by pure waveguide dispersion.

On the contrary, very flat dispersion curves can be obtained in certain wavelength ranges in PCFs with small air-holes, that is with low air-filling fraction. As an example, Fig. 1.7c reports the dispersion-flattened triangular PCF presented in [11], with seven air-hole rings, characterized by $\Lambda \simeq 2.5$ μm and $d \simeq 0.5$ μm.

Highly nonlinear fibers

An attractive property of solid-core PCFs is that effective index contrasts much higher with respect to conventional optical fibers can be obtained by making large air-holes, and/or by reducing the core dimension, so that the light is forced into the air-holes. In this way a strong confinement of the guided-mode can be reached, thus leading to enhanced nonlinear effects, due to the high field intensity in the core. Moreover, a lot of nonlinear experiments require specific dispersion properties of the fibers. As a consequence, PCFs can be successfully exploited to realize nonlinear fiber devices, and this is presently one of their most important applications.

An important example is the supercontinuum generation, that is the formation of broad continuous spectra by the propagation of high power pulses through nonlinear media. The term supercontinuum does not indicate a specific phenomenon, but rather a plethora of nonlinear effects, which, in combination, lead to extreme pulse broadening. The determining factors for supercontinuum generation are the dispersion properties of the nonlinear medium relative to the pumping wavelength, the pulse length and the peak power. Since the nonlinear effects involved in the spectral broadening are highly dependent on the medium dispersion, a proper design of the dispersion properties can significantly reduce the power requirements. The widest spectra can be obtained when the pump pulses are launched close to the zero-dispersion wavelength of the nonlinear media. An increased interest in the supercontinuum experiments has been caused by the introduction of the nonlinear PCFs with zero-dispersion wavelengths in the range of the Ti:Sapphire femtosecond laser systems, that is around 800 nm [4].

For example, it has been demonstrated that a highly nonlinear PCF, designed with the zero chromatic dispersion close to 800 nm, displays giant spectral broadening when a 100 MHz pulse train is launched into just a few cm of fiber. The pulses have the bandwidth of sunlight but are 104 times brighter.

The supercontinuum turns out to consist of millions of individual frequencies, precisely separated by the repetition rate of the pump laser. This "frequency comb" can be used to measure optical frequency with a very high accuracy. The huge bandwidth and high spectral brightness of the supercontinuum source make it ideal for all sorts of spectroscopy. In particular, measurements which usually took hours and involved counting individual photons can now be made in a fraction of a second. Moreover, since the light emerges from a microscopic aperture, it is particularly easy to perform spectroscopy with very high spatial resolution [6]. Finally, the typical output spectrum is smooth and stable, and so well suited for pulse compression or optical coherence tomography.

Large mode area fibers for high power applications

By changing the geometric characteristics of the fiber cross-section, it is possible to design PCFs with completely different properties, that is with large effective area. The typical cross-section of this kind of fibers, called Large Mode Area (LMA) PCFs, consists of a triangular lattice of air-holes where the core is defined by a missing air-hole. An example of a triangular PCF is reported in Fig. 1.8a. The PCF core diameter can be defined as $d_{core} = 2\Lambda - d$, which corresponds to the distance between opposite air-hole edges in the core region. When $d/\Lambda < 0.4$, the triangular PCF is endlessly single-mode, that is single-mode at any wavelength [7, 8]. In this condition it is the core size, or the pitch, that determines the zero-dispersion wavelength λ_0, the Mode Field Diameter (MFD) and the Numerical Aperture (NA) of the fiber. By exploiting the particular PCF properties, a very large core single-mode light guiding can be obtained. LMA PCFs are usually exploited for high-power applica-

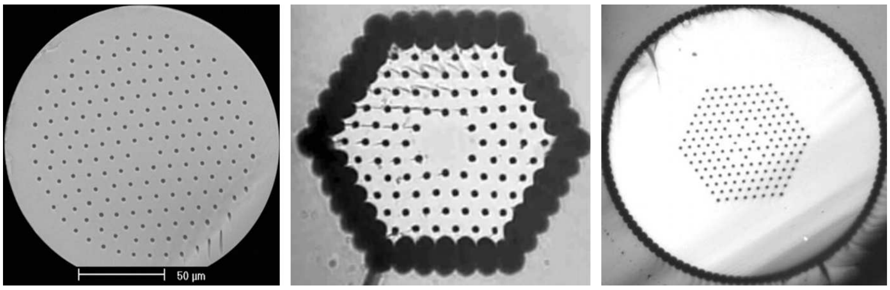

(a) (b) (c)

Figure **1.8**: (a) Microstructured LMA fiber for high-power delivery applications. (b) Microscope image of one of the Yb^{3+}-doped air-clad PCF produced by Crystal Fibre A/S [12]. (c) Cross-section picture of a 7 core Yb^{3+}-doped air-clad fiber [12].

tions, since fiber damage and nonlinear limitations are drastically reduced. Another important application is single-mode transmission at several different wavelengths, for example for RGB or broadband interferometry. Finally, more complicated designs, such as multicore fibers, are used in applications like parallel data transmission [12].

Conventional active fibers are basically standard transmission fibers whose core region has been doped with rare-earth elements. These fibers, also known as "core-pumped", are usually pumped with single-mode pump lasers. Due to its power limitations, this kind of fiber is unsuitable for high power applications, on the order of 1 W and upwards. High power fibers are usually designed with a double-cladding structure, where a second low-index region acts as a cladding for a large pump core. In the center of the pump core is located a much smaller doped signal core. With respect to the more traditional core-pumped design, double-cladding fibers present a large pump area and a high numerical aperture, thus enabling pumping with relatively low-cost multi-mode diodes and diode bars/stacks. However, it is important to underline that, when considering high powers, it is necessary to optimize fiber characteristics, such as NA, core dimension and length, in order to obtain efficient coupling of the pump light, reduction of nonlinear effects, high conversion of pump light and good thermal properties [12].

Since PCF structures can provide single-mode waveguides with MFD values above 40 μm, LMA PCFs can be successfully used as active fibers for high power applications. Double-cladding PCFs consist of a LMA structure with a doped-core inside an air-clad pump guide. Very high NA values, determined by the silica bridge width, are provided by the air-clad, since the refractive index contrast is greatly enhanced. As a consequence, the NA is only limited by the practical handling of the fibers, being the cleaving increasingly challenging at NA values above 0.6. Moreover, the thermal conductivity is greatly improved compared to conventional polymer-clad fibers, because the PCF is made only of glass and air, and there is no material degradation. The power density limit is set only by the silica damage threshold. Finally, the combination of very large MFD and high NA offered by PCFs makes it possible to fabricate lasers and amplifiers with very short fiber lengths, drastically reducing the nonlinear effects [12].

As an example, an air-clad Yb^{3+}-doped fiber characterized by a hexagonal inner cladding with a diameter of 117 μm and a NA of about 0.6 has been fabricated by Crystal Fibre A/S [12]. The microscope picture of the fiber cross-section is reported in Fig. 1.8b. Only 48 cm of this fiber, pumped from one end, has been used by University of Bordeaux and University of Jena to realize a high power laser [13].

For industrial material processing applications kW average power levels are desirable. These power levels can be now obtained with fiber lasers. By exploiting the advantages offered by air-clad active PCFs, that is large Yb^{3+}-doped core mode-field areas and high NA all-silica pump core, reliable kW lasers can be realized with short fiber lengths [12].

Once reached the power limit of the fibers previously described, multicore PCF designs will be exploited in order to obtain a further scaling of the power level. For example, a 7 core air-clad Yb-doped fiber was fabricated by Crystal Fibre A/S for QinetiQ (UK) [12]. As reported in Fig. 1.8c, each LMA-type core has a mode-field diameter of 15 μm. QinetiQ applied this fiber in a laser configuration and obtained lasing in a supermode with high beam quality. The next planned generation of multicore fibers will have 18 cores [12].

1.3.2 Hollow-core fibers

Hollow-core PCFs have great potential, since they exhibit low nonlinearity [14] and high damage threshold [15–17], thanks to the air-guiding in the hollow-core and the resulting small overlap between silica and the propagating mode. As a consequence, they are good candidates for future telecommunication transmission systems, as well as for the delivery of high-power beams for laser machining and welding.

Moreover, they are suitable for nonlinear optical processes in gases, which require high intensities at low power, long interaction lengths and good-quality transverse beam profiles. For example, it has been demonstrated that the threshold for stimulated Raman scattering in hollow-core fibers filled with hydrogen is orders of magnitude below that obtained in previous experiments [18]. In a similar way, PCFs with a hollow core can be used for trace gas detection or monitoring, or as gain cells for gas lasers. Finally, the delivery of solid particles down a fiber by using optical radiation pressure has been demonstrated [6]. In particular, only 80 mW of a 514 nm argon laser light was enough to levitate and guide 5 μm polystyrene spheres along a 15 cm length of PCF with a hollow-core diameter of 20 μm [19].

1.4 Loss mechanisms

The most important factor for any optical fiber technology is loss. Losses in conventional optical fibers have been reduced over the past 30 years, and a further improvement is unlikely to be reached. The minimum loss in fused silica, which is around 1550 nm, is slightly less than 0.2 dB/km. This limit is important, since it sets the amplifier spacing in long-haul communications systems, and thus is a major cost of a long-haul transmission system [1].

The optical loss α_{dB}, measured in dB/km, of PCFs with a sufficiently reduced confinement loss can be expressed as

$$\alpha_{dB} = A/\lambda^4 + B + \alpha_{OH} + \alpha_{IR} \ , \tag{1.1}$$

being A, B, α_{OH} and α_{IR} the Rayleigh scattering coefficient, the imperfection loss, and OH and infrared absorption losses, respectively. At the present time these loss components in PCFs are dominated by OH-absorption loss and imperfection loss [20].

In a typical solid-core PCF the OH-absorption loss is more than 10 dB/km at 1380 nm and this causes an additional optical loss of 0.1 dB/km in the wavelength range around 1550 nm. Since this contribution is very similar to the intrinsic optical loss of 0.14 dB/km for pure silica glass at this wavelength, the OH-absorption loss reduction becomes an important and challenging problem. Most of the OH impurities seem to penetrate the PCF core region during the fabrication process. As a consequence, a dehydration process is useful in

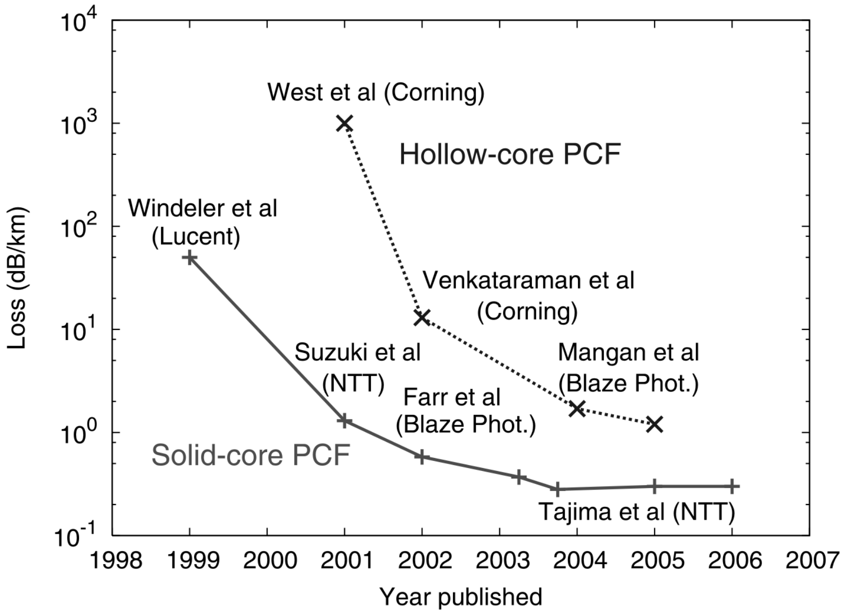

Figure **1.9**: Optical loss behaviour during the past years, until 2006, for index- and air-guiding PCFs [5].

reducing the OH-absorption loss [20]. Imperfection loss, caused mainly by air-hole surface roughness, is another serious problem. In fact, during the fabrication process, the air-hole surfaces can be affected by small scratches and contamination. If this surface roughness is comparable with the considered wavelength, it can significantly increase the scattering loss. Thus, it is necessary to improve the polishing and etching process, in order to reduce the optical loss caused by this roughness. Moreover, fluctuation in the fiber diameter during the fiber drawing process can cause an additional imperfection loss, if the air-hole size and pitch change along the fiber [20].

It is important to underline that the Rayleigh scattering coefficient of solid-core PCFs is the same as that of a conventional SMF. However, this is higher than that of a pure silica-core fiber, although the PCF is made of pure silica glass. It is necessary to reduce the roughness further, in order to obtain a lower imperfection loss and a lower Rayleigh scattering coefficient [20].

Losses in hollow-core fibers are limited by the same mechanisms as in

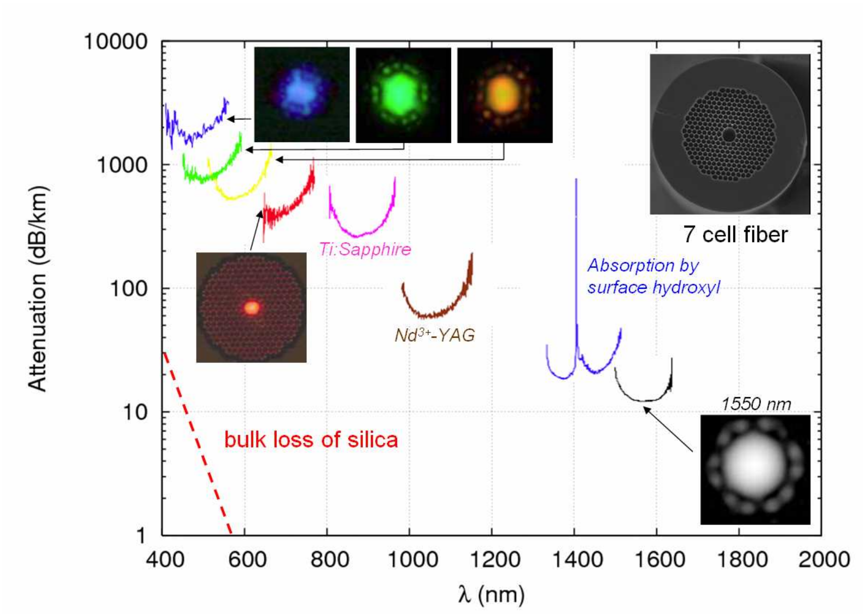

Figure **1.10**: Spectral guiding profiles for a range of 7-cell hollow-core PCFs fabricated by Crystal Fibre A/S [12]

conventional fibers and in index-guiding PCFs, that is absorption, Rayleigh scattering, confinement loss, bend loss and variations in the fiber structure along the length. However, there is the possibility to reduce them below the levels found in conventional optical fibers, since the majority of the light travels in the hollow core, in which scattering and absorption could be very low.

In Fig. 1.9 the decrease of the loss for fabricated index-guiding PCFs as well as air-guiding PBG is shown until 2006. Early in their development solid-core PCFs had optical losses of the order of 0.24 dB/m [22] and the available length was limited to several meters. The optical losses of PCFs were rapidly reduced to 1 dB/km by improving the fabrication process [23–25]. The lowest loss yet achieved is 0.28 dB/km [26]. Recently, a low loss, that is 0.3 dB/km, and long length, that is 100 km, PCF was reported [27]. The optical losses of these kind of PCFs are still high compared with those of a conventional SMF. However, a solid-core PCF is not expected to have

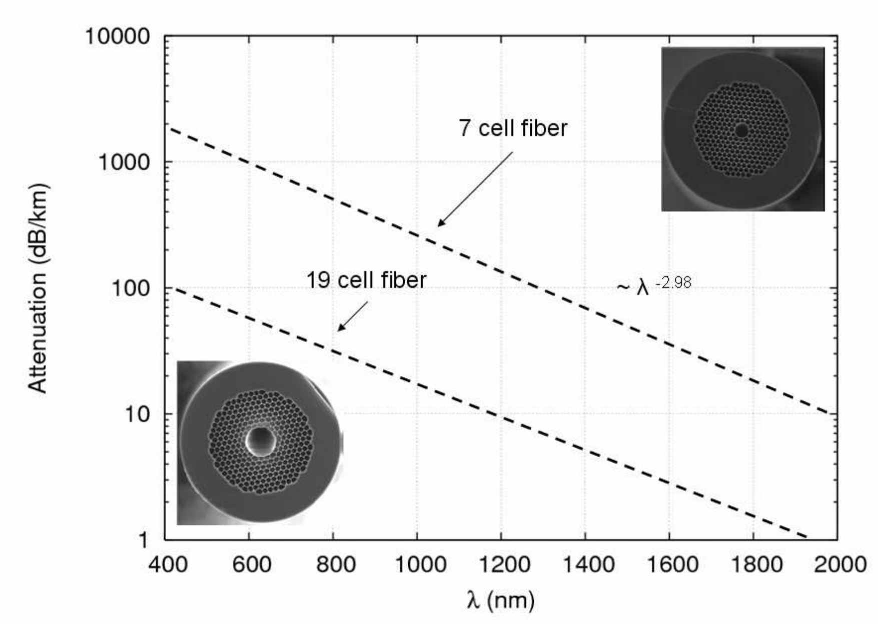

Figure **1.11**: Attenuation scaling with wavelength for 7 and 19-cell hollow-core PCFs [21].

significantly lower losses than standard fibers. By considering hollow-core PCFs, the attenuation values reported in literature are higher than those for both solid-core PCFs and standard fibers. In fact, looking at the attenuation profiles for a range of hollow-core fibers made by Crystal Fibre A/S, reported in Fig. 1.10, it is possible to notice two important facts [12]. The guiding bandwidth is usually around 15% of the central wavelength and the loss scales inversely with the wavelength. As indicated by theoretical considerations, the attenuation related to mode coupling and scattering at the internal air-silica interfaces should scale with the wavelength λ as λ^{-3}. This consideration has been confirmed by experimental observations [21]. All the fibers considered in Fig. 1.10 are based on a 7-cell design, that is the hollow core has been obtained by removing 7 capillaries in the fiber cross-section center. It is important to underline that, in order to reach lower losses, 19-cell designs can be used, as it is demonstrated by the loss values reported in Fig. 1.11 [21]. The minimum-

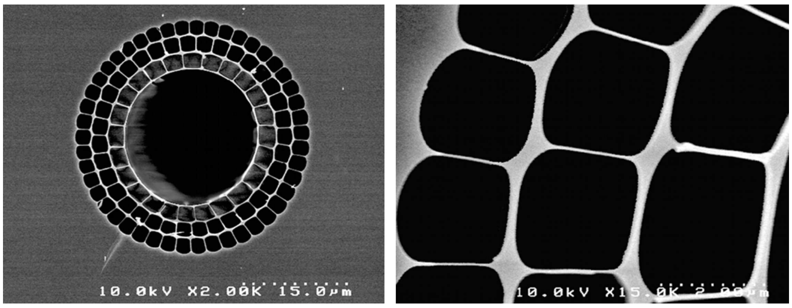

(a) (b)

Figure **1.12**: Scanning Electron Microscope pictures of a hollow-core Bragg fiber (a) overall cross-section and (b) cladding region. [28, 29]

loss record of 1.7 dB/km has been obtained [21]. In fact, a larger core reduces the overlap of the guided modes with silica.

Reducing the hollow-core PCF loss to levels below those of conventional silica fibers remains a challenge. Confinement losses can be eliminated by forming a photonic crystal cladding with a sufficient number of air-hole rings, while bending losses, which are determined by the fiber design, can be reduced to a low level in at least some structures. For what concerns Rayleigh scattering, as well as absorption, they should be reduced to below the level in bulk fibers, even if the increased scattering at the many surfaces represents potentially a problem. However, the biggest unknown is the level of variation in the fiber structure along the length. In fact, the bandgap presents a high sensitivity to structural fluctuations that occur over long fiber lengths, that is wavelengths that are guided in one section may leak away in another.

Finally, there is an excess loss in hollow-core PCFs which occurs at wavelengths where there is coupling from the air-guided fundamental mode to the confined surface modes, which have much greater overlap with the glass and, as a consequence, experience far higher loss. Notice that a larger hollow core gives increased perimeters, leading to a greater density of surface modes, which lead to decreased bandwidth and also to increased higher-order dispersion [30]. A new class of hollow-core fibers affected by surface modes, are the so called Bragg fibers. They were proposed in late seventies and confine light by Bragg reflection from concentric rings of dielectric layers with different refractive index [31]. In recent years, the advent of photonic crystal fibers has provided a new way to achieve air guiding and to design Bragg fibers. In particular, air-silica Bragg fibers have been fabricated with a cladding characterized by thin silica rings, surrounded by air and connected by nanoscale silica bridges [28,29]. An example is reported in Fig. 1.12a. As better discussed in Chapter 2, numerous surface modes arise in the cladding and are mainly localized in the thin silica regions or in correspondence of the junctions between the bridges and the rings which define the air-holes in the cladding, clearly shown in Fig. 1.12b. These modes couple with the fundamental one [32] and cause significant losses in the fiber.

In conclusion, the significant reduction over the past few years suggests that loss will be reduced still further in hollow-core fibers.

1.5 Fabrication process

One of the most important aspect in designing and developing new fibers is their fabrication process. Producing conventional single-mode optical fibers requires core and cladding materials with similar refractive index values, which typically differ by around a percent. On the contrary, designing PCFs requires a far higher refractive index contrast, differing by perhaps $50 \div 100\%$. The small index differences in conventional fibers are usually obtained by vapour deposition techniques, but the larger ones needed for PCFs have been most widely achieved by developing the stack-and-draw technique, investigated in the 1970s by Bell Laboratories and others, or by directly forming the glass by using, for example, extrusion through a die [1].

In a lot of papers presented in literature so far, PCFs have been realized by "introducing" air-holes in a solid glass material. This has several advantages, since air is mechanically and thermally compatible with most materials, it is transparent over a broad spectral range, and it has a very low refractive index at optical frequencies.

Fibers fabricated using silica and air have been accurately analyzed, partly because most conventional optical fibers are produced from fused silica. This is also an excellent material to work with, because viscosity does not change much with temperature and it is relatively cheap. Moreover, filling the holes of a silica-air structure opens up a wide range of interesting possibilities, such as the bandgap guidance in a low-index core made of silica when the holes are filled with a high-index liquid.

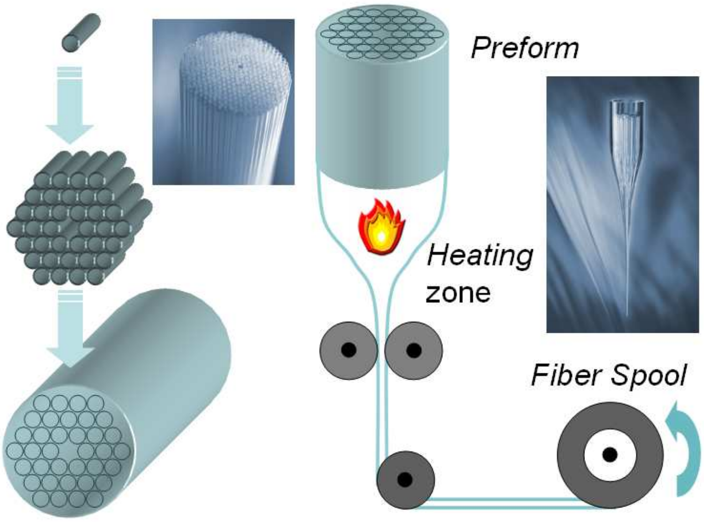

Figure **1.13**: Scheme of the PCF fabrication process [33].

1.5.1 Stack-and-draw technique

In order to fabricate a PCF, it is necessary, first, to create a preform, which contains the structure of interest, but on a macroscopic scale. The PCF preform is realized by stacking by hand a number of capillary silica tubes and rods to form the desired air-silica structure, as reported in Fig. 1.13. This way of realizing the preform allows a high level of design flexibility, since both the core size and shape, as well as the index profile throughout the cladding region can be controlled. Then the preform is drawn down on a conventional high-temperature fiber-drawing tower, greatly extending its length, while reducing its cross-section, as shown in Fig. 1.13. Through a careful process control, the air-holes retain their arrangement all through the drawing process.

A typical preform is a meter long and 20 mm in diameter, and it contains several hundreds of capillaries. By jacketing this stack, and perhaps using pressure to maintain the air-hole size in the fiber, a wide range of different structures have been made, each with different optical properties. Finally, the PCFs are coated to provide a protective standard jacket, which allows the robust handling of the fibers. The final PCFs are comparable to standard

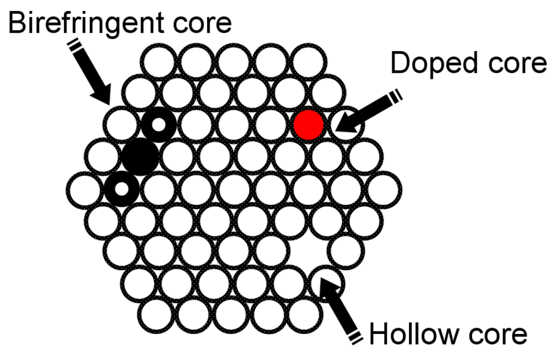

Figure **1.14**: Example of a PCF cross-section, showing the flexibility offered by the stack-and-draw fabrication process [34].

fibers in both robustness and physical dimensions, and can be both stripped and cleaved using standard tools.

It is important to underline that the stack-and-draw procedure, represented in Fig. 1.13, proved highly versatile, allowing complex lattices to be assembled from individual stackable units of the correct size and shape. Solid, empty or doped glass regions can be easily incorporated, as reported in Fig. 1.14. Notice that the fabrication technique success is largely due to the mechanical stability of the structure. In fact, the surface tension forces tend to balance out, allowing the formation of highly regular lattices of air-holes during the drawing process. Overall collapse ratios as large as about 50000 times have been realized, and continuous holes as small as 25 nm in diameter have been demonstrated, earning an entry in the Guinness Book of Records in 1999 for the World's Longest Holes [6].

Chapter 2

PCF guiding properties

This Chapter summarizes the results obtained by studying the PCF properties both numerically, through a full vector modal solver based on the Finite Element Method (FEM) and experimentally with different kinds of fiber samples.

The PCF guiding properties have been evaluated starting from a parameter which characterizes the PCF modes, that is the value of the complex propagation constant $\gamma = \alpha + jk_0 n_{eff}$, being α the attenuation constant, n_{eff} the effective index and k_0 the wave number in the vacuum, as reported in Appendix A.

First of all, results regarding a new kind of PCFs, with a square lattice of air-holes in a silica matrix [35], are reported. The modal cut-off of square-lattice PCFs has been evaluated by taking into account the leakage losses, that is the attenuation constant α of the second-order mode [36, 37]. This analysis, already presented in literature for triangular PCFs, has been done for the first time for PCFs with a square lattice of air-holes.

The same method used for the square-lattice PCFs has been applied to study the cut-off properties of a new kind of LMA triangular PCFs, called 7-rod, which have a large silica core obtained by removing the central air-hole and the ones belonging to the first ring [38, 39]. In fact, it is important to investigate the trade-off between the effective area and the single-mode operation regime of 7-rod triangular PCFs, in order to successfully exploit them in practical applications.

Moreover, the guiding properties of realistic all-silica hollow-core Bragg fibers, reported in Fig 1.12, have been investigated by calculating the dispersion curve, the confinement loss spectrum and the field distribution of the guided modes. In particular, the silica bridge influence on the fundamental mode has been analyzed, by comparing the properties of an ideal structure, without the silica nano-supports, and of two realistic fibers, with squared off and rounded air-holes. Simulation results have demonstrated the presence of anti-crossing points in the dispersion curve, associated to the transition of the fundamental mode into a surface one. It has been shown that surface modes are responsible of the sharp loss peaks, also experimentally measured, which pollute the loss spectrum of the fundamental mode and of the higher-order ones. Then, the influence on the guiding properties of each geometric characteristic in the hollow-core Bragg fiber cross-section has been deeply investigated, thus showing which parameter it is better to change in order to properly modify the loss values or its spectral behaviour. Moreover, in order to improve the loss properties of hollow-core Bragg fibers, the number of silica and air layers in the fiber cladding has been increased, and the layer thickness has been modified. Results have shown that the first change is more effective for the loss reduction, while the second is useful for a spectral shift. Among the different possible applications, the feasibility of a DNA bio-sensor based on a hollow-core Bragg fiber has been demonstrated.

As regards the experimental measurements, a Scanning Near-Field Optical Microscope (SNOM) has been used to measure the guided.mode field distribution on the PCF cross-section, and to evaluate the effective area. Through the

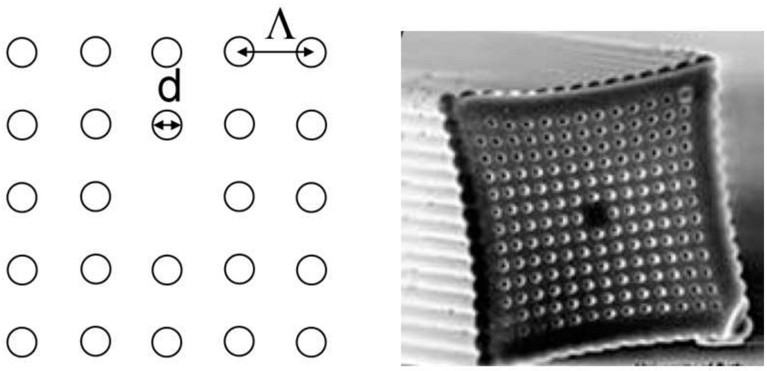

(a) (b)

Figure **2.1**: (a) Detail of the square-lattice PCF cross-section. (b) Scanning electron micrograph of a square-lattice PCF intermediate preform.

comparison with the experimental values, the accuracy of the effective area calculation performed with the FEM solver has been demonstrated.

In addition, the spectral broadening of a 50 fs Ti:Sapphire laser pulse with average power of 150 mW, coupled into a 39 cm-long nonlinear highly birefringent microstructure fiber fabricated from silicate glass, has been experimentally observed. The modal polarization and dispersive properties of the fiber have been also analyzed using the full vector FEM solver. Particularly, the calculations have revealed the guidance of two orthogonally polarized eigenmodes with different effective index values.

2.1 Cut-off properties of square-lattice PCFs

It has been already underlined in Chapter 1 that PCFs have particular properties, strictly related to the geometric characteristics of the air-holes in their cross-section. As a consequence, it is interesting to analyze how a regular air-hole disposition different from the triangular one, usually studied so far, can affect the characteristics of the guided mode. Moreover, it is important to understand in which terms all the results previously obtained for the triangular PCFs can be applied to fibers with different lattice geometries.

To this aim, a PCF with a square lattice has been considered. In this

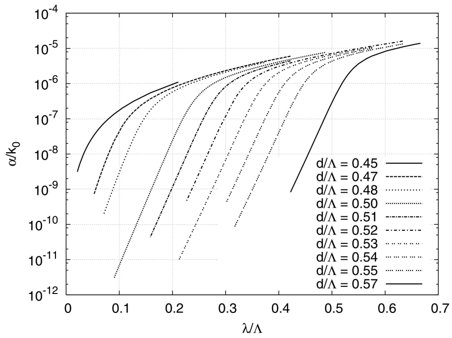

(a)

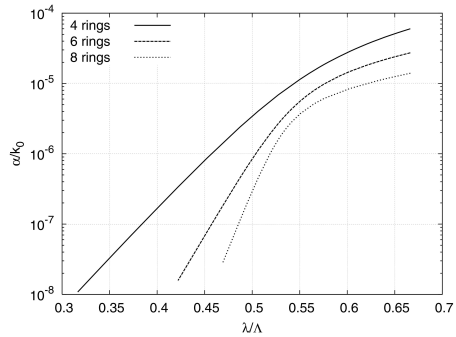

(b)

Figure **2.2**: Second-order mode α/k_0 versus the normalized wavelength λ/Λ (a) for 8 ring square-lattice PCFs with d/Λ in the range $0.45 \div 0.574$ and (b) as a function of the air-hole ring number, that is 4, 6 or 8, for a square-lattice PCF with $d/\Lambda = 0.57$.

fiber the air-holes are organized in a square lattice, characterized by the same geometric parameters as the triangular one, that is Λ and d/Λ, as reported in Fig. 2.1a. It has been already demonstrated the technological feasibility of square-lattice PCFs, which can be drawn from intermediate preforms, as shown in Fig. 2.1b, realized with the standard stack-and-draw fabrication process [40]. Recently, square-lattice fibers have been fabricated and characterized in order to analyze their polarization properties, and a great potential for high birefringence has been shown [41, 42].

As it has been previously demonstrated [35], square-lattice PCFs present a wider effective area than triangular ones for fixed d/Λ and Λ values, so they can be of practical interest as LMA fibers for high-power delivery. In order to successfully use square-lattice PCFs for this kind of applications, it is necessary to define their single-mode operation regime. For the first time, the modal cut-off of square-lattice PCFs with a finite number of air-hole rings has been accurately investigated, in order to find the boundary between the single-mode and the multi-mode operation regimes.

It has been already demonstrated that PCFs with a silica core, which guide light by modified total internal reflection, can be designed to be endlessly single-mode, that is only the fundamental mode can propagate in the fiber core for all the wavelengths, unlike conventional fibers which exhibit a cut-off

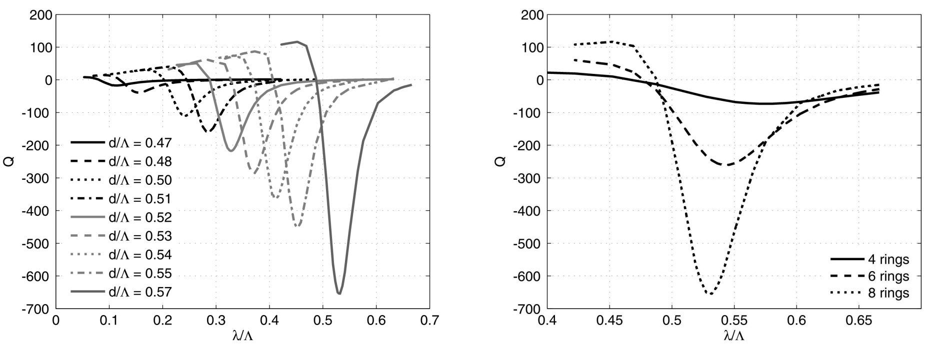

(a) (b)

Figure **2.3**: Q parameter values versus the normalized wavelength λ/Λ (a) for 8 ring square-lattice PCFs with d/Λ in the range $0.45 \div 0.57$ and (b) as a function of the air-hole ring number, that is 4, 6 or 8, for a square-lattice PCF with $d/\Lambda = 0.57$.

wavelength below which higher-order modes are supported [43, 44]. A cut-off analysis for PCFs is not trivial as for conventional optical fibers because all the modes propagating in PCFs with a finite air-hole ring number are leaky [45–47]. The single-mode regime has been already successfully investigated for triangular PCFs [7, 8, 44, 48]. In particular, it has been evaluated that triangular PCFs are endlessly single-mode for $d/\Lambda < d^*/\Lambda$ and recently the value $d^*/\Lambda \simeq 0.406$ has been proposed [7, 8].

Different approaches have been used in previous works to study the single-mode regime of triangular PCFs, that is the wavelength range where only the first-order mode is guided, while the higher order ones are unbound. In particular, it is necessary to decide clearly at which wavelength λ^* the second-order mode is no more guided, that is it becomes a delocalized cladding mode. In order to find this transition, it is possible to take into account the divergence at long wavelengths of its effective area [49], or its leakage losses, which are related to the attenuation constant α, the real part of the complex propagation constant in Eq. (A.2) [45, 47]. In particular, the normalized cut-off wavelength λ^*/Λ can be evaluated by observing the transition shown by the behaviour of α/k_0, k_0 being the wave number, versus λ/Λ [48]. This can be made evident by calculating the Q parameter

$$Q = \frac{d^2 \log[\alpha/k_0]}{d^2 \log(\Lambda)} , \tag{2.1}$$

because it exhibits a sharp negative minimum at λ^*/Λ [48]. In the present analysis the phase diagram with single-mode and multi-mode operation for square-lattice PCFs has been obtained by calculating the Q parameter for different normalized wavelength λ/Λ and by evaluating its negative minimum for PCFs with d/Λ in the range $0.45 \div 0.57$. The analysis has been developed by fixing the guided-mode wavelength at 633 nm. The hole-to-hole distance Λ has been properly selected to obtain the desired normalized wavelength value. Due to the strong influence of the air-hole ring number on the leakage losses of PCFs with a finite cross-section [45, 46], fibers with 4, 6 and 8 rings have been considered for the modal cut-off analysis. In fact, it has been already demonstrated that the transition of the Q parameter becomes more acute and the method more reliable as the ring number increases [48]. Finally, it is important to point out the numerical methods used in this analysis. The complex propagation constants of the fundamental and the second-order mode, as well as the field distributions, have been calculated by means of the FEM full-vector modal solver with anisotropic PML [45, 47], as described in Appendix A. The multipole method [50, 51] has been also used to confirm the simulation results, obtaining a good agreement.

In order to calculate the Q parameter according to Eq. (2.1), the behaviour of α/k_0 versus the normalized wavelength λ/Λ for the second-order mode has to be evaluated. As shown in Fig. 2.2a for 8 ring PCFs with different d/Λ values, α/k_0 increases with λ/Λ, that is the confinement of the second-order mode is lower for smaller pitch Λ. For all the considered d/Λ ratios the curves show a transition, that is a change in the slope which becomes sharper as the air-hole diameter increases with respect to the pitch. Moreover, by varying d/Λ from 0.45 to 0.57 the transition region moves toward the higher λ/Λ values, as it has been already demonstrated for triangular PCFs [48]. In addition, notice that, when $d/\Lambda = 0.45$, it is difficult to identify the transition, which, on the contrary, is very sharp when $d/\Lambda = 0.57$. The same behaviour of α/k_0 has been obtained for square-lattice PCFs with a lower air-hole ring number, that is 4 and 6. However, it must be observed that, in these cases, as shown in Fig. 2.2b, the transition is not so sharp even for a high d/Λ value.

From the previous results, the Q parameter has been calculated through a finite difference formula and the values obtained for the 8 ring square-lattice

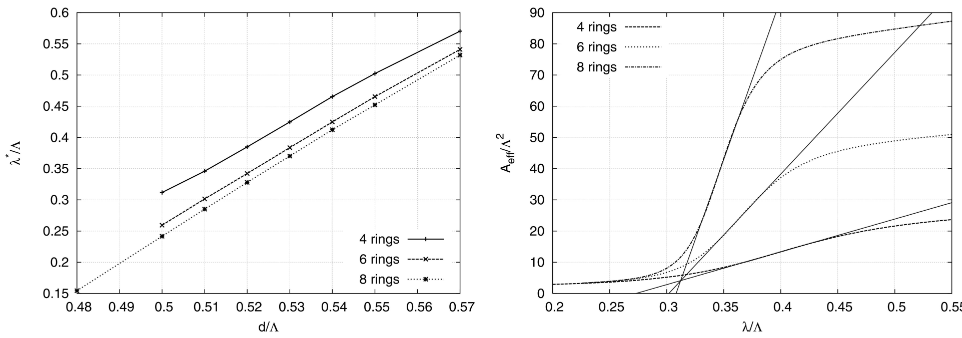

(a) (b)

Figure **2.4**: (a) Normalized cut-off wavelength λ^*/Λ as a function of the d/Λ ratio for square-lattice PCFs with 4, 6 and 8 air-hole rings. (b) Second-order mode normalized effective area A_{eff}/Λ^2 versus λ/Λ for square-lattice PCFs with $d/\Lambda = 0.52$ and with 4, 6 and 8 air-hole rings.

PCFs are reported in Fig. 2.3a. The negative value of the curve minimum becomes higher as d/Λ increases, reaching -654 at $\lambda/\Lambda \simeq 0.532$ for $d/\Lambda = 0.57$. As the square-lattice PCF air-filling fraction decreases, the Q minimum moves toward the lower λ/Λ values and becomes wide and difficult to identify with high precision. For example, the negative minimum almost disappears for the PCFs with $d/\Lambda = 0.45$ and its curve has not even been drawn in the figure. A similar behaviour has also been obtained for PCFs with less air-hole rings. Fig. 2.3b, for example, reports data for PCFs with $d/\Lambda = 0.57$, showing that the Q minimum becomes less negative and moves toward higher λ/Λ values when the ring number decreases. In particular, for 4 ring fibers the dip is very wide and the most negative value is only -73 at $\lambda/\Lambda \simeq 0.571$, while it is -260 at $\lambda/\Lambda \simeq 0.541$ when the square-lattice PCFs have 6 air-hole rings.

In summary, Fig. 2.2 and 2.3 clearly show that, when the leakage behaviour is strong, whatever the reason, for example low d/Λ or few air-hole rings, it is difficult to define the transition region and the related cut-off wavelength. On the contrary, by considering a high number of air-hole rings the slope change in α/k_0 is more evident, the Q curve presents a sharp dip and it is possible to find reliable values of the normalized cut-off wavelength λ^*/Λ. These values for the square-lattice PCFs with 8 air-hole rings are reported in Fig. 2.4a, which also shows data for 4 and 6 ring PCFs. Notice that the λ^*/Λ values

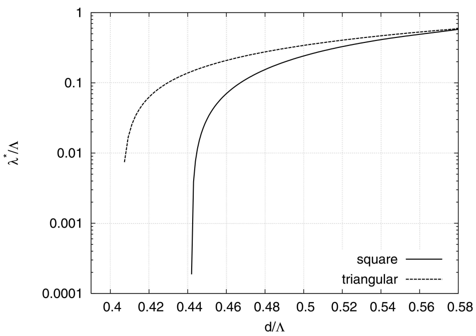

(a)

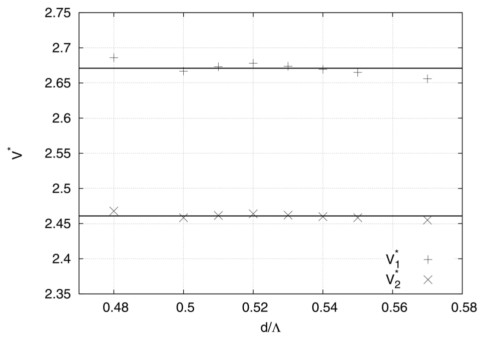

(b)

Figure **2.5**: (a) Phase diagram for 8 air-hole ring PCFs characterized by the square and the triangular lattice. (b) Cut-off value V^* of the normalized frequency according to the two definition for square-lattice PCFs with 8 rings. Solid lines represent the mean value of V_1^* and V_2^*.

have been reported only for the well-defined and sharp minima, that is for $d/\Lambda \geq 0.48$ for 8 ring PCFs and for $d/\Lambda \geq 0.50$ for 4 and 6 ring PCFs. As expected, results change by increasing the air-hole rings, tending to the values of a PCF with an ideal infinite cladding. This suggests again that the Q parameter method must be applied assuming a high ring number.

This conclusion is confirmed also by further comments on results reported in Fig. 2.4a. In fact, it seems that PCFs with 4 air-hole rings have a smaller single-mode region, defined by $\lambda/\Lambda > \lambda^*/\Lambda$, their cut-off values being the highest ones. However, this result is in contradiction with the α/k_0 values reported in Fig. 2.2b, which are also the highest for all the considered λ/Λ. Fig. 2.2b, in fact, indicates that the second-order mode suffers from high leakage losses and consequently only the fundamental mode can actually propagate in a wider single-mode spectral range. In other words, the Q parameter approach fails when a sharp minimum does not occur, as shown in Fig. 2.3b for the case of 4 air-hole rings. On the contrary, by considering 8 air-hole rings, results are clearly readable and reliable. It is important to highlight that the λ^*/Λ evaluated for PCFs with many rings of air-holes also apply to fibers with few rings, being λ^*/Λ, in any case, an upper limit of the cut-off wavelength. This means that fibers with a reduced number of rings present an even larger single-mode region.

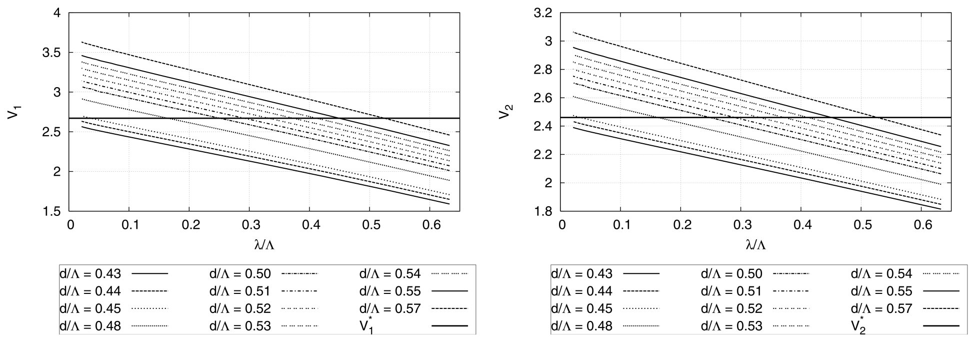

(a) (b)

Figure **2.6**: (a) V_1 and (b) V_2 behaviour versus the normalized wavelength λ/Λ for square-lattice PCFs with d/Λ between 0.43 and 0.57. A solid horizontal line is drawn at the fixed value V_1^* and V_2^*, respectively.

In order to give a further confirmation of what stated, the normalized cut-off wavelength has been evaluated also according to another approach, the method based on the second-order mode effective area, proposed by Mortensen et al. [49]. Simulation results for the PCFs with $d/\Lambda = 0.52$ are shown in Fig. 2.4b. Notice that the λ^*/Λ values, indicated by the crossing of the solid lines with the horizontal axis, are, respectively, 0.273, 0.302 and 0.308 for the PCFs with 4, 6 and 8 air-hole rings. This means that λ^*/Λ increases with the air-hole ring number, that is the PCFs which provide the better field confinement have the smallest single-mode operation region and not the other way round, as could be suggested by Fig. 2.4a. Moreover, the difference between the normalized cut-off wavelength values almost vanishes if PCFs with 6 and 8 rings are considered. Thus 8 ring square-lattice PCFs offer the most reliable results and, in the following, will also be used to compare square and triangular lattice PCF characteristics.

A first interesting comparison can be made on the endlessly single-mode region. For fibers with a triangular lattice of air-holes, a fitting of the cut-off curve has been evaluated according to the expression [48]

$$\lambda^*/\Lambda \simeq \alpha \cdot (d/\Lambda - d^*/\Lambda)^{\gamma} \ , \tag{2.2}$$

where d^*/Λ is the boundary of the endlessly single-mode region, resulting in $d^*/\Lambda = 0.406$, $\alpha = 2.80 \pm 0.12$ and $\gamma = 0.89 \pm 0.02$ [48]. The same procedure, applied to the λ^*/Λ values of the square-lattice PCFs reported in Fig. 2.4a, provides $d^*/\Lambda \simeq 0.442$, $\alpha = 4.192 \pm 0.246$ and $\gamma = 1.001 \pm 0.025$. The boundary between the single-mode and the multi-mode operation area is reported in Fig. 2.5 for square-lattice PCFs and triangular ones. Notice that the single-mode region for square-lattice PCFs, that is the one above the curve in Fig. 2.5a, is wider for lower d/Λ values, while the difference is significantly reduced, until it disappears, as the air-filling fraction increases. Moreover, it can be noticed that the d^*/Λ value is higher for square-lattice fibers, that is they can be endlessly single-mode in a wider range of the geometric parameter values with respect to triangular PCFs, and they can be successfully used in applications which need large mode area fibers.

As a second part of the cut-off analysis, starting from the single-mode regime information obtained with the Q parameter approach, the normalized cut-off frequency V^* has been evaluated. The V parameter can be easily calculated in a standard optical fiber, since it depends on the core radius and the core and cladding refractive indices, which are all well defined. The choice of these parameters for PCFs is not trivial and several formulations of the normalized frequency have been proposed in literature [8, 44, 52–55], based either on geometric and physical considerations, or analogies with classical theory of conventional fibers. In this study two different formulations of the V parameter are considered. The first one is

$$V_1 = \frac{2\pi}{\lambda}\Lambda\sqrt{n_{eff}^2 - n_{FSM}^2}\ , \tag{2.3}$$

which has been recently proposed for triangular PCFs [8,56]. In Eq. (2.3) n_{eff} and n_{FSM} are the effective indices, respectively, of the fundamental guided mode and of the fundamental space-filling mode in the air-hole cladding, which has been evaluated using a freely available software package [57]. The choice of Λ as the effective core radius can be adopted also for the PCFs studied here, since it is the natural length scale of both the triangular and the square lattices [8,56]. The second V parameter definition considered, more similar to the one used for conventional fibers, is

$$V_2 = \frac{2\pi}{\lambda}\rho\sqrt{n_{co}^2 - n_{FSM}^2}\ , \tag{2.4}$$

where n_{co} is the refractive index of the silica core at the operation wavelength and ρ is the effective core radius. In order to properly adapt the concept of the

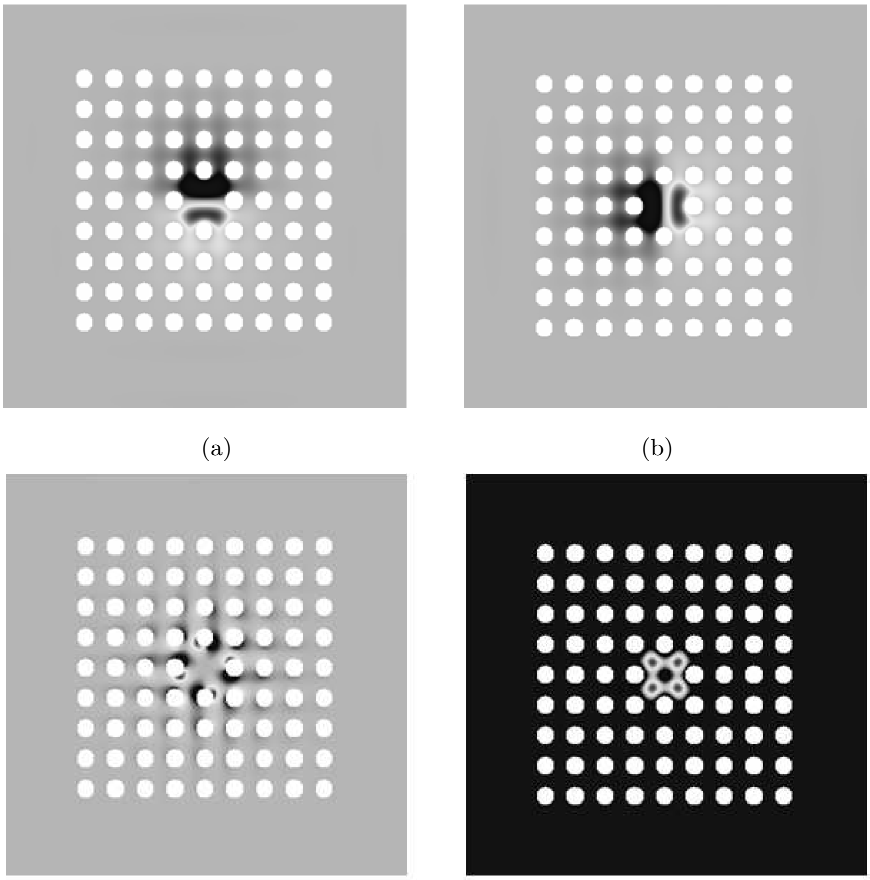

(a) (b) (c) (d)

Figure **2.7**: (a) H_x, (b) H_y, (c) H_z and (d) intensity distribution of the second-order guided mode at $\lambda/\Lambda \simeq 0.127$ for a 4 ring square-lattice PCF with $d/\Lambda = 0.57$.

V parameter to PCFs, several values for ρ have been proposed in literature for fibers characterized by a triangular lattice, that is 0.5Λ [58], $\Lambda/\sqrt{3}$ [54, 55], 0.625Λ [52], 0.64Λ [53] and Λ [44, 52]. In the present study the effective core radius for the square-lattice PCFs has been considered equal to 0.67Λ. This value, different from all the others previously adopted for triangular PCFs,

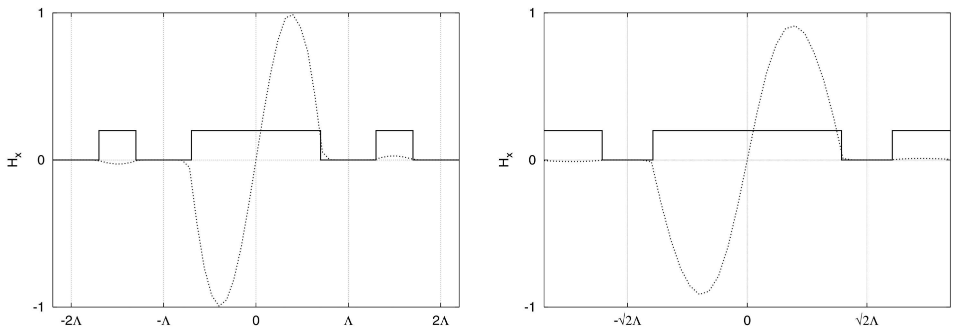

(a) (b)

Figure **2.8**: Section of the square-lattice PCF cross-section (solid line) and of the H_x field component (dotted line) (a) along the x-axis and (b) along the 45° direction.

has been evaluated through the method proposed by Brechet et al [53]. The technique consists in calculating the refractive index of the fundamental space-filling mode n_{FSM} and assessing a temporary V parameter V_t according to Eq. (2.4) with $\rho = \Lambda$. Then, using the effective index of the guided mode n_{eff}, the normalized propagation constant $\beta_n = (n_{eff}^2 - n_{FSM}^2)/(n_{co}^2 - n_{FSM}^2)$ is determined. Substituting the β_n value into the characteristic equation for step-index fibers with $NA = (n_{co}^2 - n_{FSM}^2)^{1/2}$, a new normalized frequency V is obtained. Finally, the effective core radius is given by the ratio $\rho = V/V_t$. By plotting ρ versus the normalized air-hole diameter d/Λ, it can be shown that, in the limit of short wavelengths compared to the air-hole size, that is $d/\lambda \geq 2$, and for low air-filling fractions, that is $d/\Lambda \leq 0.5$, the effective core radius tends to a constant value regardless of d/Λ.

As shown in Fig. 2.5b, V_1^* and V_2^* have been evaluated for the 8 air-hole ring PCFs starting from the normalized cut-off wavelength at the d/Λ values reported in Fig. 2.4a. The mean values of V_1^* and V_2^*, respectively 2.67 and 2.46, are also reported as a solid line in Fig. 2.5b and have been assumed as reference values like the 2.405 value of a standard fiber. Fig. 2.6a and b show the V number versus the normalized wavelength calculated according to Eq. (2.3) and Eq. (2.4), and the corresponding V^* mean value as a horizontal solid line. Of course the crossings between the V^* line and the V number curves for the two formulations give again the λ^*/Λ behaviour versus d/Λ, that is the

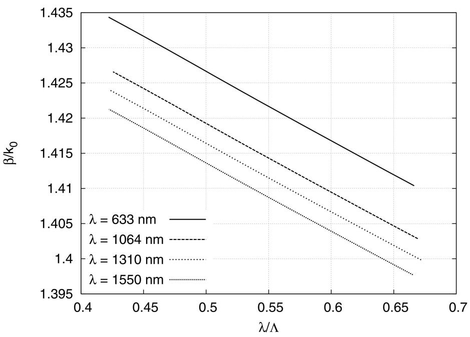

(a)

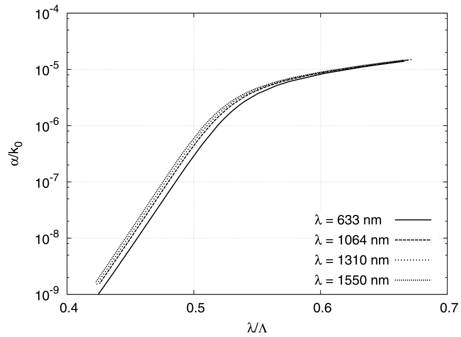

(b)

Figure **2.9**: (a) α/k_0 and (b) β/k_0 of the second-order mode as a function of the normalized wavelength λ/Λ for 8 ring square-lattice PCFs with $d/\Lambda = 0.57$ evaluated at four different wavelengths.

singlemode-multimode phase diagram of Fig. 2.4a.

Finally, it is important to notice that the value of V_1^* here evaluated for the square-lattice PCFs is lower than π, the value for the triangular PCFs [8], which has been obtained with the same V number expression and by looking at the second-order mode field distribution on the fiber cross-section [8, 56]. In particular, it has been shown that in triangular PCFs the second-order mode effective transverse wavelength, related to the dimension of the defect region where the mode fits in, is $\lambda_\perp^* \simeq 2\Lambda$ at the cut-off condition. As a consequence, the normalized cut-off frequency becomes $V_1^* = \frac{2\pi}{\lambda_\perp^*}\Lambda \simeq \pi$ [8]. In order to extend the same approach to the square-lattice PCFs, the magnetic field components shown in Fig. 2.7 have to be taken into account. It is important to underline that the field shape of the second-order mode in these PCFs is strongly influenced by the 4-fold symmetry which characterizes the square lattice, in particular by the position of the air-holes belonging to the first ring. As a consequence, different $\lambda_\perp^*$ values can be obtained if the second-order mode field amplitude is considered along the horizontal, or vertical, direction or along the 45° one. The two situations are depicted in Fig. 2.8a and b. In the first case, the field shape is the same of the one reported for triangular PCFs [8], so $\lambda_\perp^* \simeq 2\Lambda$ and $V_1^* \simeq \pi$. On the contrary, if the 45° direction is considered, the separation between the two first null values of the

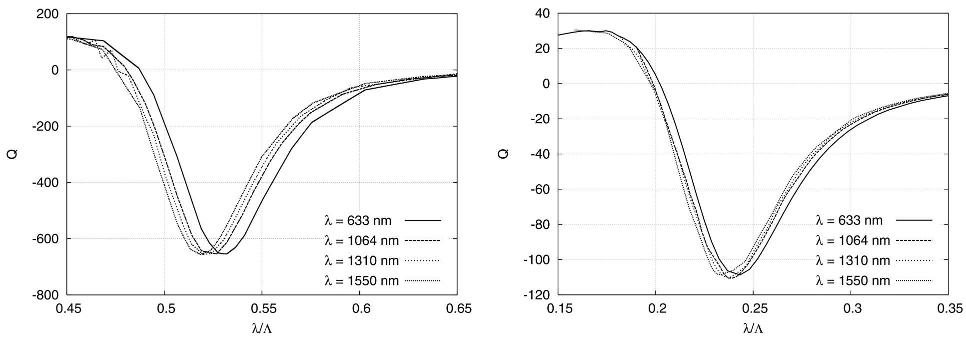

(a) (b)

Figure **2.10**: Q-parameter values as a function of the normalized wavelength λ/Λ for 8 ring square-lattice PCFs with (a) $d/\Lambda = 0.57$ and (b) $d/\Lambda = 0.50$ evaluated when the wavelength is 633 nm and 1550 nm.

second-order mode field amplitude increases, as shown in Fig. 2.8b, since the two opposite air-holes belonging to the first ring are more distant. Thus $\lambda_\perp^*$ is higher, that is $2\sqrt{2}\Lambda$, and consequently $V_1^* \simeq \dfrac{\pi}{\sqrt{2}}$. It is interesting to point out that the V_1^* value calculated in the present analysis, that is 2.67, is almost equal to the mean value between π and $\dfrac{\pi}{\sqrt{2}}$, that is 2.68. The corresponding $\lambda_\perp^* \simeq 2.34\Lambda$ is obtained by the mean value of the inverse of 2Λ and $2\sqrt{2}\Lambda$. In conclusion, it is not possible to simply extend the derivation of V_1^* previously proposed for triangular PCFs to the case of square-lattice PCFs, since a unique value of $\lambda_\perp^*$ can not be easily found.

Finally, the cut-off analysis has been carried out by fixing the guided-mode wavelength λ at different values, that is 633, 1064, 1310 and 1550 nm in order to understand the wavelength influence on the single-mode regime analysis. Notice that the pitch Λ has been properly chosen in order to obtain normalized wavelength values between 0.4 and 0.7. The silica refractive index values have been calculated according to the Sellmeier equation for the wavelengths here considered. By calculating the Q parameter minima for the square-lattice PCFs with d/Λ in the range $0.50 \div 0.57$, the phase diagram with single-mode and multi-mode operation has been obtained for the four different λ values. PCFs with 8 air-hole rings have been considered, since, as previously shown,

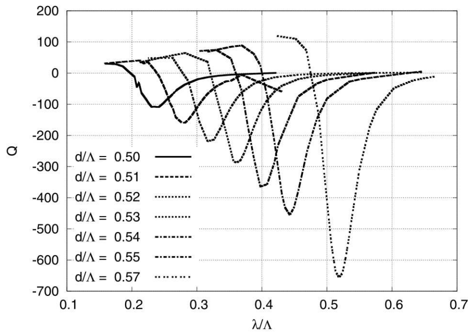

(a)

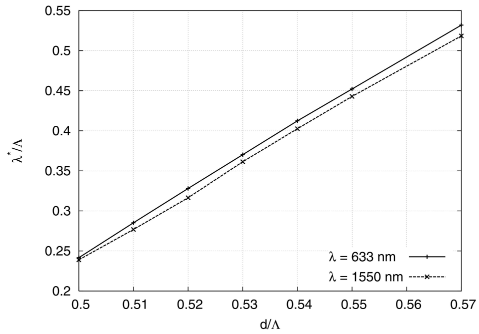

(b)

Figure **2.11**: (a) Q-parameter values as a function of the normalized wavelength λ/Λ for 8 ring square-lattice PCFs with d/Λ in the range $0.50 \div 0.57$ when the wavelength is 1550 nm.

the Q parameter transition becomes more acute and the method more reliable when the ring number increases. Fig. 2.9a and b show the behaviour of the effective index β/k_0 and of α/k_0 versus the normalized wavelength λ/Λ as a function of the wavelength for the second-order mode of the square-lattice PCFs with $d/\Lambda = 0.57$. As expected, for a chosen λ/Λ value the second-order mode effective index increases when the wavelength λ decreases, since the refractive index of silica becomes higher. Notice that the lowest values of α/k_0 and, consequently, of the leakage losses in all the considered wavelength range have been obtained when the wavelength is fixed to 633 nm. This behaviour can be explained by analyzing the confinement of the first higher-order mode in the silica core of the square-lattice PCFs, which is higher for the lower wavelengths. This is mainly due to the higher silica refractive index value, despite the smaller dimension of the PCF core. In fact, for a fixed normalized wavelength and a chosen air-filling fraction d/Λ, the pitch Λ and, as a consequence, the core diameter is smaller if a low wavelength value is considered. For example, the hole-to-hole spacing becomes about 2.5 times larger when λ increases from 633 nm to 1550 nm. It is important to underline that, for all the four wavelength values considered in the present analysis, α/k_0 increases with λ/Λ, being the second-order mode confinement lower when the pitch is small.

Moreover, all the curves show a transition, which has been evaluated by calculating the Q parameter through the Eq. (2.2). Results reported in Fig. 2.10a for the PCFs with $d/\Lambda = 0.57$ show that the negative minimum value is almost the same, that is around -655, whatever the wavelength. However, the minimum position changes with the wavelength, that is it moves towards the lower λ/Λ values when the wavelength increases from 633 nm to 1550 nm. In fact, the minimum is at 0.532, 0.527, 0.52 and 0.518 when λ is 633, 1064, 1310 and 1550 nm, respectively. Similar results have been obtained for the PCFs with $d/\Lambda = 0.50$, as reported in Fig. 2.10b. In Fig. 2.11a the Q parameter values for the square-lattice PCFs evaluated with $\lambda = 1550$ nm, are reported. As previously described for a different wavelength, that is 633 nm, the negative value of the curve minimum becomes higher as d/Λ increases, being -108 at $\lambda/\Lambda = 0.23$ for $d/\Lambda = 0.50$ and -655 at $\lambda/\Lambda = 0.518$ for $d/\Lambda = 0.57$. As the square-lattice PCF air-filling fraction decreases, the Q minimum moves towards the lower λ/Λ values, becoming also wider and more difficult to identify with high precision. As previously described, the position of the Q parameter minimum defines the normalized cut-off wavelength λ^*/Λ. Fig. 2.11b reports the values of λ^*/Λ as a function of d/Λ in the range 0.50 div 0.57, obtained by taking into account the lowest and the highest wavelength value, that is 633 nm and 1550 nm. Notice that the normalized cut-off wavelength is lower for all the considered d/Λ values when the analysis is carried out by choosing $\lambda = 1550$ nm. However, the mean relative difference between the λ^*/Λ values evaluated at 633 nm and at 1550 nm is about 2.7 when the air-filling fraction changes from 0.50 to 0.57. As a consequence, a significant change in the wavelength λ value, that is from 633 nm to 1550 nm, slightly affects the cut-off analysis results and, consequently, the boundary of the single-mode region for the square-lattice PCFs.

2.2 Cut-off properties of LMA triangular PCFs

The Q parameter method previously described has been applied also to study the cut-off properties of a new LMA triangular PCF, called 7-rod core, obtained by removing the central air-hole and the first six surrounding ones in the fiber transverse section.

In fact, it is important to investigate the trade-off between effective area and single-mode operation regime in LMA fibers, in order to successfully use them for different applications. In particular, LMA fibers, which can effectively support high optical intensities limiting the impact of nonlinear effects, are

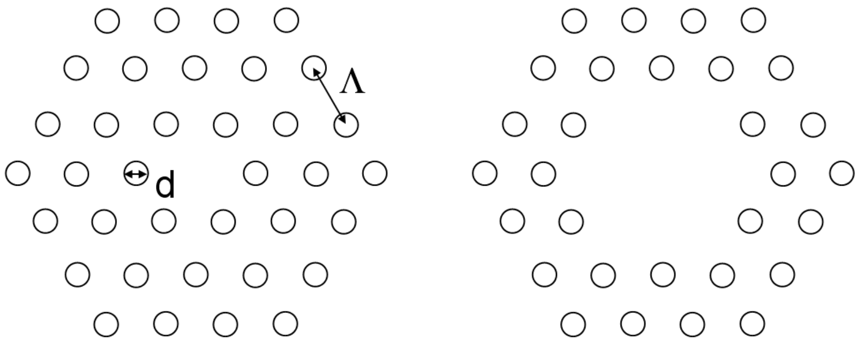

(a) (b)

Figure **2.12**: (a) 1-rod and (b) 7-rod core triangular PCF cross-section.

required for the generation and the delivery of high-power optical beams for a wide range of applications, including laser welding and machining, optical lasers and amplifiers. For such applications another desirable feature is the single-mode operation over the wavelength range of interest.

Using the conventional optical fiber technology, a large modal area can be achieved either by reducing the numerical aperture, that is by lowering the percentage of doping material in the core region, or by increasing the core dimension. Better results in LMA fiber design can be reached by exploiting the novel and unique optical properties offered by PCFs. In particular, by considering triangular PCFs, it is possible to significantly increase the effective area by narrowing the air-holes for a fixed Λ, or by enlarging the pitch for a fixed d/Λ value. Moreover, the Endlessly Single-Mode (ESM) property provide the single-mode operation for triangular LMA PCFs [59]. However, an upper limit on the guided-mode area exists, given by the value of the losses. In fact, the air-filling fraction decrease can cause an increase of the leakage losses [45, 46], while, as Λ becomes larger, there is a greater susceptibility to scattering losses induced by microbending and macrobending [60]. Another LMA PCF design based on the triangular lattice has been recently proposed in [60, 61]. The triangular core region of these fibers, called 3-rod core triangular PCFs, has been obtained by removing three air-holes in the center of the fiber cross-section. 3-rod core PCFs can provide an enhancement of the guided-mode

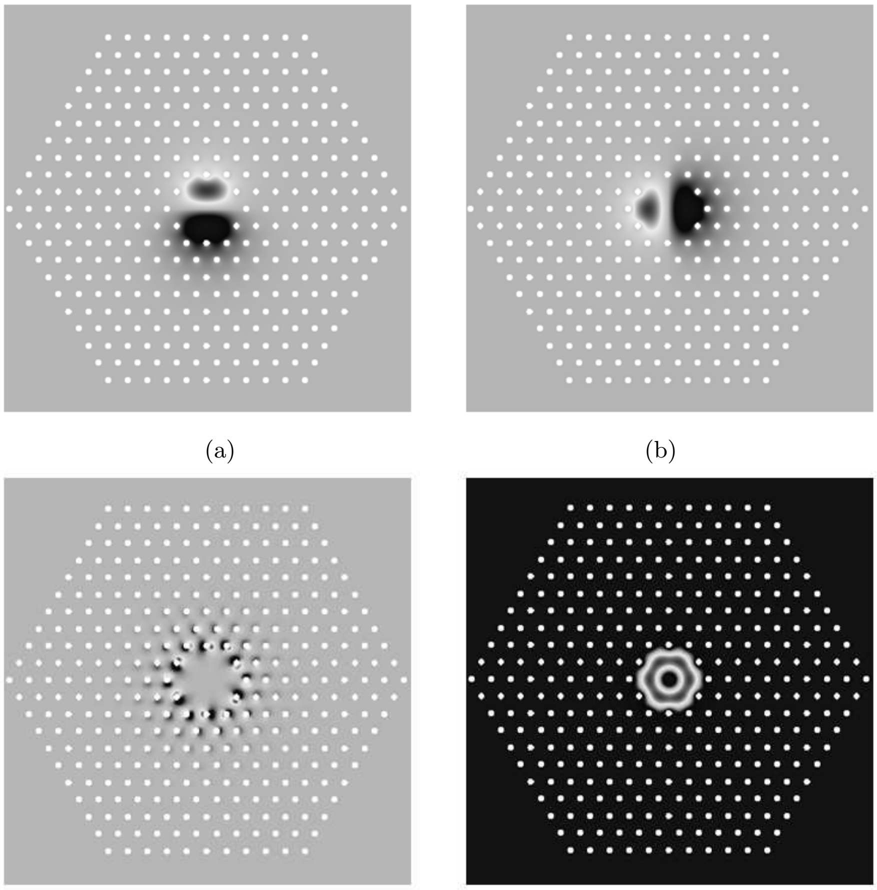

(a) (b) (c) (d)

Figure **2.13**: (a) H_x, (b) H_y, (c) H_z magnetic field components, and (b) field intensity distribution of the second-order guided mode at $\lambda = 1550\ nm$ for the 7-rod core PCF with $d/\Lambda = 0.2$ and $\Lambda = 4.2\ \mu m$.

area of about 30% and a higher robustness when scaled to a larger pitch [60]. As a drawback of the larger silica core dimension, the ESM region of these PCFs is smaller than that of the traditional triangular fibers, being limited by $d/\Lambda < 0.25$. Moreover, the triangular core symmetry influences the shape of the guided-mode field intensity, which deviates from the standard gaussian-

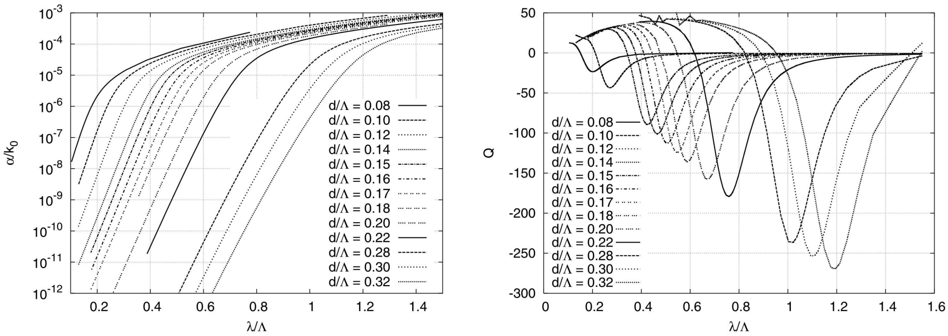

(a) (b)

Figure **2.14**: (a) Second-order mode α/k_0 and (b) Q parameter values as a function of the normalized wavelength λ/Λ for 9 ring 7-rod core triangular PCFs with d/Λ in the range $0.08 \div 0.32$.

like.

In order to overcome these problems, a new triangular PCF has been considered instead of the traditional 1-rod core fiber, reported in Fig. 2.12a. It is characterized by a triangular lattice and a silica core formed by removing seven central air-holes, as shown in Fig. 2.12b, so it will be referred as 7-rod core PCF in the following. By removing the air-holes belonging to the first ring, a wider silica region has been obtained, so 7-rod core PCFs present a larger effective area for fixed d/Λ and Λ values, compared to 1-rod core fibers. The structure here studied has been chosen so that it can be readily fabricated. In fact, the proposed geometry is feasible using the well-know stack-and-draw technique without any additional difficulty.

Since the core dimension has a strong influence on the confinement of all the PCF guided modes and, as a consequence, on the single-mode regime of triangular fibers, it is necessary to accurately define the single-mode operation regime of these LMA triangular PCFs, in order to successfully use them for practical applications. To this aim, a detailed analysis of the 7-rod core PCF cut-off properties has been carried out with the method previously described, that is the Q parameter method, based on the leaky nature of the second-order mode. In this case the negative minima of the Q parameter have been evaluated for PCFs with d/Λ in the range $0.08 \div 0.32$. Since 10 air-hole ring 1-rod core triangular PCFs have been previously used for the modal cut-off

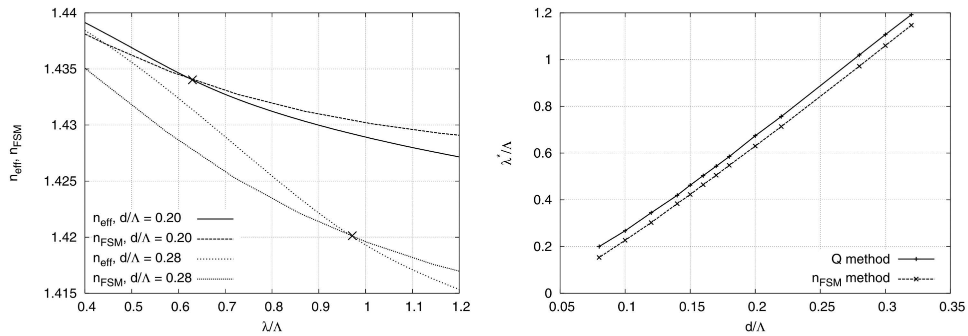

(a) (b)

Figure **2.15**: (a) Second order mode n_{eff} and n_{FSM} versus the normalized wavelength λ/Λ for 9 ring 7-rod core triangular PCFs with d/Λ equal to 0.2 and 0.28. (b) Normalized cut-off wavelength λ/Λ as a function of the d/Λ ratio for 7-rod core triangular PCFs, obtained with the Q parameter approach and the n_{FSM} method.

analysis [48], in the present study 7-rod core PCFs with 9 rings have been considered. In Fig. 2.13a, b and c the second-order mode magnetic field components distribution at $\lambda/\Lambda \simeq 0.369$ is reported for a LMA PCF with $d/\Lambda = 0.2$. At this normalized wavelength the first higher-order mode results confined in the fiber silica core. This is confirmed by the second-order mode intensity distribution, shown in Fig. 2.13d.

In order to calculate the Q parameter according to Eq. (2.1), the behaviour of α/k_0 versus the normalized wavelength λ/Λ for the second-order mode has to be evaluated. As shown in Fig. 2.14a, for 7-rod core PCFs with different d/Λ values, α/k_0 increases with λ/Λ, that is the confinement of the second-order mode is lower for smaller pitch Λ. For all the considered d/Λ ratios the curves show a transition, that is a change in the slope, which becomes sharper as the air-hole diameter increases with respect to the pitch. Moreover, by varying d/Λ from 0.08 to 0.32, the transition region moves toward the higher λ/Λ values, as it has been already demonstrated for triangular and square-lattice PCFs [36, 48].

From the previous results, the Q parameter has been calculated through a finite difference formula and the values obtained for the 7-rod core triangular PCFs are reported in Fig. 2.14b. The negative value of the curve minimum

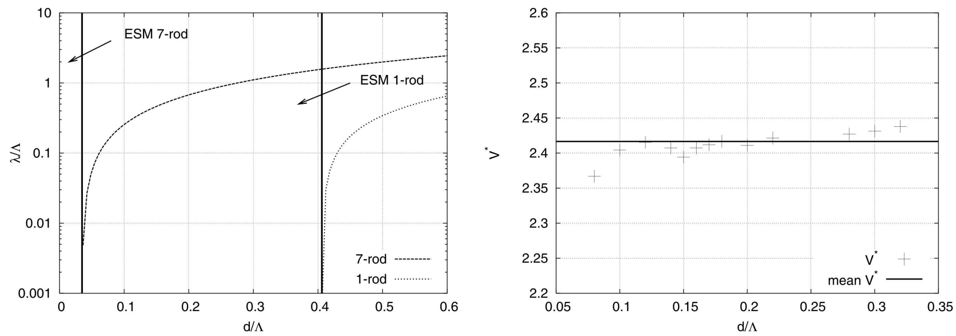

(a) (b)

Figure **2.16**: (a) Phase diagram for triangular PCFs with 7-rod and 1-rod core. (b) Cut-off value V^* of the normalized frequency for 7-rod core triangular PCFs with 9 rings.

becomes higher as d/Λ increases, reaching -270 at $\lambda/\Lambda \simeq 1.19$ for $d/\Lambda = 0.32$. As the PCF air-filling fraction decreases, the Q minimum moves toward the lower λ/Λ values and becomes wide and difficult to identify with high precision. For example, the negative minimum is about -23.5 at $\lambda/\Lambda \simeq 0.2$ for the PCFs with $d/\Lambda = 0.08$.

A second approach has been applied to confirm the results obtained with the Q method. In fact, the limit of the single-mode region can be determined by comparing the effective index $n_{eff} = \beta/k_0$ of the second-order mode and that of the fundamental space-filling mode n_{FSM} for a fixed d/Λ value [60,61]. The first higher order mode at a certain wavelength λ is no longer guided if its n_{eff} is lower than the n_{FSM} at the same λ. As a consequence, the normalized cut-off wavelength λ^*/Λ is obtained applying the condition $n_{eff} = n_{FSM}$.

The second-order mode effective index and the n_{FSM} have been reported as a function of the normalized wavelength λ/Λ in Fig. 2.15a for the 7-rod core triangular PCFs with $d/\Lambda = 0.2$ and $d/\Lambda = 0.28$. Notice that the value of the normalized cut-off wavelength, evaluated by considering the crossing of the n_{eff} and n_{FSM} curves, becomes higher as the air-filling fraction of the photonic crystal cladding increases, being 0.97 and 0.63 for d/Λ equal to 0.28 and 0.2, respectively.

The λ^*/Λ values calculated with both the previous methods for 7-rod core triangular PCFs with 9 air-hole rings and d/Λ in the range $0.08 \div 0.32$ are

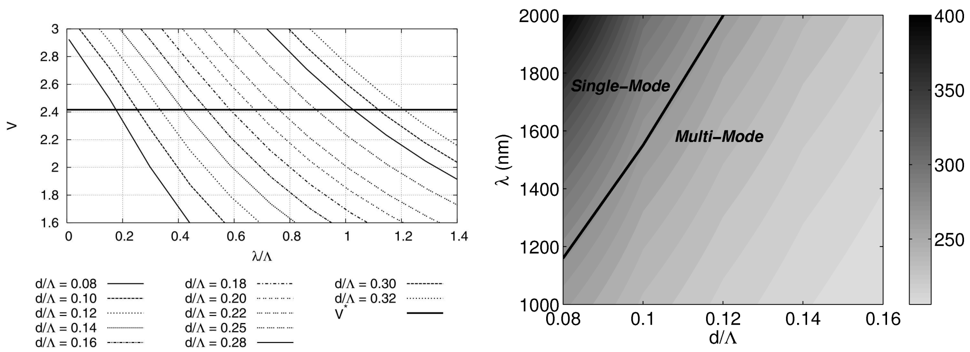

(a) (b)

Figure **2.17**: (a) V behaviour versus the normalized wavelength λ/Λ for 7-rod core triangular PCFs with d/Λ between 0.08 and 0.32. The solid line represents the mean value of V^*. (b) A_{eff} in μm^2 as a function of the air-filling fraction d/Λ and the wavelength λ for 7-rod core triangular PCFs with $\Lambda = 5.8\ \mu m$ and 9 air-hole rings.

reported in Fig. 2.15b. Notice that the results obtained are in good agreement, even if the Q parameter method is less precise for the PCFs with the lower air-filling fraction, being the evaluated minima wider and less deep for $d/\Lambda \leq 0.12$.

An interesting comparison can be made on the ESM region of triangular PCFs with core defect regions of different dimension, obtained by removing one or seven air-holes in the cross-section center. The fitting reported in Eq. (2.2) has been applied to the λ^*/Λ values of the 7-rod core PCFs obtained with the Q method and reported in Fig. 2.15b, providing $d^*/\Lambda \simeq 0.035$, $\alpha = 4.432 \pm 0.067$ and $\gamma = 1.045 \pm 0.01$. The boundary between the single-mode and the multi-mode operation area for small and large core triangular PCFs is reported in Fig. 2.16a. Notice that the single-mode region for 7-rod core PCFs, that is the one above the continue line, is significantly smaller than that of 1-rod core fibers for lower d/Λ values, while the difference between the two cut-off curves is reduced as the air-filling fraction increases. Moreover, it is important to underline that 7-rod core PCFs are characterized by a lower d^*/Λ value, that is they can be ESM in a smaller range of the geometric parameter values with respect to 1-rod core triangular fibers. In particular, the LMA fibers here proposed are endlessly single-mode only for $d/\Lambda < 0.035$.

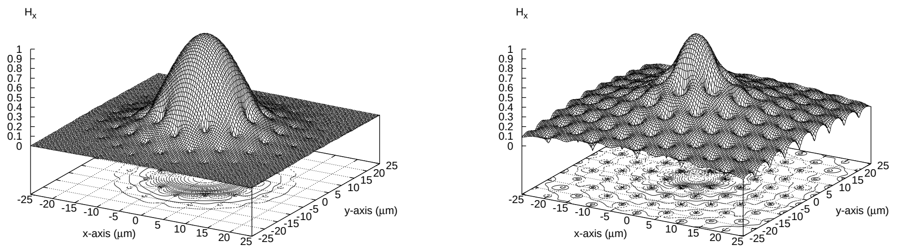

(a) (b)

Figure **2.18**: Magnetic field fundamental component at $\lambda/\Lambda = 0.267$ of (a) 7-rod and (b) 1-rod core triangular PCFs with $d/\Lambda = 0.1$.

In order to give a complete description of the 7-rod core triangular PCF cut-off properties, the normalized cut-off frequency V^* has been evaluated, starting from the single-mode regime information obtained with the two previous approaches. The formulation of the V parameter in Eq. (2.4) has been considered. Notice that the effective core radius for 7-rod core triangular PCFs, evaluated through the method proposed by Brechet et al [53] previously described, has been considered equal to 1.48Λ. As shown in Fig. 2.16b, V^* has been evaluated for the 9 air-hole ring 7-rod core triangular PCFs, starting from the normalized cut-off wavelength at the d/Λ values reported in Fig. 2.15b. The mean value of V^*, that is 2.416, is also shown as a solid line in Fig. 2.17a. Notice that this can be assumed as a reference value like the 2.405 value of a conventional optical fiber. In Fig. 2.17a the V parameter values, calculated according to Eq. (2.4), are reported versus the normalized wavelength, with the corresponding V^* mean value as a horizontal solid line. It is important to underline that, as expected, the crossings between the V^* line and the normalized frequency curves give again the phase diagram of Fig. 2.15b.

Since it has been demonstrated a strong correlation between the achievable guided-mode effective area and the single-mode regime, it becomes challenging to fulfill simultaneously all the requirements to design LMA 7-rod core triangular PCFs useful for practical applications. However, it is possible to find a compromise between the achievable effective area and the number of modes

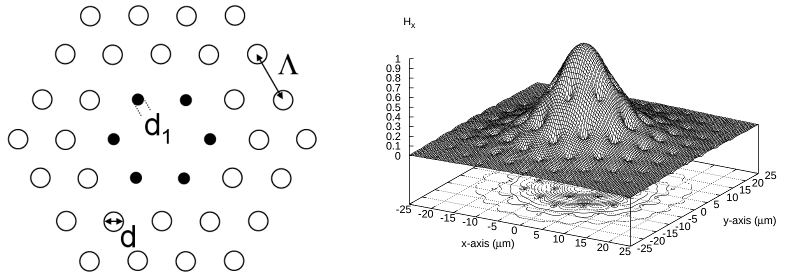

(a) (b)

Figure **2.19**: (a) Cross-section of the triangular PCF with $d_1 = 0.5d$. (b) Magnetic field fundamental component at $\lambda/\Lambda = 0.267$ of the triangular PCF with $d/\Lambda = 0.1$ and $d_1 = 0.5d$.

that PCFs guide over the wavelength range of interest. To this aim, the effective area A_{eff} of the fundamental guided mode of LMA PCFs has been calculated, according to Eq. (A.9). For example, the A_{eff} values obtained for 7-rod core PCFs with $\Lambda = 5.8$ μm and 9 air-hole rings are shown in Fig. 2.17b in the wavelength range 1000 $nm \div 2000$ nm, as well as the boundary between the single-mode and the multi-mode region previously evaluated. In particular, it is possible to obtain an effective area at 1550 nm of about 320 μm^2 and 268 μm^2, respectively, by choosing d/Λ equal to 0.08 and 0.1, while still keeping the 7-rod core PCFs in the single-mode operation regime. Notice that, in order to reach similar A_{eff} values with 1-rod core triangular PCFs with the same air-filling fraction, it is necessary to consider larger pitch, that is between 8 μm and 10 μm [59]. Moreover, it is important to underline that, unlike conventional triangular PCFs, 9 air-hole rings are enough to prevent the LMA PCF guided-mode from being leaky, even for these low d/Λ and Λ values. In fact, the fundamental mode of the 7-rod core triangular PCF with $d/\Lambda = 0.1$ and $\Lambda = 5.8$ μm is completely confined in the silica core, as shown in Fig. 2.18a. On the contrary, if a 1-rod core triangular PCF with the same geometric parameters and air-hole ring number, that is 10, is considered, the guided mode at 1550 nm is leaky, as it is shown in Fig. 2.18b. The small core dimension and the low air-filling fraction do not provide the necessary field confinement.

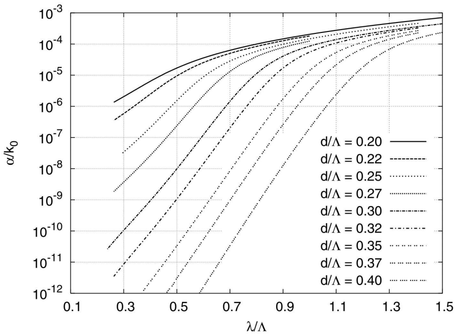

(a)

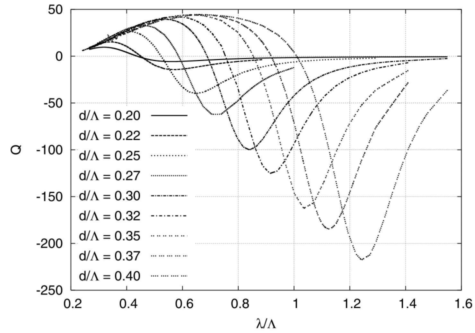

(b)

Figure **2.20**: Second-order mode α/k_0 as a function of the normalized wavelength λ/Λ for triangular PCFs with $d_1 = 0.5d$ for d/Λ between 0.2 and 0.4.

Finally, a further solution with an enlarged core region for a fixed d/Λ and Λ has been adopted, which should give a larger mode size then 1-rod core triangular PCFs, without significantly increasing the guided-mode leakage losses. In particular, triangular PCFs with a silica core larger than that of 1-rod core fibers, but smaller than that of 7-rod core ones have been considered. In fact, as represented in Fig. 2.19a, the diameter of the air-holes belonging to the first ring is $d_1 = 0.5d$ in the studied PCFs, while the air-hole ring number is still 10.

Preliminary results of the cut-off analysis for these LMA triangular PCFs have been obtained and they are here reported. Looking at the magnetic field of the fundamental mode at 1550 nm guided by this kind of PCFs, shown in Fig. 2.19b, it is possible to notice a higher confinement with respect to 1-rod core PCFs, even if the behaviour of the guided mode is still leaky. Moreover, the α/k_0 curves for the second-order mode, evaluated as previously described for d/Λ in the range $0.2 \div 0.4$ and reported in Fig. 2.20a, do not present a net transition. As a consequence the Q parameter minimum shown in Fig. 2.20b, which describes the boundary between the single- and the multi-mode region, becomes wide and difficult to identify with high precision, differently from those reported in Fig. 2.14b for 7-rod core PCFs. As a consequence, more than 10 air-hole rings should be considered in order to successfully analyze the cut-off properties of these PCFs. This will be the object of a future research.

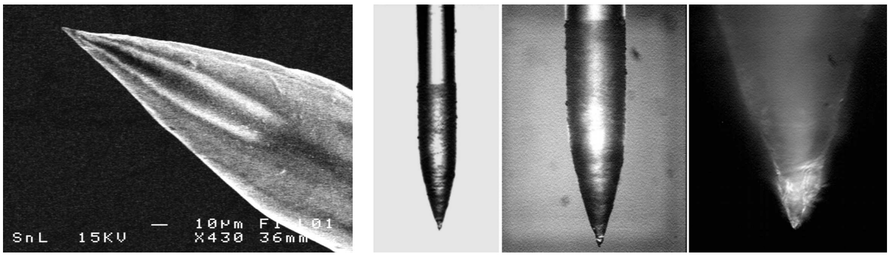

(a) (b)

Figure **2.21**: (a) The chemical-etched optical probe. (b) The coated fiber tip.

2.3 Scanning Near-Field Optical Microscope

The A_{eff} calculation presented in the previous cut-off analyses has been validated by comparing the values calculated with the FEM simulations with those experimentally measured with a Scanning Near-Field Optical Microscope (SNOM) for some PCF samples available in laboratory.

The SNOM technique can be used to evaluate the effective area of an optical fiber, since it permits to study the field distribution on its transverse section. Differently from the general purpose concept, in the microscope used in the PhD course, realized during the previous Master thesis activity, the interest is in the direct acquisition of the radiation emitted at the fiber end face. Thus, the SNOM system can be greatly simplified, since it does not require the collecting optical sub-systems of general purpose one. This allows to adopt a extremely low cost solution. In the SNOM system developed an optical probe, that is a nanometric tapered single-mode optical fiber, is approached in the near-field of the fiber under investigation. The image process is based on a pixel by pixel acquisition sequence, moving step by step the probe above the surface of the device under test and scanning all the region of interest. A computer performs the image processing, storing all the data collected from each pixel.

The probe dimensions, the probe-sample distance and the scanning mode are the keys to overpass the resolution limit of conventional optical microscopy, allowing both high spatial and spectral resolution. To reproduce the field distribution with high fidelity, the scanning pixel size, that is the scanning step, should be approximately as large as the diameter of the probe aperture.

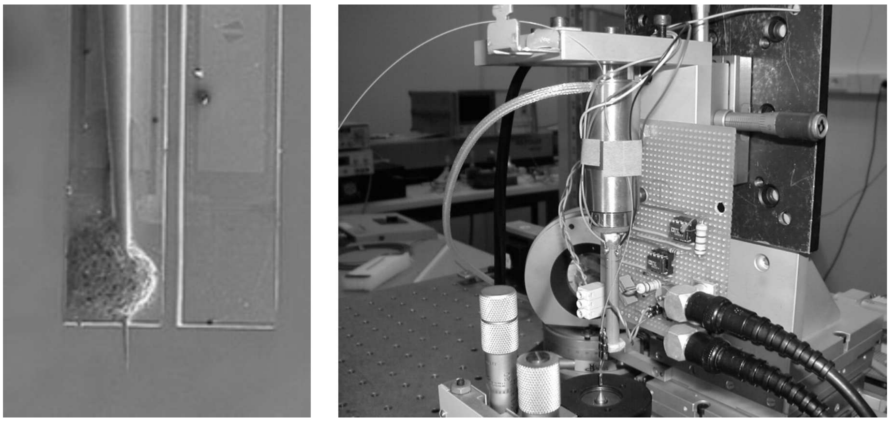

(a) (b)

Figure **2.22**: (a) The fork-fiber tip system. (b) Scanning zone.

The probe consists of two main parts, that is the tapered optical fiber which acquires the light signal from the sample, and the integrated system for the detection of the distance between the tip of the fiber and the surface of the sample. The probe is connected to a piezoelectric transducer that operates both as distance regulator and scanner. This is a piezo-ceramic tube with four external electrodes and a single internal one. By applying opposite voltages on opposite quadrants, the tube bends, allowing a scan in the $x-y$ plane, while a voltage applied in the inner electrode causes tube length variations, changing the probe-sample distance. The output of the DSP board, connected to the PC through GPIB, is used to drive the scanner. The user can control the system through a software with a graphical interface, which has the function of elaborating data, controlling the whole apparatus and generating the final images.

The near-field probe is the most crucial part of the microscope, since it defines its resolution. The probes have been obtained with the simple and economical technique of the chemical etching of a single-mode optical fiber [62]. The fiber is immersed in a liquid solution for about 90 minutes. The chemical solution is formed by Hydrofluoric acid (HF) in water solution at 40% and on top of this a thin protective layer ($1-2$ mm thick) of olive oil or toluene is deposited. The etching phenomenon in the formation of the tip takes place

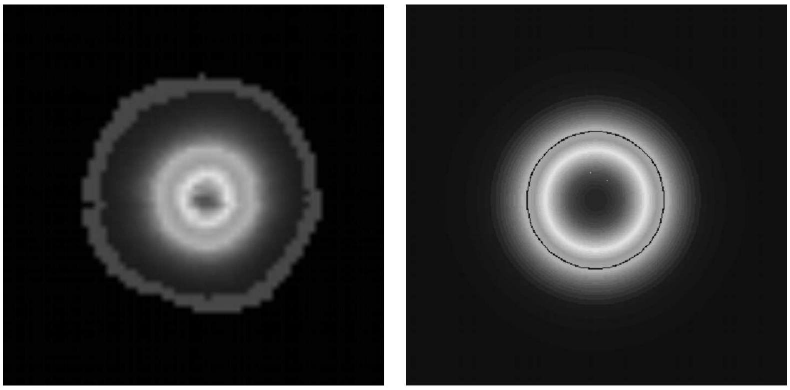

(a) (b)

Figure **2.23**: Intensity distribution of the guided mode at 1550 nm for a single-mode fiber, (a) experimentally measured and (b) calculated with the FEM solver.

at the acid-solvent-fiber interface [63]. The fabricated SNOM probes have an apex diameter of about 200 nm, as reported in Fig. 2.21a. To avoid light coupling to the probe from the tip side, that would mean loosing resolution, a simple and cheap coating method has been adopted, in which a black acrylic paint is used as the coating element [64]. In Fig. 2.21b the coated fiber tip is shown. Even if the fiber appears completely coated by the paint, it has been demonstrated that, at the apex of the tip, a nanometric aperture is spontaneously formed, due to surface tension forces acting on the paint film.

The optical probe is then glued on a leg of a commercial quartz tuning fork with resonance frequency 32768 Hz, perpendicularly to the device surface, as shown in Fig. 2.22a. The fork is then set on the piezoelectric transducer. The fork-fiber tip system is electrically excited in a transverse mode near its resonant frequency by a sinusoidal signal generated by the internal oscillator of the lock-in amplifier. Reducing the fiber tip-sample separation down to about $10-20$ nm leads to an increased damping of the tip vibration, due to the so-called shear forces that generate between the tip and the surface of the sample [65]. This phenomenon affects the amplitude and the phase of the tip oscillations, which can be measured by the same lock-in amplifier as a piezoelectric current response to the crystal structure deformation. The distance probe-sample is so kept constant in the near-field during the scan by a feedback control, which, following a reference level of the tip vibration amplitude, drives the piezoelectric transducer after a PID (Proportional Integral Derivative) elaboration of the signal. In Fig. 2.22b the scanning zone is reported.

The effective area of the fundamental mode propagating in a standard Single-Mode Fiber (SMF) has been measured in order to test the SNOM technique. Fig. 2.23a shows the intensity distribution of the beam at 1550 nm which emerges from the end face of the single-mode fiber under test. Starting from the intensity values $I\left(x,y\right)$ in each pixel, the effective area A_{eff} has been calculated as

$$A_{eff} = \frac{\left(\int_{-\infty}^{+\infty}\int_{-\infty}^{+\infty} I\left(x,y\right)dxdy\right)^2}{\int_{-\infty}^{+\infty}\int_{-\infty}^{+\infty} I^2\left(x,y\right)dxdy} \ . \tag{2.5}$$

The effective area value estimated with the SNOM technique is $A_{eff} = 85\ \mu m^2$. For comparison, the intensity distribution of the field guided by the same SMF fiber has been calculated also with the full-vector modal solver based on the FEM, as shown in Fig. 2.23b. In this case $I\left(x,y\right)$ has been obtained through the Poynting vector definition [66], which involves the three computed components of both the electric and the magnetic field of the guided mode. The A_{eff} evaluated with the FEM simulation well agrees with the one experimentally measured, thus validating the effective area numerical calculation [67].

After testing the SNOM technique with a standard optical fiber, its application has been extended to PCFs. The first PCF here considered is shown in Fig. 2.24a and it is characterized by a triangular lattice of air-hole with diameter d and hole-to-hole spacing, or pitch Λ. The silica core of the fiber is formed by a missing air-hole. This PCF is a large mode area fiber, being $\Lambda = 11\ \mu m$ and $d/\Lambda = 0.24$. The measurements here reported have been performed at a wavelength $\lambda = 1550\ nm$, where the PCF is in a single-mode regime. Fig. 2.24b shows the intensity of the mode at the fiber end face, while Fig. 2.24c reports the intensity distribution obtained with the FEM simulation. The effective area value measured with the SNOM technique is $A_{eff} = 230\ \mu m^2$, while the FEM simulation provided a value of $A_{eff} = 260\ \mu m^2$ with a relative error of 11%. The second PCF sample, reported in Fig. 2.25a, is characterized by $\Lambda = 12.4\ \mu m$ and $d/\Lambda = 0.41$. The intensity of the mode at the fiber end face obtained through the SNOM technique at $\lambda = 1550\ nm$ is shown in Fig.

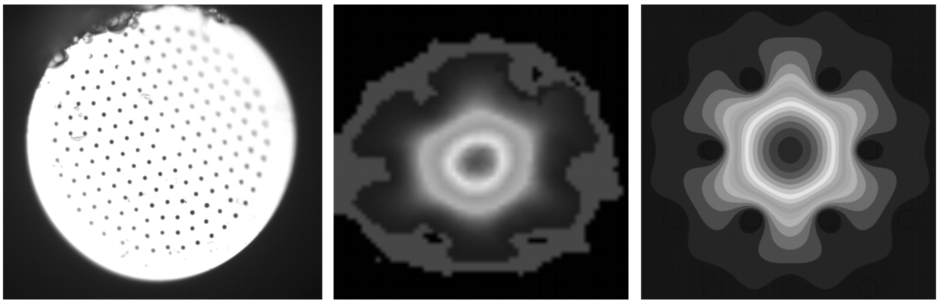

(a) (b) (c)

Figure **2.24**: (a) Sample image of the PCF with $\Lambda = 11\ \mu m$ and $d/\Lambda = 0.24$, (b) experimentally observed near-field intensity distribution at $\lambda = 1550\ nm$, (c) intensity distribution calculated with the FEM solver.

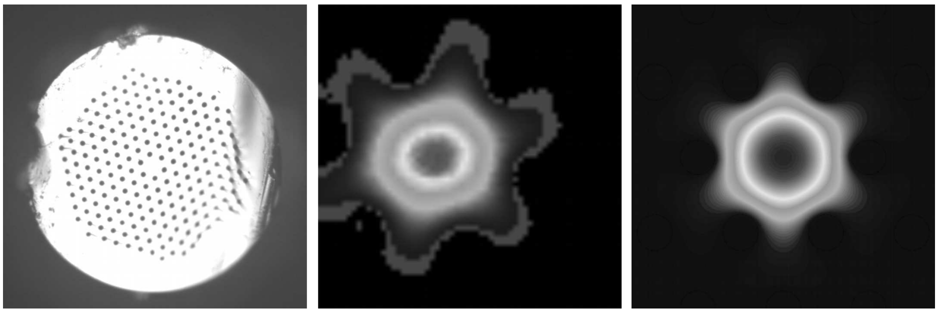

(a) (b) (c)

Figure **2.25**: (a) Sample image of the PCF with $\Lambda = 12.4\ \mu m$ and $d/\Lambda = 0.41$, (b) experimentally observed near-field intensity distribution at $\lambda = 1550\ nm$, (c) intensity distribution calculated with the FEM solver.

2.25b, while the one calculated with the FEM simulation is reported in Fig. 2.25c. An effective area of 195 μm^2 and 206 μm^2 has been obtained, respectively, with the SNOM measurement and the FEM simulation, thus providing a relative error of 5%. The best agreement between experimental and simulation results of this PCF sample is due to the higher field confinement inside the SNOM scanning region [68, 69].

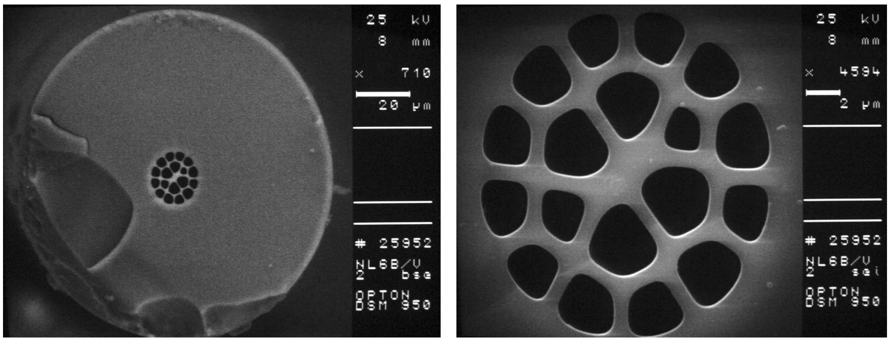

(a) (b)

Figure **2.26**: (a) Cross-section of the fabricated silicate PCF and (b) particular of the holey cladding region.

2.4 Nonlinear silicate PCFs with high birefringence

Results reported earlier in this Chapter have demonstrated that PCFs with square-lattice of air-holes, as well as with a 7-rod core can be exploited to enlarge the guided-mode effective area. However, by exploiting the high flexibility offered by the PCF technology, it is possible to design fiber cross-section to obtain a small effective area and, as a consequence, a high nonlinear coefficient. These highly nonlinear PCFs are suitable for a great number of telecommunication applications, such as wavelength conversion [70] or optical parametric amplification [71]. High nonlinearity is a result of the combination of a high Numerical Aperture (NA) of the fiber and of a small size of its core. It allows to increase light confinement in the core, which results in a smaller effective area A_{eff} and higher nonlinear coefficient γ in the fiber. Nonlinear PCFs allow also to achieve anomalous-dispersion in the vicinity of the visible range, around 800 nm. This feature enables to generate ultra-broad supercontinuum for more modest initial pulse energies and duration than in case of classical optical fibers [72]. Moreover, the good nonlinear properties can be easily combined with a high birefringence in PCFs. In fact, due to the high structure asymmetry which can be introduced in the photonic crystal, PCFs can achieve a birefringence two orders of magnitude higher in comparison to conventional Highly Birefringent (HB) fibers, such as Panda and Bow-Tie fibers [73].

The design and fabrication of a PCF that combines these two important properties is here reported. This fiber is particularly interesting because the nonlinear properties depend on the polarization state of the input light, is here reported. In fact, it has been shown that, if the input light pulse is linearly polarized in a direction matched to the one of the main axes of the birefringent fiber (slow or fast), the polarization of light is preserved in the output spectrum and different characteristics for orthogonal polarizations are observed [74]. An appropriate design of the structure, which takes into account dispersion profiles for orthogonally polarized eigen-modes, allows to obtain a fiber with polarization dependent generation of nonlinear effects. This fact especially concerns the supercontinuum generation, whose characteristics can be tuned by changing the input light polarization [75].

While most of the work devoted to PCFs in literature assume the use of fused silica glass, silicate glass is here considered for fiber fabrication and modeling [76]. Silicate glass presents a higher attenuation with respect to fused silica. However, its Kerr nonlinearity index is one to two order of magnitude higher. Furthermore, also the linear refractive index of silicate glass is higher. The contribution of these two features additionally enhances the nonlinear effects in silicate PCFs. For these reasons much shorter lengths, even several centimeters of the fiber, are enough to observe nonlinear phenomena [77].

The nonlinear fiber here presented has been fabricated at the Faculty of Physics of the Warsaw University in Poland, by the group of Prof. Ryszard Buczynski, using a typical two steps process. First, glass capillaries have been stacked in an appropriate structure arrangement into the preform, which is drowned down to a subpreform. Then, after inserting the obtained subpreform into an external glass tube, it has been finally scaled down to a fiber. The geometry of the fabricated PCF consists of two rings of air-holes with a high filling factor arranged in a regular triangular lattice, as shown in Fig. 2.26. Two pairs of similar size air-holes, which are placed opposite each other with respect to the center of the fiber, are enlarged and form a core with a strong elliptical shape. The elongation of the core introduces asymmetry into the structure, causing a high birefringence in the fiber. In the fabricated PCF the air-holes are in a region of diameter equal to 16.9 μm, while the diameter of the whole fiber is 117 μm. The elliptical core dimension along the two main axes is equal to 2 μm and 8 μm, respectively. Since the structure is simultaneously anisotropic and cobweb-type, the fiber is birefringent, as well as nonlinear. In order to evaluate these PCF properties, the full vector modal solver based

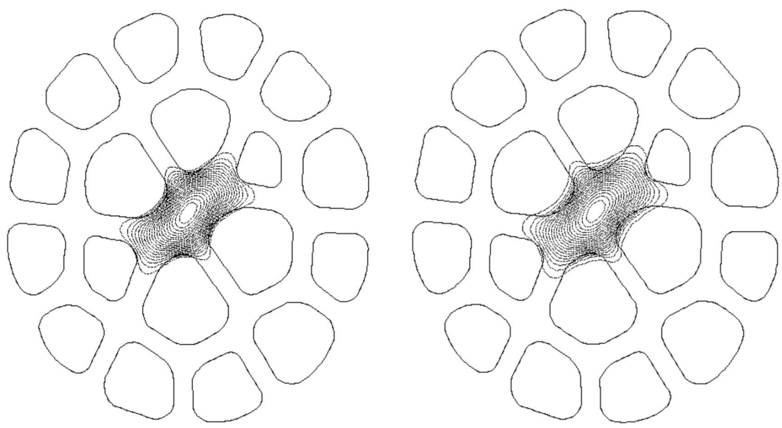

(a) (b)

Figure **2.27**: Representations of the magnetic field of the guided mode at (a) 800 *nm* and (b) 1500 *nm*.

on the FEM has been used to calculate the guided mode effective index and the magnetic field distribution. The fundamental component of the guided mode magnetic field at 800 *nm* and at 1550 *nm* is reported, respectively in Fig. 2.27a and b. The shape of the magnetic field fundamental component highlights the high birefringence of the considered PCF.

Starting from the electric and the magnetic field distributions for the fundamental mode and applying the Poynting vector definition, the normalized intensity $i(x, y)$ has been evaluated. This has been used to calculate the effective area A_{eff}, as described in Appendix A. The A_{eff} values has been evaluated for both the polarizations, with slightly different results at the two considered wavelengths. In fact, $A_{effx} = 7.7\ \mu m^2$ and $A_{effy} = 7.52\ \mu m^2$ at 800 *nm*, while $A_{effx} = 8.8\ \mu m^2$ and $A_{effy} = 8.44\ \mu m^2$ at 1500 *nm*.

In an optical fiber with high birefringence, like the silicate PCF here studied, the effective index of the guided mode is different for the two orthogonal polarizations. This difference is not constant as the wavelength changes. In particular, as reported in Fig. 2.28a, the effective index difference increases with λ in the range between 400 *nm* and 2000 *nm*. By calculating the effective index of the guided mode for different wavelengths and by applying the Sellmeier equation, the dispersion parameter D has been obtained through a

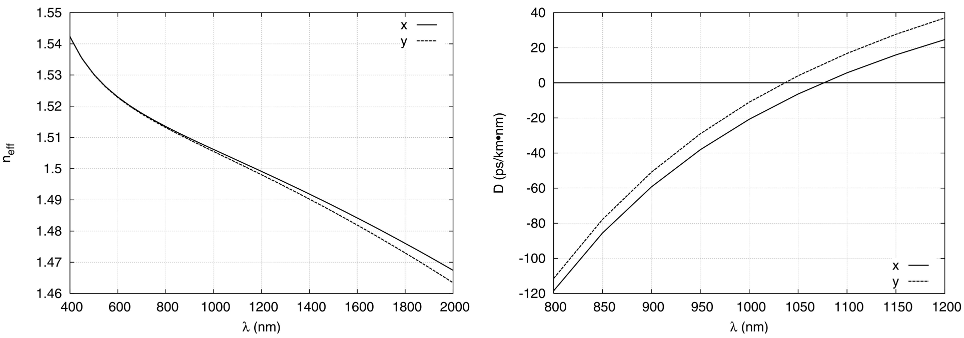

(a) (b)

Figure **2.28**: (a) Effective index versus the wavelength and (b) dispersion curves for the two orthogonal polarizations.

finite difference formula according to the expression of Eq. (A.4) of Appendix A. As a consequence, a dispersion curve for each polarization has been calculated and reported in Fig. 2.28b. Starting from the two dispersion curves, it is possible to calculate the zero-dispersion wavelength for the two orthogonal polarizations, which is, respectively, $\lambda_{0x} = 1075.28\ nm$ and $\lambda_{0y} = 1035.65\ nm$. Moreover, the dispersion slope at 1550 nm has been evaluated, being $slope_x = 0.0010251\ ps/nm^2 \cdot km$ for the x polarization, and $slope_y = 0.0011633\ ps/nm^2 \cdot km$ for the y one.

As well as the effective index difference, the birefringence B evaluated according to the expression of Eq. (A.5) of Appendix A increases with λ, reaching a maximum value of about $4 \cdot 10^{-3}$ at 2000 nm, as shown in Fig. 2.29a. On the contrary, L_B, whose expression is reported in Eq. (A.6) of Appendix A, decreases when the wavelength increases, as reported in Fig. 2.29b.

The numerical analysis of the PCF properties has been exploited to understand the experimental results of the preliminar measurements on the pulse spectral broadening made at the Faculty of Physics of Warsaw University during a Short Term Scientific Mission within the COST scientific programme on Physics of linear, nonlinear and active photonic crystals from August 22, 2005 to September 3, 2005. A Ti:sapphire laser has been employed to investigate the efficiency of self-phase modulation in the silicate highly nonlinear PCF. The light pulses at 800 nm produced by the Ti:sapphire laser, which have a

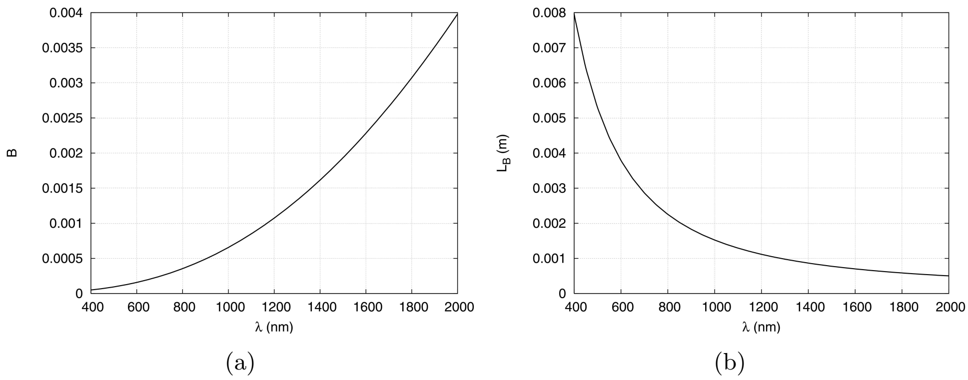

Figure **2.29**: (a) Birefringence B versus the wavelength λ and (b) behavior of L_B versus the wavelength λ for the silicate PCF.

duration of 50 fs and an average power of 150 mW, have been expanded with a telescope and then focused on the entrance face of the fiber sample, placed on a three-dimensional translation stage. Radiation coming out of the fiber has been focused on the entrance slit of a spectrometer. The spectra of the 50 fs Ti:sapphire laser pulses at the input and at the output of the PCF with a length of 39 cm are shown in Fig. 2.30a and b. The solid curves in these figures show the spectra of the pulses coming into the fiber for two different wavelengths, 790 nm and 820 nm, respectively. The dotted curves represent the spectra of the pulses at the output of the nonlinear PCF. Notice that the spectra of output radiation broaden. The pulse wavelength position respect to the zero-dispersion wavelength is one of the determining factors in order to obtain the spectral broadening. It is important to underline that, according to the previous numerical analisys of the nonlinear PCF dispersion properties, the experimental results reported in Fig. 2.30a and b have been obtained with a pulse wavelength in the PCF normal dispersion regime, as shown in Fig. 2.28b. As a consequence, the self-phase modulation dominates, as well as the Raman scattering, causing a broadening towards the long wavelength side. In these preliminar experiments the distance between the pumping wavelength and the zero-dispersion wavelength is higher than 200 nm. In order to obtain better results, that is an output spectrum smoother and larger, the pulse wavelength will be moved closer to the zero-dispersion one, so that other nonlinear effects will participate to the spectral broadening.

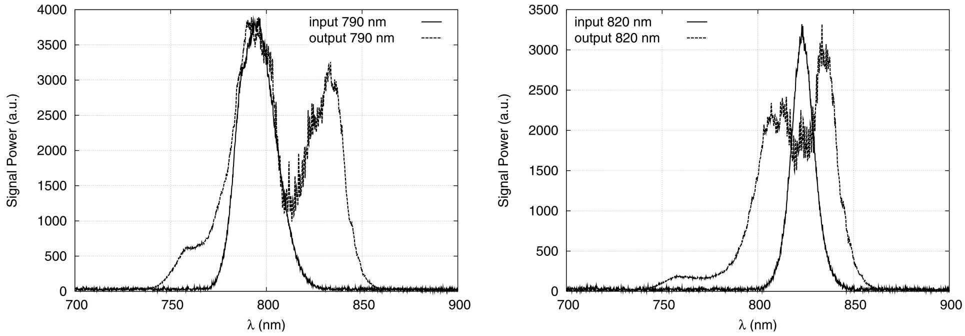

(a) (b)

Figure **2.30**: Spectra of the 50 fs Ti:sapphire laser pulses at the input and at the output of the PCF with a length of 39 cm for two different wavelength: 790 nm (a) and (b)820 nm.

2.5 Air-silica hollow-core Bragg fibers

While all the previous results regard the guiding properties of PCFs with a silica core, which guide light for TIR, here hollow-core fibers which exploit the PBG effect for light guiding are analyzed. In particular, the guiding properties of realistic air-silica hollow-core Bragg fibers have been investigated.

As previously described, in recent years, the advent of photonic crystal fibers [78] has provided a new way to obtain light guiding. In particular, optical fibers able to confine light within an air core, called hollow-core fibers, have been demonstrated [79]. These fibers are of particular promise for guiding high power light without damage or undesired nonlinear effects [80,81]. Moreover, their unusual characteristics are attractive for a range of devices used in medical applications, telecommunications, and sensing [82–85]. Air-guiding can be achieved by properly designing the cladding region in the fiber cross-section. In photonic crystal fibers the light confinement in the hollow-core has been obtained by exploiting the presence of a periodic lattice of air-holes in the cladding [79]. An alternative form of air-guiding can be provided also by hollow-core Bragg fibers.
Bragg fibers, firstly theoretically proposed in 1978 [31], have been recently fabricated with a hollow-core by combining solid-base materials of widely different refractive indices [86]. In these fibers, called OmniGuide fibers, light is

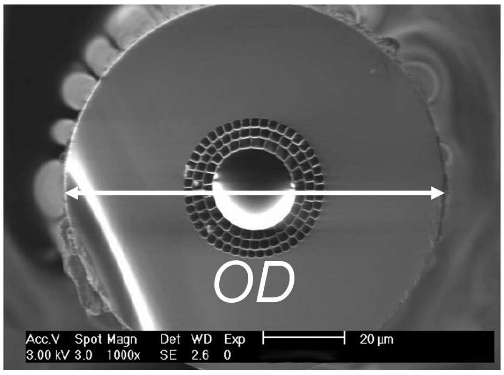

(a)

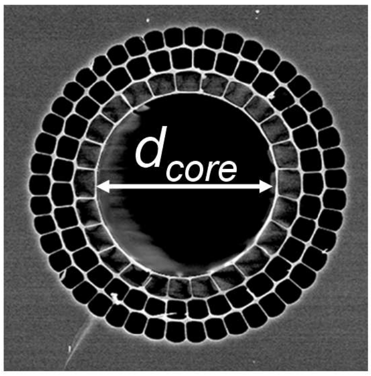

(b)

Figure **2.31**: Scanning electron microscope picture of the OD90 hollow-core Bragg fiber (a) cross-section and (b) cladding region.

guided by concentric multi-layer dielectric mirrors, which have the property of omnidirectional reflection [87]. The properties of OmniGuide fibers have been deeply investigated, showing, for example, the possibility of dispersion-tailoring [88]. Moreover, a throughout analysis of the TE and TM modes has been developed for these Bragg fibers, also considering a low refractive index difference [89].

This kind of hollow-core Bragg fibers provides interesting characteristics, but their fabrication is still an active research field, being quite complex. Different methods have been proposed in literature to manufacture both solid- and hollow-core Bragg fibers with alternating material layers in the cladding, using silica or polymers. By exploiting the modified chemical vapour deposition method, a silica Bragg fiber operating at 1060 nm with optical losses for the first time lower than 10 dB/km has been fabricated [90]. With the same technique, a Bragg fiber with a 34 μm diameter pure silica core, surrounded by a cladding composed by three layers of germania-doped silica and two layers of pure silica, exhibiting a modal area of about 500 μm^2 at a wavelength of 1550 nm, has been realized [91]. Also polymer material combinations have proved to be well suited for the Bragg fiber fabrication [92]. In fact, all-polymer hollow-core multilayer Bragg fibers, based on PMMA/PS and PVDF/PC material combinations, have been fabricated [92]. Recently, a bi-component solid-core polymer-based Bragg fiber consisting of approximately

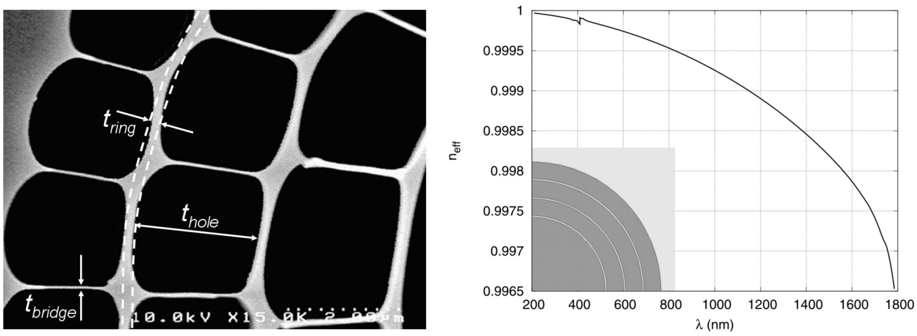

(a) (b)

Figure **2.32**: (a) Scanning electron microscope picture of the OD90 hollow-core Bragg fiber bridge region. (b) Fundamental mode dispersion curve of the OD90 hollow-core Bragg fiber without bridges. Inset: cross-section of the analyzed structure.

60 coaxial rings has been directly produced, for the first time, via melt extrusion, which offers a means of continuous high-volume low-cost manufacturing of this kind of fibers [93]. Other solid-core all-polymer Bragg fibers for light guiding in the visible range, with a large PMMA core surrounded by a 50 layer PMMA/PS Bragg reflector, have been realized starting from a preform made using a co-rolling technique [94]. As a consequence of these recent experimental advances in the fabrication process, hollow-core all-polymer Bragg fibers with periodic multilayers of PVDF/PC have been theoretically investigated to obtain optimal reflector designs in the whole terahertz region [95].

Due to the finite number of cladding layers, the guided modes in the Bragg fibers are affected by leakage. In order to reduce this leakage loss, that is to enhance the reflections from the cladding layers, the hollow-core Bragg fibers proposed in literature usually show cladding structures with a large index contrast between the alternating layers [86]. The leakage reduction can be more efficient if the low index material is air. By exploiting the photonic crystal fiber fabrication technology, silica/air hollow-core Bragg fibers with a cladding characterized by thin silica rings, surrounded by air and connected by nanoscale silica bridges, have been recently fabricated [28]. In order to realize this kind of fibers, silica has been used as the high refractive index material, and the stack-and-draw approach has been employed. In particular, an outer

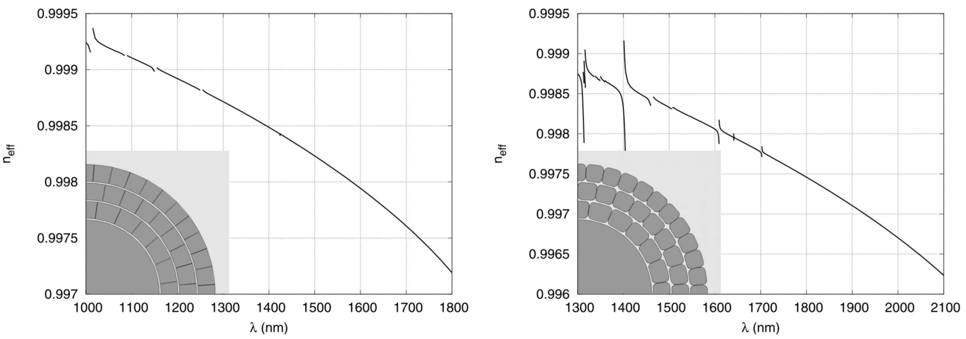

(a) (b)

Figure **2.33**: Fundamental mode dispersion curve of the OD90 hollow-core Bragg fiber (a) with squared off air-holes and (c) with rounded air-holes. Inset: cross-section of the analyzed structures.

silica tube has been filled with three tubes of decreasing sizes, by keeping fixed the distance between them. Within the annular gap, thin capillaries have been introduced and evenly distributed. The stack of tubes and capillaries has been then drawn to a preform cane, which has been subsequently pulled to fibers of different outer diameters. According to the experimental measurements [28, 29], these air-silica hollow-core Bragg fibers present transmission spectra with sharp variations and high loss peaks.

In literature the guiding properties of air-silica hollow-core Bragg fibers have been studied with different methods. For example, the asymptotic approach [96], which just takes into account an ideal and simplified fiber cross-section, that is without the silica bridges, has been applied [28, 29]. Unfortunately, this approach can only predict smooth confinement loss spectra, with values about two orders of magnitude lower than the ones experimentally measured [28, 29]. Recently, an idealized hollow-core Bragg fiber has been studied with both the transfer matrix approach and the FEM, showing the possibility to reduce the confinement loss by exploiting the second bandgap [97]. On the contrary, Uranus et al. [98] have considered a realistic model of the fiber cross-section, in order to calculate, at the fixed wavelength of 1060 nm, the attenuation of one of the hollow-core Bragg fibers described in [28], obtaining a better agreement with the measurement results with respect to the asymptotic approach.

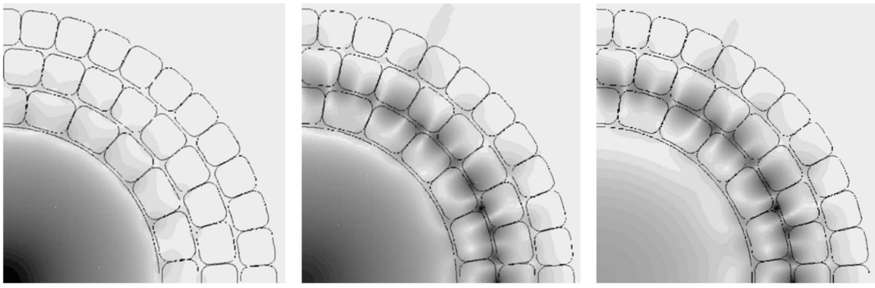

(a) (b) (c)

Figure **2.34**: Modulus of the magnetic field of the fundamental mode of the Bragg fiber OD90 with bridge width of 45 nm at three different wavelengths: (a) 1650 nm, (b) 1702 nm and (c) 1703 nm.

Here the full-vector modal solver based on FEM [99] has been used to analyze the spectral behaviour of several realistic hollow-core Bragg fibers, in order to understand the effect of the finite thickness of the silica bridges. The FEM allows to accurately discretize any kind of fiber cross-section, following any details of the geometrical shapes without approximations, and thus to consider the real structure of the fiber under investigation. In particular, hollow-core Bragg fibers with different values of the cross-section geometric parameters have been considered, in order to show their influence on the dispersion and confinement loss properties, as well as on the spatial distribution of the fundamental and higher-order guided modes. Simulation results have shown that the peaks experimentally observed in the Bragg fiber transmission spectra are strictly related to the bridge presence and to their width. In fact, numerous surface modes [32] are mainly localized in these thin silica supports, or in correspondence of the junctions between the bridges and the rings. The FEM has been also applied to identify which geometric parameter stronger influences the hollow-core Bragg fiber transmission window. Results have shown that an increase of the layer number is effective in order to reduce the hollow-core fiber confinement loss, while a proper layer design is able to enlarge the transmission window. Finally, it has been demonstrated that Bragg fibers can be employed in fiber sensor devices, in particular a bio-sensor application [100] has been investigated.

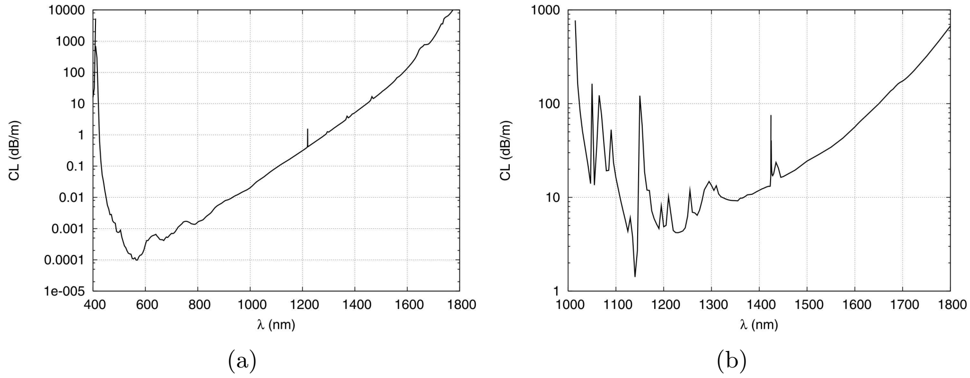

Figure **2.35**: CL obtained for the OD90 hollow-core Bragg fiber (a) without bridges and (b) with squared off air-holes and bridges 45 nm wide.

2.5.1 Guiding properties

Several samples of hollow-core Bragg fibers with different Outer Diameter (OD) have been presented in [28, 29]. In particular, the Bragg fiber with outer diameter of 90 μm, called OD90, is shown Fig. 2.31a and b. This fiber is characterized by three concentric cylindrical silica rings, surrounding the hollow-core with diameter d_{core}, with a thickness t_{ring}, separated by air layers, whose width is t_{hole}, and connected by nano-scale silica bridges t_{bridge} wide. In the present analysis the geometric parameter values already considered in [98] for the OD90 Bragg fiber, that is $d_{core} = 20$ μm, $t_{ring} = 0.2$ μm, $t_{hole} = 2.3$ μm and $t_{bridge} = 45$ nm, have been taken into account.

Firstly, the OD90 fiber has been modelled as in the asymptotic approach, that is by neglecting the silica bridge presence in the fiber cladding, shown in detail in Fig. 2.32a. The behaviour of the fundamental mode effective index n_{eff} as a function of the wavelength has been evaluated and it is reported in Fig. 2.32b. Notice that, as expected for air-guiding, n_{eff} values are always lower than 1, that is the refractive index of air. The effective index decreases as the wavelength becomes higher, and only a small discontinuity has been found in the wide range between 200 nm and 1800 nm. Then, silica nano-supports between adjacent rings, with thickness of 45 nm, have been added in the fiber cross-section, in order to obtain a more realistic Bragg fiber model [98]. When considering squared off air-holes in the fiber cladding, as shown in the inset of Fig. 2.33a, more discontinuities, the largest one around 1015 nm, can be identified in the dispersion curve, reported in the same figure. Finally, silica regions, called "islands", have been added at the interconnections between the rings and the bridges, thus obtaining rounded air-holes and, as a consequence, a fiber transverse section geometry very similar to the fabricated one, as demonstrated by the inset of Fig. 2.33b. This further geometry change significantly affects the n_{eff} behaviour, since the dispersion curve reported in Fig. 2.33b is no more regular, due to the numerous discontinuities, in particular at the shorter wavelengths. By analyzing the magnetic field modulus, for example, just before the last discontinuity, it is possible to recognize the transition of the guided mode, shown at 1650 nm on the left of Fig. 2.34, into a surface mode, reported at 1703 nm on the right of the same figure. So, each split in the dispersion curve represents an anti-crossing point between the guided mode and a surface one. Surface modes, which are located in the silica regions of the cladding surrounding the hollow-core, have been already widely studied in air-guiding photonic crystal fibers, since they considerably influence the fiber performances, being responsible of loss peaks in their transmission spectrum [32, 101]. Their presence has been demonstrated also by calculating the confinement loss CL, strongly related to the cross-section geometry. CL values have been evaluated in dB/m according to the expression of Eq. (A.11) of Appendix A.

Fig. 2.35a reports the CL spectrum for the ideal Bragg fiber previously described. Notice that it presents a U-shape, already observed in other kind of hollow-core PCFs [99], and it is very similar to the one obtained with the asymptotic approach [28, 29]. This transmission window is very wide, the CL being lower than 1 dB/m from 420 nm to 1285 nm, with a minimum of about $1{\cdot}10^{-4}$ dB/m at 575 nm. Unfortunately, the silica bridges negatively affect the Bragg fiber loss properties, causing the presence of surface modes, highly confined in the small silica regions at the interconnections between bridges and rings. In fact, by considering the curve reported in Fig. 2.35b obtained for the fiber with squared off air-holes, the CL values significantly increase, the minimum value being higher by more than four orders of magnitude and shifted to longer wavelengths with respect to the previous case. The same effect has been obtained for the Bragg fiber with rounded air-holes, since the minimum CL, about 16 dB/m, moves to 1650 nm as shown in Fig. 2.36a. Moreover, sharp peaks around 1565 nm, 1610 nm, 1640 nm and 1700 nm, due to the presence of surface modes, interrupt the regularity of the transmission

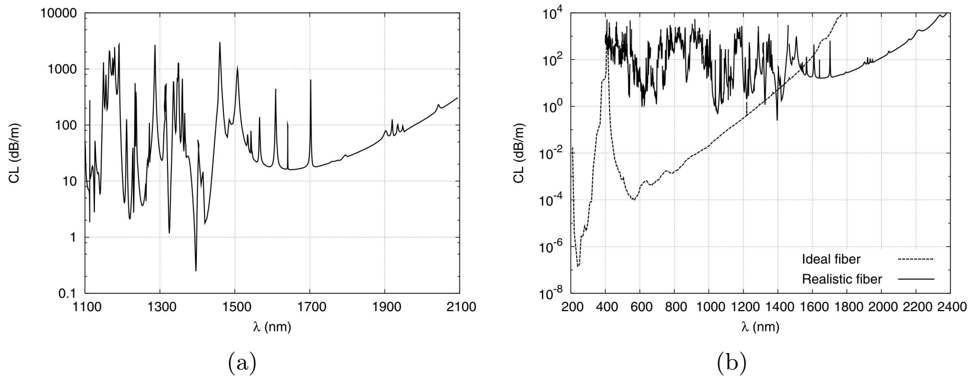

Figure **2.36**: CL obtained for the OD90 hollow-core Bragg fiber with rounded air-holes and bridges 45 nm wide. (b) Wideband comparison between the CL spectra of the three Bragg fibers considered.

window, as found also in the experimental measurements [28, 29]. Simulation results thus demonstrate that the silica nano-supports and, in particular, the "islands" at their interconnections, which are larger for rounded air-holes, are one of the main causes of the surface mode appearance.

Notice that as reported in Fig. 2.36b, the ideal Bragg fiber presents a second transmission window in the wavelength range between 200 nm and 400 nm, with a minimum of about $1.5 \cdot 10^{-7}$ dB/m at 240 nm, in agreement with the theoretical [29,97] and experimental results [29] previously presented. Differently from this behaviour, the CL curve of the realistic fiber is more polluted with sharp peaks in the lower part of the spectrum, that is for the wavelengths lower than 1400 nm. In fact, not only the loss values increase significantly, but a lot of high peaks appear in the CL spectrum, so that the only useful window is the one for the wavelengths longer than 1500 nm. In the shorter wavelength range only narrow and highly uneven transmission windows can be identified around 620, 1050, 1225 and 1420 nm. The light guiding is not effective for the wavelengths lower than 400 nm, being the dispersion curve interrupted by discontinuities and the fundamental mode no more confined in the fiber hollow-core.

Surface modes negatively influence also the loss behaviour of the higher order modes. In particular, in the present analysis the higher order modes TE_{01}, TM_{01}, $HE_{21,a}$ and $HE_{21,b}$ have been considered. As expected, the

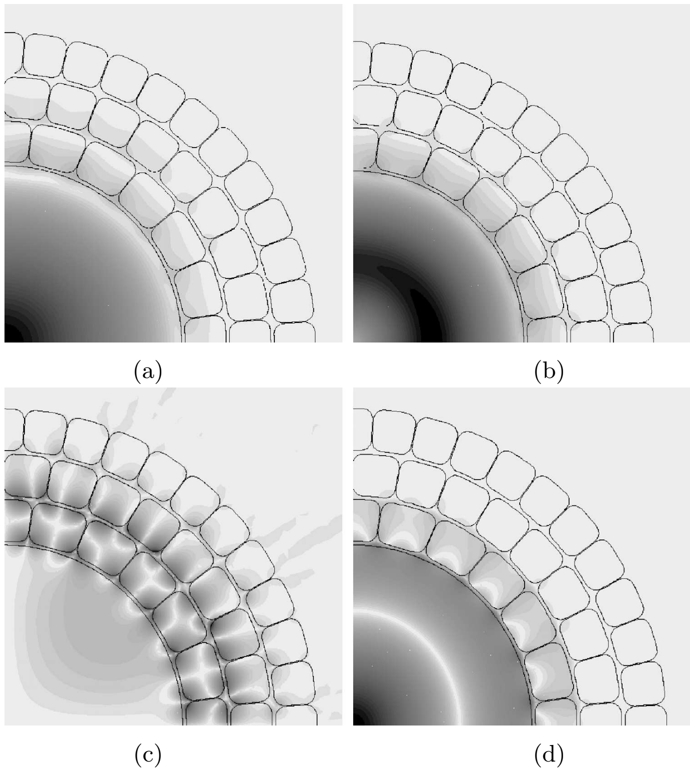

Figure **2.37**: Magnetic field modulus of (a) the HE_{11} mode and (b) the TE_{01} mode, $|H_z|$ of the (c) TM_{01} mode and (d) TE_{01} mode of the realistic OD90 fiber at 1875 nm.

magnetic field modulus of the fundamental mode, shown in Fig. 2.37(a) at the wavelength of 1875 nm, is characterized by a gaussian-like shape and it is well confined in the fiber hollow-core. On the contrary, a donut-shape distribution of the magnetic field modulus on the hollow-core Bragg fiber cross-section has been obtained for all the higher order modes, as reported, for example, in Fig. 2.37(b) for the TE_{01} mode. In order to identify each higher-order mode, the modulus of the longitudinal component of the magnetic field, that is $|H_z|$, has been taken into account. This is significantly different for the TM_{01} mode, being almost null as shown in Fig. 2.37(c), and for the TE_{01} one, reported in Fig. 2.37(d). The CL curves for the fundamental mode and for

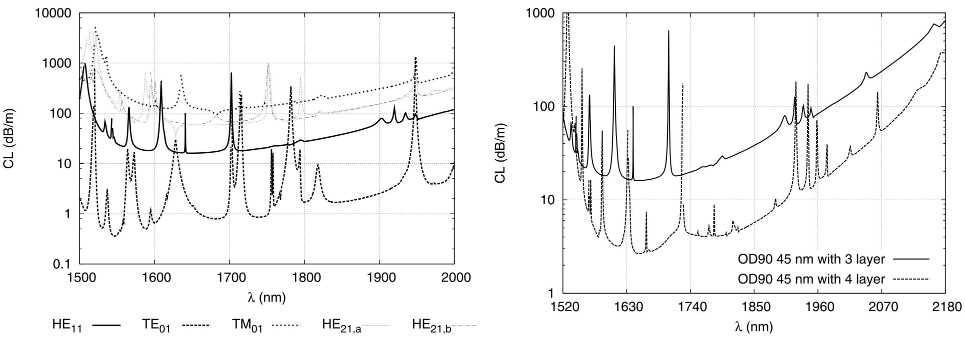

(a) (b)

Figure **2.38**: (a) CL spectra of the fundamental mode HE_{11} and of the first higher order modes, that is TE_{01}, TM_{01}, $HE_{21,a}$ and $HE_{21,b}$. (b) Fundamental mode CL curves of the OD90 hollow-core Bragg fiber with 3 and 4 layers in the cladding and bridges 45 nm wide.

the TE_{01} and for the TM_{01} ones are reported in Fig. 2.38a in the wavelength range between 1500 nm and 2000 nm. It is important to underline that the silica bridges in the hollow-core Bragg fiber cladding causes the presence of numerous surface modes, which break the transmission window regularity also for the TE_{01} and the TM_{01} mode. Moreover, as already demonstrated with the asymptotic approach for the ideal Bragg fiber structure [29, 97], the CL values for the TE_{01} mode are about one order of magnitude lower than those for the fundamental one, which in turn have the same relation with the TM_{01} loss in all the considered wavelength range. In fact, by fixing, for example, the wavelength to 1660 nm, the loss value is about 1 dB/m, 16 dB/m and 123 dB/m for the TE_{01} mode, the fundamental and the TM_{01} one, respectively. Notice that the same behaviour has been obtained also for the two higher-order modes $HE_{21,a}$ and $HE_{21,b}$. The CL values for these two modes are similar in the considered wavelength range, and are intermediate between the ones for the fundamental mode and the TM_{01} mode, being the loss minimum about 60 dB/m around 1650 nm.

In conclusion, the TE_{01} is the higher-order mode which has the most significant influence on the single-mode regime of hollow-core Bragg fibers, due to its low confinement loss values.

2.5.2 Cross-section geometric parameter influence

As demonstrated by all the CL curves reported so far, as well as by the measured spectra, the hollow-core Bragg fibers are affected by quite high loss values. Consequently, it is important to investigate possible design improvements of the fiber cross-section, in order to obtain better loss properties for this kind of air-guiding fibers, otherwise interesting for different applications [80–82, 84]. Since it has been previously shown that the PCF leakage loss can be reduced by increasing the air-hole ring number in the cladding [45, 102], an OD90 fiber with bridges 45 nm wide and 4 pair of silica and air layers in the cladding has been considered. Its CL spectrum is compared with the one of the 3-layer OD90 Bragg fiber in Fig. 2.38b. As expected, by increasing the layer number, a significant decrease of more than one order of magnitude of the CL values has been obtained, the minimum being about 3 dB/m around 1615 nm for the 4-layer fiber. However, there is still a strong peak presence in the CL spectrum, and the transmission window is almost unchanged.

As it has been experimentally demonstrated [28, 29], the CL spectrum of hollow-core Bragg fibers changes with the geometric parameters in the fiber cross-section. In particular, the transmission window shifts towards the higher wavelengths when Bragg fibers with a larger OD are considered [28, 29]. In order to identify which geometric parameter causes the transmission window shift experimentally observed for fibers with a similar structure scaled to a different outer diameter, the loss properties of intermediate fibers between the OD90 fiber and the OD105 one, with an OD of 105 μm, have been analyzed. Starting from the fabricated OD90 fiber, several Bragg fibers have been considered by performing a step-by-step analysis, that is by changing only one geometric parameter when passing from a fiber cross-section to another one. At first, the CL values for the OD90 hollow-core Bragg fibers have been calculated for two different values of the silica bridge width, that is 45 nm, already discussed in the previous section, and 70 nm. The CL spectra for the two fibers are reported in Fig. 2.39a and b, respectively, in the wavelength range between 1500 nm and 2900 nm. Notice that both the hollow-core Bragg fibers are characterized by a wide U-shaped transmission window. When the bridges become wider, that is 70 nm, the transmission window, as well as the sharp peaks due to the surface modes, shift to longer wavelengths and the CL values significantly increase. In fact, the loss minimum, which is about 16 dB/m around 1650 nm for the 45 nm wide bridge hollow-core Bragg fiber, becomes 52 dB/m around 1765 nm for the fiber with wider bridges. Two intermediate structures between OD90 fiber and OD105 one have been studied. In the first one, named Bragg Fiber 1, the t_{ring} value of the OD90 fiber with bridges 70 nm wide has been increased from 0.2 μm to 0.25 μm, which is the ring width in the fabricated OD105 fiber. The CL spectrum of this fiber, reported in Fig. 2.39c, has the same behaviour of the one previously described, except for slightly lower loss values, the minimum being about 50 dB/m around 1860 nm, and the 3-dB bandwidth being 85 nm, between 1805 nm and 1890 nm. A second intermediate fiber, called Bragg Fiber 2, has been obtained from the previous one by increasing only t_{hole} from 2.3 μm to 3 μm. Fig. 2.39d shows its transmission window, which is shifted to longer wavelengths, with a 3-dB bandwidth enlarged to 125 nm and fewer peaks associated to the surface modes. As a further step, the core diameter has been increased from 20 μm to 23 μm, in order to obtain the OD105 hollow-core Bragg fiber structure. It is important to underline that the effect of the core diameter increase is practically only a reduction of the loss values, as shown in Fig. 2.39e. In fact, a minimum CL value of about 35 dB/m at 2190 nm has been calculated. Finally, when the bridge width decreases to 40 nm, which is the minimum value technologically feasible, the transmission window, reported in Fig. 2.39f, shifts to smaller wavelengths, with a significant decrease of the CL, reaching a minimum of 10 dB/m at 2040 nm. All these results demonstrate that the Bragg fibers CL values decrease when the silica bridge width is reduced, or the hollow-core is enlarged, with the possible drawback of the higher-order mode number increase. Differently, the changes of the silica ring thickness, or of the air-hole layer width are effective in adjusting the transmission window position.

2.5.3 Confinement loss property improvement

In order to obtain a further improvement of the fiber loss properties, that is lower CL values and larger bandwidth, a new cladding structure, which involves a combination of pairs of air and silica layers with different thickness, has been proposed, in order to obtain an improvement of the hollow-core Bragg fiber guiding properties. In particular, the FEM, already successfully used to study this kind of fibers [97,98,103], has been applied to deeply investigate how the fundamental mode CL spectrum changes when modifying the periodicity of the cladding layers. Ideal fibers, without the silica bridges, have been initially considered, in order to draw general conclusions regarding the light guiding through the Bragg reflection. Then, these considerations have been

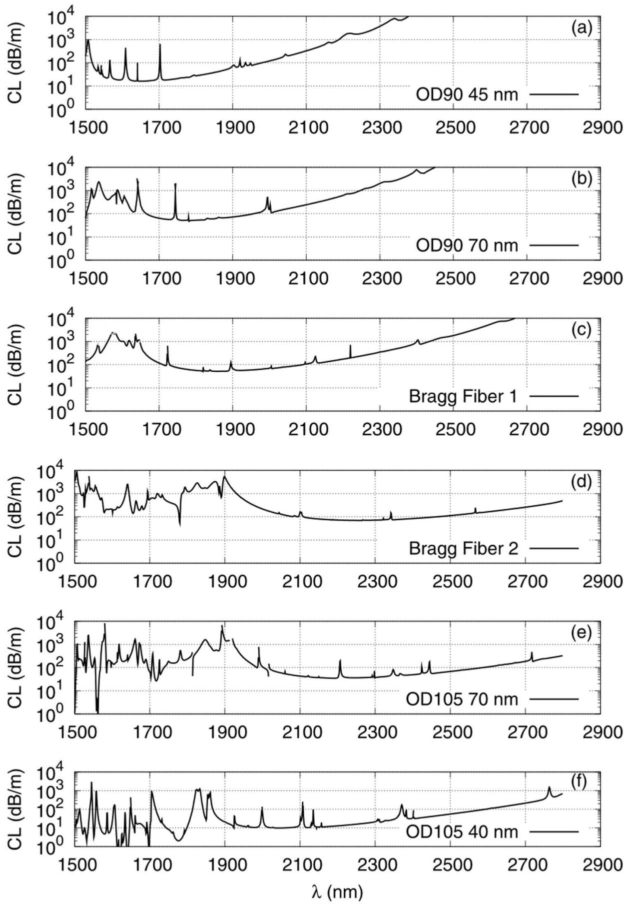

Figure **2.39**: CL spectra of different Bragg fibers, obtained starting from the OD90 fiber and changing only one geometric parameter every time, towards the OD105 fiber.

applied, as a significant example, to the realistic structure of the 4-layer OD90 fiber, with the aim to obtain a more regular transmission window comprised in the C band.

In order to obtain improvements of the Bragg fiber guiding properties, three different pairs of air and silica layers with thickness t_{hole} and t_{ring}, respectively, have been taken into account, which are indicated as S (i.e. Small),

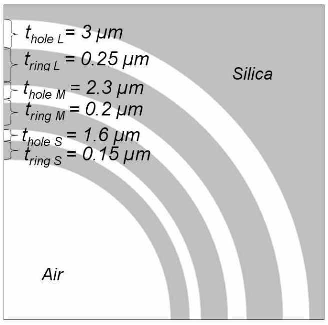

(a)

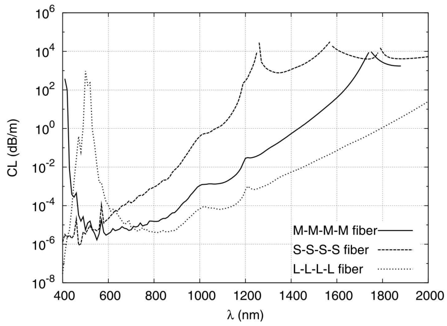

(b)

Figure **2.40**: (a) Cross-section schematic of the layer pairs proposed in the hollow-core Bragg fiber cladding. (b) Fundamental mode CL spectra of fibers with 4 identical rings.

M (i.e. Medium) and L (i.e. Large) and described in Fig. 2.40a. Notice that M represents the pair of air and silica layers in the cladding of the OD90 fiber, while wider silica ring and air-hole have been considered in the L pair, according to the characteristics of the OD105 fiber cladding. The S layer pair has been finally obtained by reducing the t_{hole} and t_{ring} values of the OD90 fiber in the same way.

Firstly, ideal fibers, that is without silica bridges, characterized by 4 pairs of air and silica layers have been considered. Fig. 2.40b reports the CL spectra of the hollow-core Bragg fibers with 4 identical layer pairs, that is with the conventional periodicity in the cladding. It is important to underline that, regardless of the pair type, a CL minimum of about $1{\cdot}10^{-6}$ dB/m has been obtained. The values of t_{ring} and t_{hole} influence only the minimum position, being around 400 nm, 550 nm and 820 nm for the S-S-S-S, M-M-M-M and L-L-L-L fiber, respectively. Notice that the transmission window minimum shifts towards the longer wavelengths by increasing the layer thickness. Moreover, looking at the CL spectra, it is possible to notice that a larger transmission window can be obtained for fibers with pairs of wider layers in the cladding.

With the aim to combine the spectral properties obtained with each pair of layers, hollow-core Bragg fibers with two different arrangements of layer pairs have been analyzed. In particular, the fundamental mode CL values for fibers

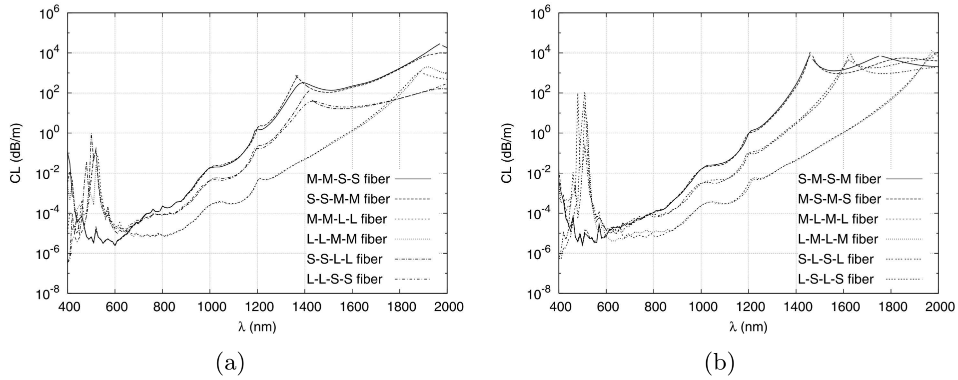

Figure **2.41**: Fundamental mode CL spectra of the ideal Bragg fibers with (a) a double periodicity and (b) alternating layer pairs in the cladding.

characterized by a double periodicity, or by alternating couples of air and silica layers have been reported in Fig. 2.41a and b for all the combinations of S, M and L layer pairs. Notice that the CL curves for the fibers with the same two couples of layer combination in the cladding are almost equal, independently from their position. In fact, for example, both the M-M-S-S and S-S-M-M fibers present the same loss spectral behaviour and a CL minimum of about $2.5{\cdot}10^{-6}$ dB/m around 600 nm. The CL minimum for the fibers with S and M pairs is the lower one, that is $2 \cdot 10^{-6}$ dB/m at 600 nm, while the higher is that of the fibers characterized by M and L pairs, being $7 \cdot 10^{-6}$ dB/m at 810 nm. The latter hollow-core Bragg fibers are characterized by the largest bandwidth, being the CL values lower than $1 \cdot 10^{-4}$ dB/m in a 400 nm wavelength range, between 570 nm and 970 nm. Looking at Fig. 2.41b, it is possible to notice that also for the fibers with alternating layer pairs in the cladding the order is not influential on the CL behaviour. Moreover, by comparing the results reported in Fig. 2.41a and b, it is possible to conclude that the CL curves for the hollow-core Bragg fibers with the same 4 layer pairs, independently from their position in the cladding, are almost identical. For example, consider the M-M-S-S and S-S-M-M fibers of Fig. 2.41a, as well as the M-S-M-S and S-M-S-M fibers of Fig. 2.41b.

Since simulation results have shown that the bridge presence strongly influences the CL spectra [103], silica nanosupports 45 nm wide, as in OD90 fiber, have been introduced in the cross-section of the fibers with layer pairs

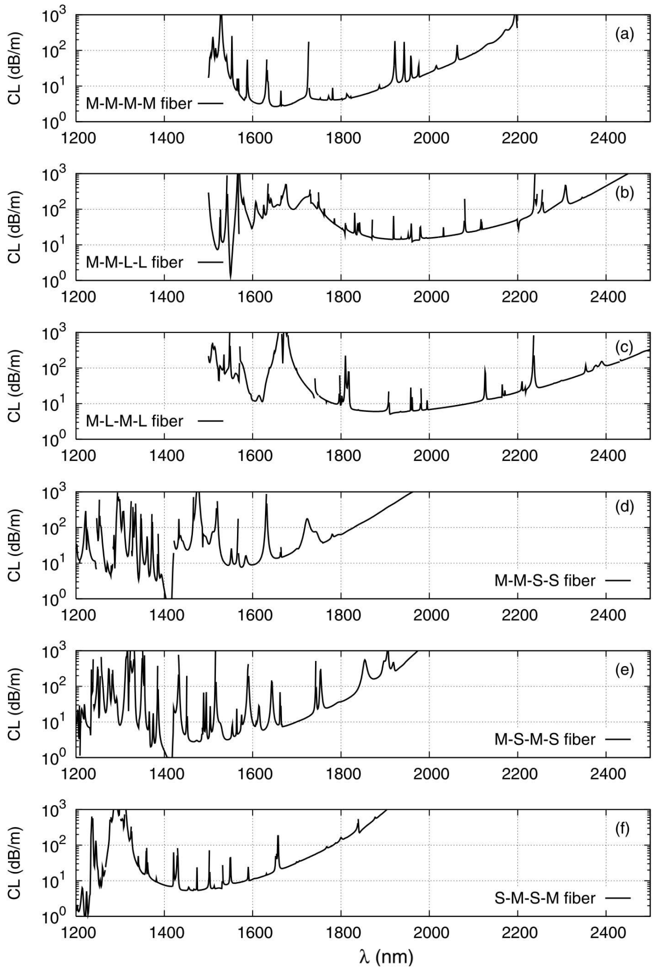

Figure **2.42**: Fundamental mode CL spectra of the realistic hollow-core Bragg fibers with different combinations of air and silica layers in the cladding.

S, M and L in the cladding, thus obtaining realistic hollow-core Bragg fibers. The transmission window of the M-M-M-M fiber, that is the 4-layer OD90 one, presents a minimum of 3 dB/m around 1615 nm and a quite wide 3-dB bandwidth, but interrupted by high peaks, as shown in Fig. 2.42a.

By enlarging the air and silica layers in the outer part of the cladding, thus obtaining the M-M-L-L fiber, the bandwidth is significantly enlarged, in agreement with the results of the previous analysis on the ideal fibers, but the CL minimum slightly increases, being about 12 dB/m around 1960 nm, and the U-shape transmission windows is centred more far away from the C band. The sharp peak presence can be reduced by considering the M-L-M-L fiber, which provides also a decrease of the loss minimum value to about 5 dB/m around 1910 nm, and a further enlargement of the transmission window, the loss being lower than 8 dB/m from 1820 nm to 2040 nm, as shown in Fig. 2.42c. It is important to underline that, differently from the ideal structure case, the order of the layer pairs in the Bragg fiber cladding influences the loss behaviour, as shown by the different CL properties of the last two realistic fibers considered, which have the same layer pairs. In order to design hollow-core Bragg fibers useful for the telecommunications, the L layer pair in the cladding has been substituted by the S one. In fact, as reported in Fig. 2.42d and e, the reduction of the silica ring and air-hole width provides the shift of the transmission window to the shorter wavelengths. As a drawback, the 3-dB bandwidth decreases and a lot of sharp peaks, more numerous than in the OD90 fiber spectrum, appear. Changing the order of the alternating layer pairs to reproduce the proportion rule of the M-L-M-L case, the S-M-S-M fiber has been considered, which presents better guiding properties, as shown in Fig. 2.42f. In fact, the transmission window is significantly less fragmented and almost completely comprised in the C band, being the loss minimum, that is about 5 dB/m, around 1450 nm and the CL values lower than 10 dB/m until 1580 nm, with the exception of few narrow peaks.

2.5.4 Hollow-core Bragg fiber as a bio-sensor

The unique characteristics of hollow-core Bragg fibers make them ideal for sensor applications [82–84]. In particular, in the present work, the possibility to exploit the OD90 fiber as a biological sensor useful to detect the hybridization in DNA molecules has been investigated.

DNA molecules are double-stranded, that is made by two single-stranded chain well-positioned, so that their bases, or nucleotides, can interact with each other [104]. A DNA chain is made by connecting the bases via chemical bounds, forming an oligonucleotide. A single DNA strand can be isolated with different techniques, forming a very reactive and unstable molecule. In fact, a single oligonucleotide easily joins a complementary strand of a DNA molecule, to reform a double-stranded structure. This phenomenon of re-

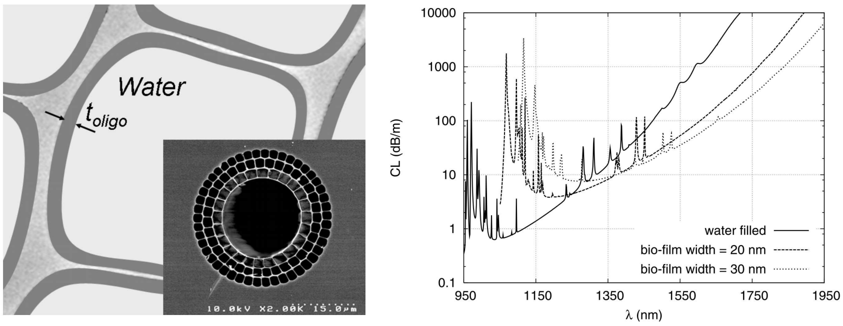

(a) (b)

Figure **2.43**: (a) Schematic representation of the holes in the hollow-core Bragg fiber with a inner coating t_{oligo} wide. (b) Fundamental mode CL curves of the water-filled OD90 hollow-core Bragg fiber without and with a 20 nm and 30 nm wide bio-film.

annealing, called hybridization, is exactly the process that should be detected through the fiber sensor [104]. Firstly, it is necessary to immobilize single oligonucleotides, contained in an aqueous solution, on the inner surfaces of the fiber holes with a long complicated procedure [104]. This single-stranded DNA molecule layer modifies the geometric and dielectric characteristics of the Bragg fiber core and cladding, thus altering its guiding properties. Then, an aqueous solution, containing single-stranded DNA molecules of an unknown kind, which can be complementary or not to the one previously immobilized, is flushed into the fiber. Only in the first case the hybridization takes place and a double-stranded molecule is formed. The consequent growth of the layer coating the inner walls of the fiber holes changes again the fiber cross-section characteristics, as well as the guided mode ones. As a consequence, by comparing the transmission properties of the fiber before and after the last step, it is possible to conclude if the hybridization happened, that is if the two strands of DNA considered were complementary or not.

In order to investigate the feasibility of this kind of bio-sensor in a Bragg fiber, the CL spectrum of the OD90 fiber fully filled of water, with refractive index 1.33, has been calculated and compared with the one obtained by adding the first and the eventual second layer on the inner surface of the core and the cladding holes. In particular, the immobilization of a single oligonucleotide

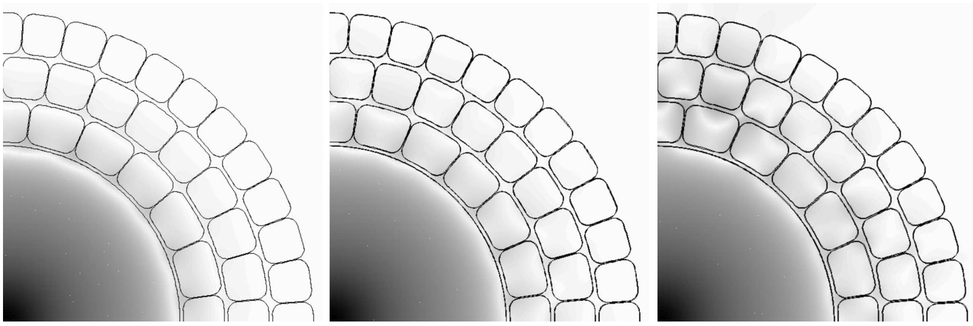

(a) (b) (c)

Figure **2.44**: Magnetic field modulus of the fundamental mode at 1137 nm of the water-filled OD90 hollow-core Bragg fiber (a) without and with a bio-film layer (b) 20 nm and (c) 30 nm wide.

and the next potential hybridization have been emulated by introducing a biological coating with a thickness t_{oligo} of 20 nm and 30 nm, respectively, whose refractive index is 1.55 [100]. This coating has been added on the inner walls of the water-filled fiber holes, as reported in Fig. 2.43a. The fundamental mode CL spectra obtained for the OD90 Bragg fiber in the three different conditions are reported in Fig. 2.43b in the wavelength range between 950 nm and 1950 nm. With respect to the OD90 fiber with air-holes, deeply described in the previous sections, the water-filled fiber is characterized by a CL minimum one order of magnitude lower, that is about 1 dB/m, and shifted to the shorter wavelengths of about 600 nm, being around 1035 nm. Notice that, by adding the bio-film, the U-shaped transmission window moves towards the longer wavelengths and the loss values significantly increase. This effect is stronger when considering the thicker layer, the CL minimum being about 7 dB/m around 1270 nm and about 4 dB/m around 1190 nm when t_{oligo} is 30 nm and 20 nm, respectively. On the contray, the 3 dB-bandwidth is almost unchanged, being approximately 200 nm, between 1130 nm and 1330 nm, and about 165 nm, from 1207 nm to 1372 nm, for the fiber with 20 nm and 30 nm wide coating, respectively. In order to better understand how the bio-film changes the properties of the fundamental mode, it is useful to consider the magnetic field modulus at a fixed wavelength, that is, for example, 1137 nm, as reported in Fig. 2.44. In agreement with the increase of the confinement loss values, the field becomes less confined in the Bragg fiber core, when the bio-film is added on the hole inner surface.

In summary, a 100 nm shift and a 3 dB increase of the CL minimun has been obtained before and after the potential hybridization. As a consequence, by exploiting the CL spectrum shift, as well as the loss increase, the OD90 Bragg fiber can be successfully used as the DNA bio-sensor.

Chapter 3

Erbium-doped fiber amplifiers

This Chapter summarizes the results obtained by exploiting the bending losses of an erbium-doped fiber with a depressed-cladding to realize amplifiers, as well as lasers in S band.

During the first year of the PhD course an accurate experimental study of S band Erbium-Doped Fiber Amplifier (EDFA) performances has been carried out by changing the signal input power, the pump power, the fiber bending diameter and the fiber length. The proposed EDFA is based on a depressed-cladding Erbium-Doped Fiber (EDF). By winding the fiber with a proper bending diameter, the ASE in the C band can be filtered, thus allowing gain in S band. Moreover, by inserting the proposed EDFA in a Double-Pass (DP) configuration, a significant gain improvement has been obtained. Finally, by combining in a new parallel scheme a S band amplifier and a C band one, both with a DP configuration and realized with the same depressed-cladding EDF, bent with two different diameter values, an EDFA for S+C band has been demonstrated. By adding a L band module, a triple band all-silica erbium-doped fiber-based optical amplifier has been developed. The amplifier encompasses a parallel configuration with three different paths for S, C and L band signals.

By moving from the amplification process to the laser one, a tunable narrow-linewidth triple-wavelength Erbium-Doped Fiber Ring Laser (EDFRL) has been experimentally demonstrated, where the bending losses of the depressed-cladding fiber have been exploited to tune the laser wavelength in S, C and L band. This tuning method has been also exploited to move the wavelength of a single frequency EDFRL in S band and in C band.

Finally, a tunable single frequency S band depressed-cladding EDFRL where the doped fiber has been used as the active medium, as well as the tunable filter has been proposed and experimentally demonstrated.

3.1 S band amplification

Due to the recent explosive growth of the telecommunication requirements, new optical transmission bands with amplifiers are desired to satisfy the ever increasing capacity demand of Wavelength-Division Multiplexed (WDM) systems. Nowadays, optical amplification outside C and L band is required, so alternative optical fiber amplifiers have been investigated.

S band, (1450 $nm \div 1530$ nm), is particularly attractive, being characterized by low loss in silica optical fibers. Several methods have been proposed to provide gain in S band, such as flouride-based Tm-doped fiber amplifiers [105–108] and Raman amplifier [109]. Other hybrid amplification techniques have been proposed by combining Raman and Tm-doped fiber amplifiers stages [110], or by exploiting silica-based P/Al-codoped EDFs [111]. Also EDFs have been used, by suppressing the Amplified Spontaneous Emission (ASE) in the C band. This suppression has been previously realized with complicated multistage filters [112] or by exploiting the fundamental mode cut-off near 1530 nm of a depressed-cladding EDF [113–116]. Recently, it has been demonstrated that the ASE can be suppressed also by exploiting the

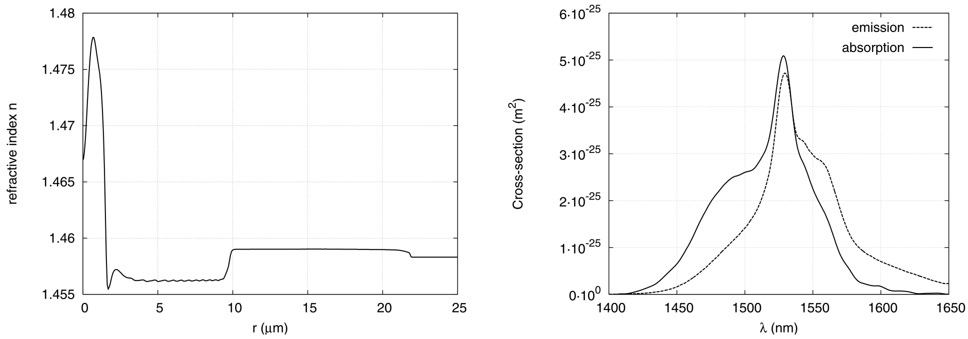

(a) (b)

Figure **3.1**: (a) Refractive index profile and (b) emission and absorption cross-section of the depressed-cladding erbium-doped fiber.

bending losses of this kind of fiber [117–119].

3.1.1 Depressed-cladding EDF

The depressed-cladding silica-based EDF here considered has the refractive index profile reported in Fig. 3.1a, characterized by $\Delta n^+ = n_1 - n_3 = 0.0162$ and $\Delta n^- = n_2 - n_3 =$ -0.0028, where n_1, n_2, n_3 are, respectively, the core, inner cladding and outer cladding refractive indices. The ratio between the radius of the inner cladding and that of the core is 6.3, the dopant region radius is 1.46 μm and the erbium ion concentration is 7.40 10^{24} $ions/m^3$. In Fig. 3.1b the emission and absorption cross-section of the depressed-cladding EDF are shown in the wavelength range between 1400 nm and 1650 nm.

It is well known that the bending losses of a depressed-cladding fiber change with the bending diameter [120]. In particular, losses can reach very high values when the diameter is small. It has been also demonstrated that this loss spectrum shifts towards shorter wavelengths for tighter bends and that this effect can be exploited to inhibit the ASE in the C band to the advantage of that in S band [117]. In Fig. 3.2a the attenuation spectra for different values of the bending diameter d are reported. These measurements have been obtained with a 1 m-long depressed-cladding EDF. Looking at the behaviour of the straight fiber, it is possible to notice the erbium absorption peak, about 12 dB/m at 1530 nm, and a very high attenuation for the wave-

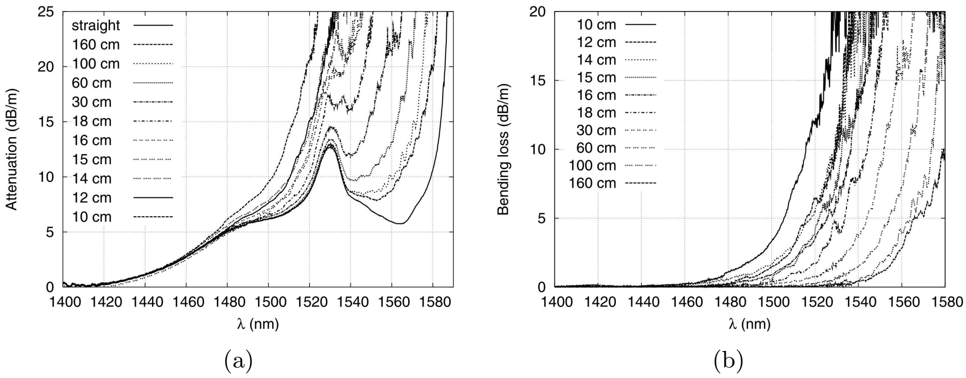

Figure **3.2**: (a) Attenuation and (b) bending loss spectra measured for different bending diameters.

lengths $\lambda > 1570$ nm. This attenuation is related to the fundamental mode cut-off of the depressed-cladding fiber, which is slightly lower than 1590 nm. In spite of this cut-off, the straight fiber would be useless to suppress the C band ASE, thus frustrating amplification in the S band. However, as shown in the figure, by reducing the bending diameter d, the strong transition in the attenuation curve moves towards shorter wavelengths. Bending losses, whose spectral variation for different values of the bending diameter d is reported in Fig. 3.2b, can thus be exploited as a tunable filter which suppresses the ASE in the C band and allows S band amplification. In fact, looking at the curve obtained with the largest bend diameter, that is 160 cm, it is possible to notice that the bending losses increase significantly for the wavelengths $\lambda > 1520$ nm. Moreover, by reducing d, the net transition moves towards shorter wavelengths. For example, for a bend diameter of 10 cm, the bending losses increase for the wavelengths $\lambda > 1460$ nm.

3.2 Single Pass S band EDFA

The measurement setup adopted for the Single Pass (SP) S band amplifier, consists of a classical 980 nm-forward pumping scheme, with a pump power of about 120 mW. A fiber coupler, which exhibits 0.07 dB and 0.15 dB loss at 980 nm and 1480 nm, respectively, has been used to multiplex the 980 nm

pump and the S band signal. A tunable laser has been used as the signal source. An isolator with an insertion loss of 0.49 dB has been inserted, in order to avoid a laser behaviour in absence of the signal. An attenuator has been used to modify the signal input power in the range -25 $dBm \div 0$ dBm. The optical connections of the 15 m-long depressed-cladding EDF have been made by regular fusion splices with taper, providing 0.35 dB loss, and the optical characterization has been carried out by using an Optical Spectrum Analyzer (OSA).

In order to confirm the bending loss influence on the EDFA performances, the ASE spectra have been measured using the amplifier setup previously described by turning off the signal power. As shown in Fig. 3.3a, the ASE spectrum changes in agreement with the bending loss behaviour. In particular, the ASE spectrum shape obtained with d in the range 14 $cm \div 16$ cm seems to be the most suitable in order to obtain S band signal amplification. In fact, with larger bending diameters, such as 60 cm, the ASE spectrum is too much narrow and centered around 1530 nm. On the other hand, with the smallest d values, that is 10 and 12 cm, there is a strong attenuation due to the bending loss also in the S band wavelength range.

In view of the previous considerations, the amplifier performances have been measured by changing the bending diameter in a slightly wider range, between 10 cm and 18 cm, for different signal input power values. Results for -15 dBm are reported in Fig. 3.3b in the wavelength range 1470 $nm \div$ 1530 nm. The best gain spectrum in Fig. 3.3a has been obtained with a bending diameter of 15 cm, being the maximum gain G around 22 dB at 1504 nm and the 3-dB bandwidth almost 26 nm. Notice that G abruptly decreases after 1525 nm, since the attenuation becomes too high. When d is smaller, the strong gain decrease moves toward the shorter wavelengths, as well as the G maximum value, which is 20 dB at 1500 nm and 16.9 dB at 1490 nm for a bending diameter of 14 cm and 12 cm, respectively. It is interesting to underline that with $d = 10$ cm it is not possible to obtain significant gain in S band. Good gain performances have been demonstrated also for d equal to 16 cm, while $d = 18$ cm is not suitable to reach amplification in the desired wavelength range. Results for a signal input power of -10 dBm are reported in Fig. 3.4a. As for the lower signal input power value, the best gain performances have been measured with a bending diameter of 15 cm, since the peak gain is around 19.7 dB at 1502 nm and the 3-dB bandwidth is almost 24 nm. Similar considerations can be applied to the gain spectra

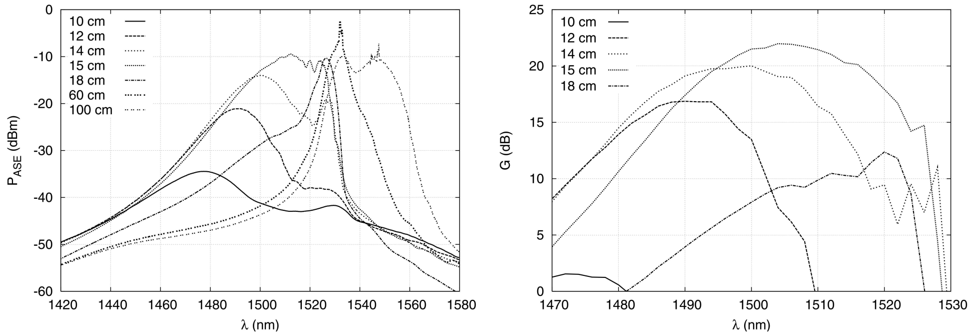

(a) (b)

Figure **3.3**: (a) ASE spectra measured for different bending diameters. (b) Gain spectra versus the bending diameter measured for the signal input power of -15 dBm.

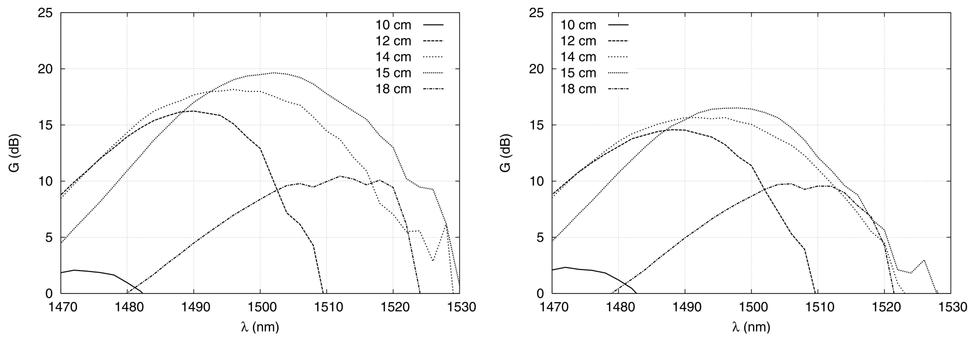

(a) (b)

Figure **3.4**: Gain spectra versus the bending diameter measured for the signal input power of (a) -10 dBm and (b) -5 dBm.

obtained with -5 dBm signal input power, shown in Fig. 3.4b. Notice that the influence of the bending diameter on the gain spectrum shape is lower in this case, being smaller the difference among the maximum gain values for $d = 14$, 15, 16 cm. For example, the highest G values are, respectively, 16.5 dB at 1498 nm and 15 dB at 1496 nm when d is equal to 15 cm and 16 cm.

The influence of the bending loss have been analyzed also by changing the signal input power in the range -25 $dBm \div 0$ dBm for a fixed bending diameter value. In Fig. 3.5a results are shown for $d = 15$ cm, which is the optimum bending diameter for the amplifier here considered. As the signal power increases, G values become lower, as well as the gain bandwidth, and the abrupt gain decrease moves towards the shorter wavelengths. The maximum G of 25.3 dB has been obtained at 1504 nm when the signal input power is -25 dBm. Moreover, the gain is almost constant, with a ripple lower than 1 dB, in a wavelength range of 14 nm, that is from 1501 nm to 1515 nm, while the 3-dB bandwidth is almost 30 nm. In correspondence of the peak gain, the noise figure is 6.4 dB, while the minimum value, 5.1 dB, has been reached at 1492 nm.

In order to demonstrate how the EDFA gain spectrum can be optimized and shifted in different wavelength ranges by exploiting the filtering effect of the bending losses on the ASE spectrum, G values obtained for a bending diameter of 100 cm have been also reported. Notice that the maximum gain G is around 20.7 dB at 1554 nm and the 3-dB bandwidth is almost 35 nm in the wavelength range 1528 $nm \div 1563$ nm. It is important to underline that flat gain spectra have been measured in the C band, due to the bending losses, which are still high for $\lambda > 1550$ nm even for this large d value. With the depressed-cladding fiber here considered a C band amplifier is not realizable in practice, since the necessary bending diameter is too large. However, by a proper design of the fiber refractive index profile, that is by a proper choice of the fundamental mode cut-off, it is possible to obtain good EDFA amplifiers also in this wavelength range for bending diameter values which are actually feasible for system applications.

3.3 Double Pass S band EDFA

In order to improve the gain performances of the S band EDFA, a Double Pass (DP) configuration has been considered. Fig. 3.6a reports the experimental setup of the realized S band DP EDFA, with a configuration proposed by Rosolem et al [118]. Notice that the WDM signal configuration has been obtained by coupling the Laser Diodes (LD) through a multiplexer (MUX), whose output is sent to port 1 of the first Optical Circulator (OC1). Port 2 is connected to a WDM optimized for S band, which is used to couple, according to a classical co-propagating scheme, a pump power of 120 mW at 980 nm into the same 15 m-long depressed-cladding EDF, bent with a diameter d which is

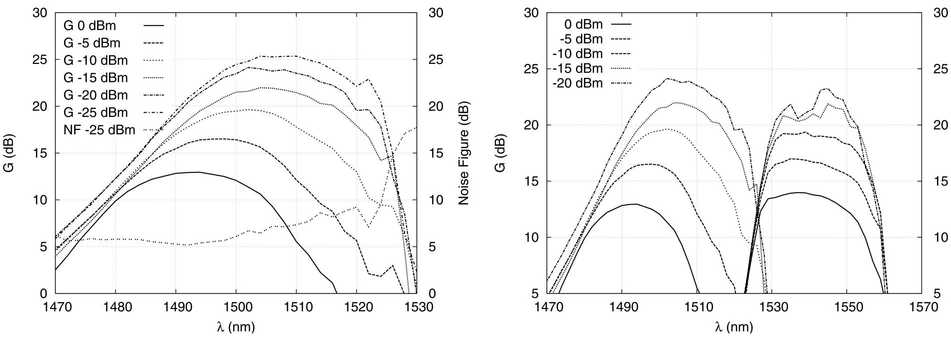

(a) (b)

Figure **3.5**: (a) Gain and noise figure spectra versus the signal input power measured for the bending diameter of 15 *cm*. (b) Comparison between gain spectra measured for the bending diameter of 15 *cm* and 100 *cm*.

optimized for S band region, as discussed in the previous Section. The active fiber 13 *cm* bent is spliced to a SMF with a loss of 0.35 *dB*. A second circulator OC2, whose port 1 is connected to port 3, is used at the EDF end to allow the double passage of the signals inside the amplifier. When the amplified signals come back to the EDFA input, they are routed to the OSA through port 3 of the OC1.

The gain spectra of the S band DP EDFA have been measured, by changing the wavelength of the tunable laser from 1470 *nm* to 1530 *nm* and the power between -25 and -5 *dBm*. As shown in Fig. 3.6b, a maximum gain of 36 *dB* has been obtained at 1512 *nm* for a signal power of -25 *dBm*. As the signal input power increases, the gain becomes lower in all the considered wavelength range, but the gain bandwidth improves. In fact, the 3-*dB* bandwidth becomes 22 *nm* for an input power of -20 *dBm* and it reaches a maximum value of 28 *nm* for the highest power, that is -5 *dBm*, while the peak gain is 32.1 *dB* at 1512 *nm* and 19.3 *dB* at 1496 *nm*, respectively. Notice that with the depressed-cladding doped fiber and the EDFA configuration here considered, a gain 4 *dB* higher than that reported in [118] has been obtained around 1500 *nm* with the same pump and signal power, that is 120 *mW* and -20 *dBm*, respectively.

In order to evaluate the S band EDFA improvements due to the DP configuration, the gain and the noise figure have been measured for the DP and

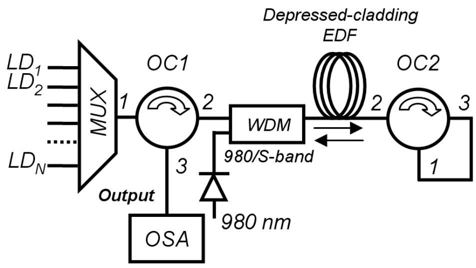

(a)

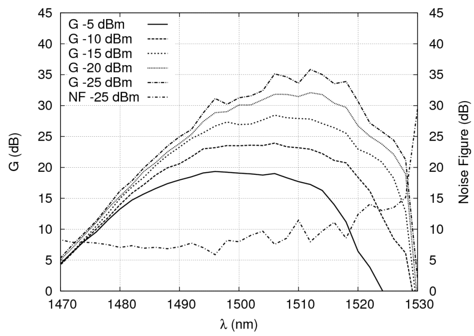

(b)

Figure **3.6**: (a) Scheme of the DP EDFA experimental setup. (b) Gain and noise figure spectra of the DP S band EDFA for different signal power values in the range between -25 and -5 dBm.

the SP amplifier with a signal input power of -25 dBm and -10 dBm. Results are reported in Fig. 3.7a. It is important to underline that the gain obtained with the DP configuration for a signal power of -25 dBm is at least 8 dB higher than that reached with the SP one in a wavelength range of 16 nm, between 1505 nm and 1521 nm. The maximum difference, that is around 11 dB, has been reached at 1512 nm and 1518 nm. For the highest power, that is -10 dBm, the gain measured with the DP configuration overcomes of 5 dB the gain obtained with the SP one in a wavelength range of 15 nm, between 1508 nm and 1523 nm. Notice that the drawback of this configuration is given by a slight increase of the noise figure, as shown in the figure, due to the counter-propagating ASE.

The gain spectra measured for the C band DP EDFA, obtained by bending the fiber with a diameter d equal to 100 cm for a pump power of 120 mW, are reported in Fig. 3.7b. For the C band EDFA a maximum gain of 41 dB has been obtained at 1550 nm when the signal input power is -25 dBm. Moreover, the 3-dB bandwidth is almost 12 nm between 1543 and 1555 nm. In correspondence of the peak gain, the noise figure is 7.2 dB. A flat and wide gain spectrum has been measured for the highest signal input power. In fact, as the signal power increases, the peak gain becomes lower and the gain bandwidth improves. For a signal input power of -20 dBm and -5 dBm, the

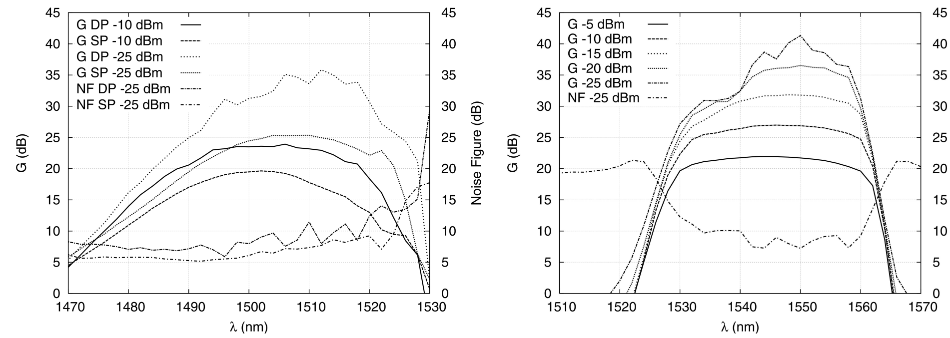

(a) (b)

Figure **3.7**: (a) Gain and noise figure spectra of the S band EDFA with SP and DP configuration. (b) Gain and noise figure spectra of the DP C band EDFA for different signal powers in the range between -25 and -5 *dBm*.

peak gain is 36.5 *dB* and 22 *dB*, respectively, and the 3-*dB* bandwidth changes from 18 *nm* to 32 *nm*.

Finally, it has been analyzed how the power of a single channel at the DP EDFA output is influenced by the presence of a high power saturating signal, which simulates the behavior of a WDM configuration with more than three low power signals. Fig. 3.8a reports results obtained for an input power of -25 *dBm* for four values of the saturating channel wavelength, λ_s, that is 1490, 1500, 1510 and 1520 *nm*, when its power is fixed to -6 *dBm*. Notice that the presence of the saturating signal causes a decrease of the output power in all the considered wavelength range, which is maximum when $\lambda_s = 1510$ *nm*, that is near the gain peak wavelength, and minimum for the lower λ_s value, that is 1490 *nm*. For example, at 1512 *nm*, the single channel output power decrease is 3 *dB* and 10 *dB* when the saturating channel is launched, respectively, at 1490 *nm* and 1510 *nm*.

3.4 S+C band DP EDFA in parallel configuration

Besides a wide band, a flat gain is a mandatory requirement for fiber amplifiers employed in WDM systems. Several techniques have been adopted, such as Raman amplification [121], which is attractive to expand the gain over all the

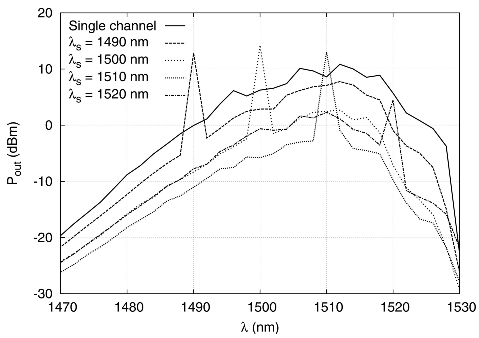

(a)

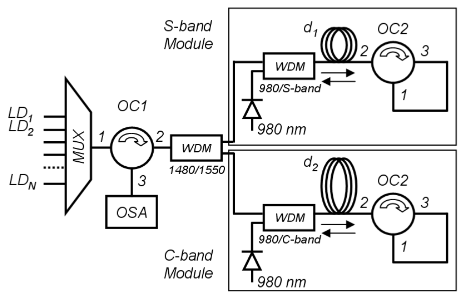

(b)

Figure **3.8**: (a) Output power measured with a single tunable channel with power -25 dBm in presence of a high power signal at λ_s. (b) Experimental setup for the S+C band EDFA.

transmission bandwidth, or amplifiers based on fibers realized with alternative host glasses, such as tellurite [122] and flouride [123]. Even different EDFA topologies, which employ a coupled structure [124] or a parallel configuration [116, 125] have been proposed. This solution however presents a limitation given by the dead-zone between the adiacent bands where no signals can be transmitted, due to the non-ideal wavelength multiplexing behaviour.

While in the previous Section, the gain and noise performances of the S and C band DP amplifiers based on the same 15 m-long depressed-cladding EDF have been individually analyzed, here the design of a S+C band amplifier in parallel configuration has been studied. Fig. 3.8b reports the experimental setup of the realized S+C band parallel EDFA. In order to couple the input signals into the amplifier, a MUX has been used, whose output is sent to port 1 of the OC1. Port 2 is connected to a 1480/1550 WDM coupler to split the S and C band signals in the correspondent EDFA module. Both S and C band modules have been realized in a DP configuration with a 15 m-long depressed-cladding EDF bent with two different diameters, that is 15 cm and 100 cm, respectively. In each EDFA module a WDM coupler has been used to multiplex the input channels and a 980 nm pump, with a maximum power of 120 mW, according to a classical co-propagating scheme. In order to allow the double passage of the signals into the doped fiber, a second circulator, OC2 and OC3 for the S and C band module, respectively, has been placed at the

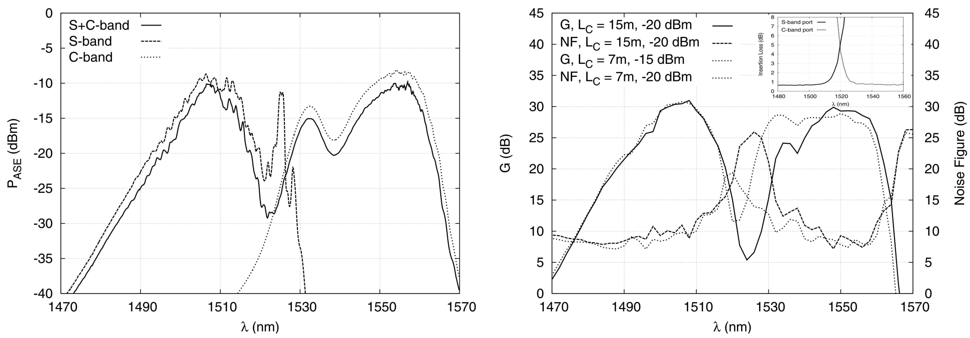

(a) (b)

Figure **3.9**: (a) ASE spectra of the DP S and C band amplifiers, measured with the experimental setup shown in Fig. 3.8b with 120 mW and 80 mW pump power at 980 nm, respectively, and ASE spectrum of the S+C band EDFA in parallel configuration, measured with the same pump power. (b) Gain and noise figure spectra of the S+C band EDFA with $L_C = 7$ m and $L_C = 15$ m for an input power of -20 dBm. Inset: insertion loss versus the wavelength of the 1480/1550 WDM coupler.

EDF end with port 1 connected to port 3. When the amplified signals come back from both the EDFA modules to the amplifier input, they are routed to the OSA through port 3 of OC1. It is important to underline that the setup shown in Fig.3.6a can be obtained by removing the 1480/1550 WDM coupler from the parallel amplifier scheme and by connecting the circulator OC1 directly to the S band module or to the C band one.

Fig. 3.9a reports the ASE spectra centered in S and C band of the DP amplifiers with the scheme reported in Fig. 3.6a, and the ASE spectrum of the S+C band EDFA, with the parallel configuration shown in Fig. 3.8b, measured by turning off the input signal. Notice that, in order to equalize the wide-band ASE spectrum and, as a consequence, the gain, the pump power in the C band module has been reduced to 80 mW, while the S band one has been kept constant to 120 mW. These pump power values correspond to the ones used in each of the two DP amplifiers to obtain the ASE spectrum shown in Fig. 3.9a.

Fig. 3.9b shows the spectra of the gain and the noise figure in the range 1470 $nm \div 1570$ nm for a signal input power of -20 dBm, measured by using

120 mW and 80 mW pump power in the S and C band module, respectively. The doped fiber lengths are L_S and L_C for the S band and the C band amplifier, respectively. With $L_S = L_C = 15$ m, a peak gain value of 31 dB and 30 dB and a noise figure of 8.8 dB and 7.1 dB have been obtained at 1508 nm and 1548 nm, respectively. Notice the presence of a dip in the gain spectrum around 1524 nm, which is due to the insertion loss of the 1480/1550 WDM coupler, reported in the inset of Fig. 3.9b. In fact, these losses are lower than 1 dB for the wavelengths shorter than 1512 nm in the S band port and longer than 1526 nm in the C band one, and they are almost 5 dB around 1520 nm for both the ports. However, it is important to underline that, despite of the WDM coupler bandgap loss, which is visible also in the ASE spectrum shown in Fig. 3.9b, a gain of almost 5 dB has been measured in a 92 nm wavelength range, between 1473 nm and 1565 nm. In order to optimize the gain profile and to reduce the gain dip, the EDFA performances have been investigated for different values of L_C. In particular, by choosing L_C equal to 7 m with the same L_S, a larger gain bandwidth and a significant dip reduction is obtained. In fact, the gain increases around 1530 nm and the dip minimum is almost 7 dB higher than that reached with $L_C = 15$ m for a signal power of -20 dBm. Moreover, with the shorter C band EDFA the noise figure value in correspondence of the dip wavelength decreases from 26 dB to 19 dB.

The performances of this optimized S+C band amplifier have been deeply analyzed. Results are shown in Fig. 3.10a in the range 1470 $nm \div 1570$ nm, by varying the signal input power between -25 and -10 dBm. A peak gain of 35.3 dB and 33 dB, and a noise figure of 6.9 dB and 8.7 dB have been obtained at 1508 nm and 1534 nm, respectively, when the input power is -25 dBm. Moreover, the maximum gain values become lower, that is 22 dB at 1502 nm and 20 dB at 1546 nm, as the signal power increases to -10 dBm. A gain of almost 10 dB has been measured in a 85-nm wavelength range, that is 1478 $nm \div 1563$ nm, for a signal input power of -25 dBm.

The amplifier performances have been then measured by simultaneously launching six signals in the doped fiber by changing the signal input wavelengths, thus obtaining different WDM configurations. In Fig. 3.10b the output power spectra for two different six-signal configurations which cover the entire S+C band, that is 1490, 1500, 1510, 1540, 1550, 1560 nm and 1510, 1520, 1530, 1540, 1550, 1560 nm, are reported for an input power of -25 dBm. As a comparison, the values previously obtained by modifying the wavelength of a single channel are also shown. Notice that the output power values of the

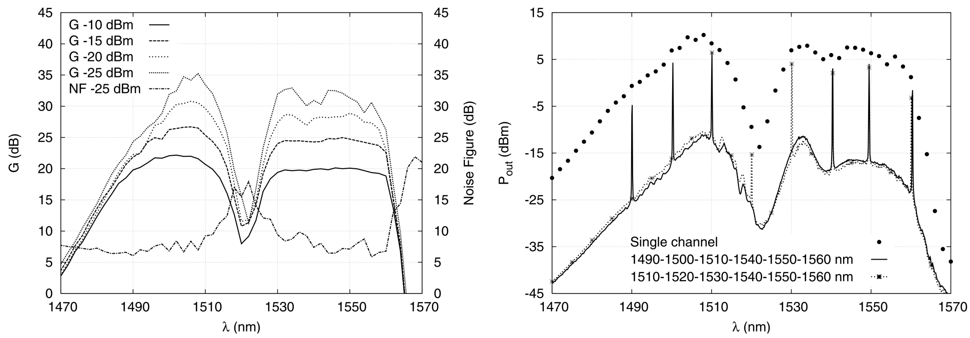

(a) (b)

Figure **3.10**: (a) Gain and noise figure spectra of the S+C band EDFA realized with $L_C = 7\ m$ for different signal power values in the range between -25 and -10 dBm. (b) Output power obtained with a single tunable channel and six signals at different wavelengths between 1490 and 1560 nm for an input power of -25 dBm.

two six-signal configurations are almost the same of those measured with a single channel. In fact, for the first six-signal configuration, the output power decrease is about 4 dB for the channel at 1490 nm and lower than 2.5 dB for the other channels. By considering the second six-signal configuration, the output power is lower than the single channel one of about 3.5 dB and of 5 dB for the channels in C band and for the channel at 1520 nm, respectively, while it is almost unchanged for the signal at 1510 nm.

Finally, it has been analyzed how the power of a single channel at the S+C band EDFA output is influenced by the presence of a high power saturating signal, which simulates the behavior of a WDM configuration with more than six power signals. Fig. 3.11a reports the results obtained for an input power of -25 dBm considering different saturating channel wavelength λ_s, with a fixed power of -6 dBm. As a comparison, the values previously measured with a single channel are also shown. As expected, the presence of the saturating signal causes a decrease of the output power with respect to the single channel case, in all the considered wavelength range. The difference is maximum when $\lambda_s = 1510\ nm$ and $\lambda_s = 1550\ nm$, that is near the peak gain wavelength for S and C band, respectively.

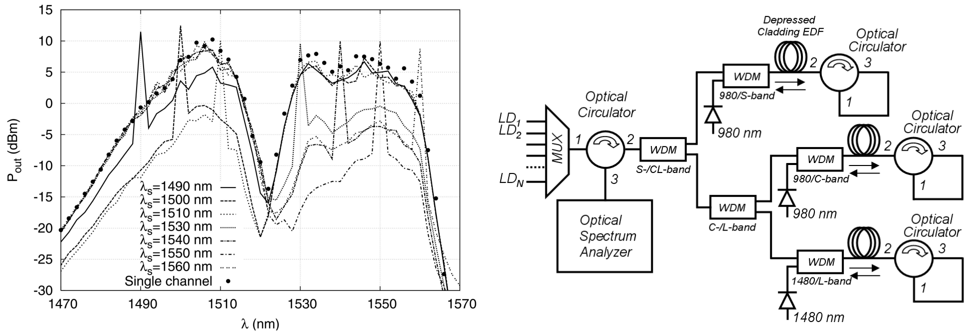

(a) (b)

Figure **3.11**: (a) Output power measured with a single tunable channel with power of -25 dBm in presence of a high power signal at λ_s. (b) Experimental setup of the proposed DP S+C+L band EDFA.

3.5 Triple band DP EDFA

In order to increase the transmission capacity of both dense and coarse WDM systems, broadband optical amplifiers are mandatory devices, provided they are capable to enlarge the traditional amplification band, the C one, which extends from 1530 nm to 1565 nm. Actually, many WDM optical links already use the L band, between 1565 nm and 1625 nm, thus considerably increasing the system capacity. In addition, triple band systems have been under investigation for years with the intent to consider also the S band, from 1460 nm to 1530 nm. Whereas amplification in L band has been achieved by exploiting the well established technology developed for EDFAs in C band, various and different solutions have been proposed for the S band. As previously reported, a way toward the usage of all-silica erbium-doped fibers for triple band amplification [116] has been opened up by the recent investigation on depressed-cladding doped fibers.

During the PhD course the experimental setup and the characterization of a triple band all-silica erbium-doped fiber-based optical amplifier, whose amplification in S band is obtained due to the losses introduced in C band by the fiber bending, has been developed. The amplifier encompasses a parallel configuration with three different paths for S, C and L band signals. Moreover, it implements a DP scheme, which allows the signals to pass twice through the

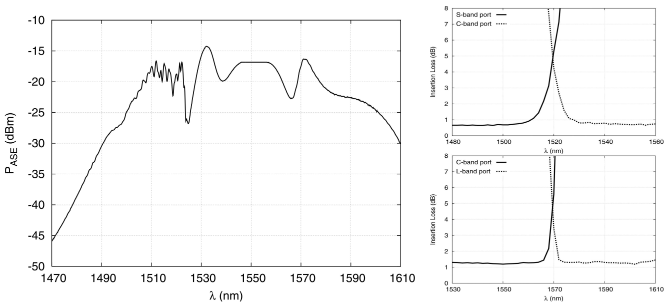

(a) (b)

Figure **3.12**: (a) ASE spectra of the proposed DP S+C+L band EDFA. (b) Insertion loss of the S/CL band and C/L band WDM couplers.

doped fiber, thus fully exploiting the injected pump power. The DP scheme improves the EDFA performances while using fewer components than a bidirectional pumping scheme, thus providing a cost effective solution, of primary importance, for example, in coarse WDM systems.

Fig. 3.11b reports the experimental setup of the realized S+C+L band parallel EDFA. In order to couple the input signals into the amplifier, a MUX has been used, whose output is sent to port 1 of a first optical circulator. Port 2 is connected to a band WDM coupler to separate the signals from S band to the C and L band, in order to provide distinct amplification paths. The S band module, as well as the C band and the L band ones, have been realized in a DP configuration. The DP technique, usually adopted in L band [126] to enhance the gain, and recently exploited also in S band [127], as previously reported, plays an important role in the development of practical EDFAs. In each EDFA module a WDM coupler has been used to multiplex the input channels and the pump, according to a classical co-propagating scheme. In order to allow the double passage of the signals into the doped fibers, for each module, a second circulator has been placed at the EDF end with port 1 connected to port 3. When the amplified signals come back from each EDFA modules to the amplifier input, they are routed to the OSA through port 3 of the first optical circulator. Two laser diodes at 980 nm with 120 mW and 100 mW power have been employed to pump the S band module and the C band one, respectively, while another laser, providing 100 mW of optical power at 1480 nm, has been used to pump the L band module. The L band EDFA has a 100 m-long EDF, while the C and the S band EDFA has 11 m- and 15 m-long EDF, respectively. The fiber considered inside the S band EDFA, is a depressed-cladding silica-based EDF 13 cm bent. It is important to underline that inside each module the EDF lengths and the pump powers have been chosen in order to equalize the gain spectrum.

By turning off the input signals, the ASE spectrum of the proposed DP S+C+L band EDFA has been measured and it is reported in Fig. 3.12a. An output power of almost -30 dBm has been obtained in a 120 nm wavelength range, between 1490 nm and 1610 nm. This can be exploited as a broad-band ASE source. Notice that the dips in the gain spectrum around 1526 nm and 1570 nm are due to the insertion loss of the S/CL band and C/L band WDM couplers, respectively, which are reported in Fig. 3.12b. In fact, for the first WDM these losses are lower than 1 dB for the wavelengths shorter than 1512 nm in the S band port, and longer than 1526 nm in the C band one, and they are almost 5 dB around 1520 nm for both the ports. Similar considerations can be applied to the C/L band WDM coupler.

By changing the signal input power from -30 dBm to -5 dBm, the performances of the proposed amplifier have been investigated for the central wavelength in S, C and L band, that is 1510 nm, 1550 nm and 1590 nm. The measured gain and noise figure as a function of the signal input power are reported in Fig. 3.13a. As expected, for each considered wavelength the G values become lower, as the signal power increases. The maximum gain and the minimum noise figure have been obtained for the input signal at 1550 nm and 1590 nm, respectively. In particular, when the signal input power is -30 dBm, a maximum G of 29.73 dB has been obtained at 1550 nm, while the minimum value of the noise figure, that is 6.4 dB, has been obtained at 1590 nm.

In order to better analyze the EDFA performances, the gain and the noise figure spectra of the S+C+L band DP amplifier have been measured for a single channel by changing its wavelength from 1470 nm to 1610 nm, and its power between -30 and -10 dBm. As shown in Fig. 3.13b, a gain of 29.4 dB, 30.7 dB, 30.9 dB and 30 dB and a noise figure of 9.6 dB, 7.5 dB, 6.5 dB and 7 dB have been obtained at 1514 nm, 1532 nm, 1556 nm and 1572 nm, respectively, when the signal input power is -30 dBm. Notice that the maximum gain values become lower, that is 17.7 dB at 1502 nm, 17.4 dB at 1552 nm and 19 dB at 1574 nm, as the signal power increases to -10 dBm. It is important to underline that a 140 nm gain bandwidth in the range 1470

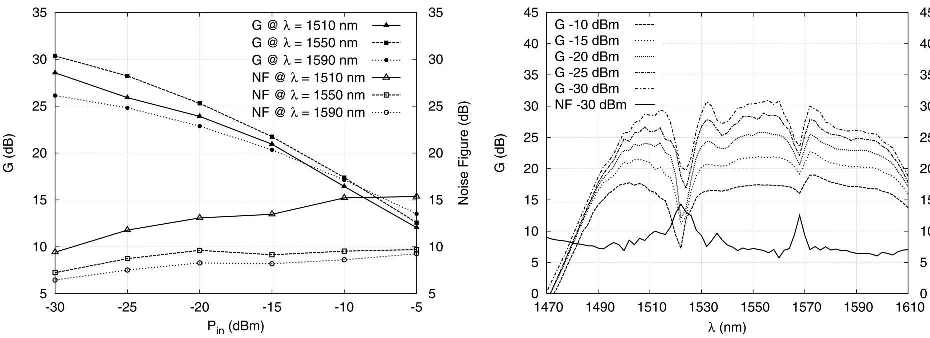

(a) (b)

Figure **3.13**: (a) Gain and noise figure versus the signal input power at 1510 *nm*, 1550 *nm* and 1590 *nm*. (b) Gain and noise figure spectra of the S+C+L band EDFA for different signal power values between -30 and -10 *dBm*.

nm ÷ 1610 *nm* has been measured. Despite of the WDM couplers bandgap losses, a gain of almost 20 *dB* has been obtained in a 120 *nm* wavelength range, between 1490 *nm* and 1610 *nm*, for a signal input power of -30 *dBm*.

The amplifier performances have been then analyzed by simultaneously launching nine signals with a channel spacing of 10 *nm*. The output power spectra measured for the considered WDM configuration are reported in Fig. 3.14a and Fig. 3.14b for an input power of -30 and -15 *dBm/ch*, respectively. The channel wavelengths, reported in the label of Fig. 3.14, cover the entire S+C+L band. As a comparison, the values previously measured with a single channel have been also shown. Notice that, by considering the lower signal input power, that is -30 *dBm/ch*, the output power values of the nine signals are almost the same of those measured with a single channel. In fact, the output power decrease is about 3 *dB* for the channel at 1530 *nm* and lower than 2 *dB* for the others. If the signal input power increases to -15 *dBm/ch*, as shown in Fig. 3.14b, a significant difference has been obtained for the signals at 1530 and 1540 *nm*. In fact, the output power decreases of about 13 *dB* and 7 *dB*, respectively. On the contrary, the difference with respect to the single channel case is about 5 *dB* and of 2 *dB* for the other channels in S+C band and for the ones in L band, respectively. This causes a reduction of the S+C+L band DP EDFA bandwidth towards the lower wavelengths in the C band.

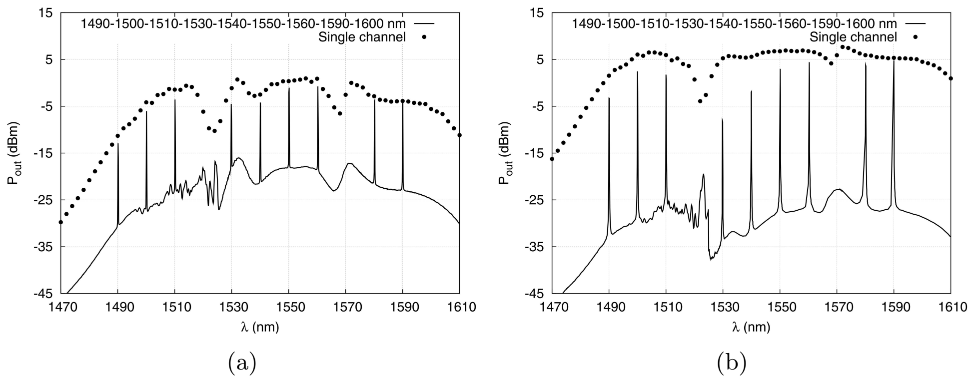

Figure **3.14**: Output power obtained with a single tunable channel and nine signals at different wavelengths for an input power of (a) -30 dBm/ch and (b) -15 dBm/ch.

In conclusion, the parallel configuration, the DP scheme and the all-silica erbium-doped fiber used in all the three modules result in a very efficient, reliable and technologically robust amplifier. Its analysis reveals a very wide gain spectrum, never reported up to day for a triple band all-silica EDFA, which allows an uniform spectral distribution of the signals.

3.6 Tunable multiwavelength EDFRL

While all the previous results regard the amplification process, here the experimental analysis of the performances of multiwavelength EDF lasers designed and realized during the PhD course is reported.

Tunable multiwavelength lasers are interesting for many applications, including optical communications, medicine, fiber optic sensors and optical instrument testing [128]. Due to the relatively large homogeneous gain broadening, the simultaneous multiwavelength lasing in an EDF is very sensitive to the cavity loss variations [129]. Recently, in order to overcome the cross-saturation between different wavelengths, a C band three-wavelength fiber laser has been proposed with three EDFAs in ring cavities, which provide gain for each lasing wavelength [130]. One of these wavelengths can be changed in the C band by properly tuning an optical filter [130]. Other tuning mechanisms have been

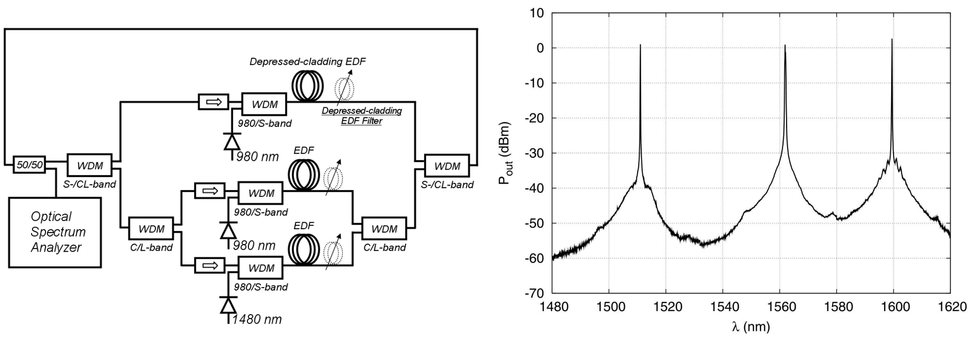

(a) (b)

Figure **3.15**: (a) Detailed scheme of the proposed tunable triple-wavelength EDFRL. (b) Output spectrum of the triple-wavelength laser beams obtained without filtering.

proposed in literature for multiwavelength EDF lasers. For example, active overlapping linear cavities have been used [128], as well as a high birefringence fiber loop mirror [131], sampled chirp fiber Bragg gratings [132] or a self-seeded Fabry-Pérot laser diode incorporated with a tunable bandpass filter [133].

Here a new technique to widely tune a multiwavelength EDFRL featuring a simultaneous three-wavelength output in S, C and L band has been experimentally demonstrated. In the proposed scheme three ring cavities, one for each optical band, have been considered. Moreover, the lasing effect has been extended to the S band by exploiting the bending losses of the depressed-cladding EDF [117], rather than its fundamental mode cut-off [116], in order to suppress the ASE in the C band. The tuning method here proposed is based on a simple tunable filter realized by inserting a 1 m-long depressed-cladding EDF with a proper bending diameter in each ring cavity. In fact, it has been already experimentally demonstrated that by properly exploiting the fiber bending losses it is possible to tune the gain spectrum between S and C band for depressed-cladding EDFAs [134].

Fig. 3.15a reports the detailed scheme of the proposed triple-wavelength EDFRL, which has been realized with three interconnected fiber ring cavities. In each ring a single stage EDFA module with a classical co-propagating scheme based on a WDM coupler has been inserted. Laser diodes at 980 nm with 50 mW and 56 mW power have been employed to pump the EDF in the

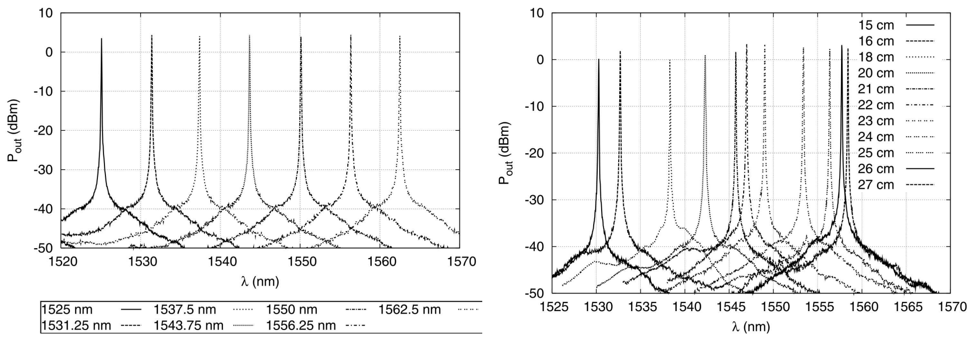

Figure **3.16**: Three-wavelength laser tuned in C band by using (a) a conventional tunable filter and (b) a filter based on the depressed-cladding EDF with different bending diameters.

S and the C band module, respectively, while a 1480 *nm* laser, providing 52 *mW* of optical power, has been used as the L band module pump. The length of the EDF is 11 *m*, 15 *m* and 100 *m* in the amplifier module for S, C and L band, respectively. For the S band EDFA the depressed-cladding silica-based EDF whose characteristics has been previously described has been considered [117, 134]. Notice that a depressed-cladding EDF bending diameter of 14 *cm* has been chosen in order to properly suppress the ASE in the C band, thus obtaining output lasing in S band. An optical isolator has been inserted into each ring to ensure unidirectional operation. The output light has been routed to an OSA through one port of a 3-*dB* fiber coupler. A resolution bandwidth of 0.05 *nm* has been used to display the laser output. The output of the proposed multiwavelength ring laser, obtained without filtering, is shown in Fig. 3.15b. Three laser lines centered at 1511, 1562 and 1600 *nm* have been obtained, with a peak power of 1 *dBm*, 1 *dBm* and 2.6 *dBm*, respectively. A threshold power of 14, 7 and 26 *mW* has been measured for the S, C and L band laser, respectively.

It has been investigated how the wavelengths of the EDFRL here realized can be tuned, thus obtaining a simultaneous three-wavelength tunable laser. As an example, Fig. 3.16a reports different laser lines measured in the C band by properly acting on a conventional tunable filter inserted in the corresponding cavity. The C band laser has been tuned down to 1525 *nm*, while the two lines in S and L band have been held steady. Then the filter realized with a 1-*m* long depressed-cladding EDF has been added in each cavity, as reported in the scheme of Fig. 3.15a. The bending diameter of the doped fiber in each filter has been properly changed, in order to tune the laser wavelength in the three bands. For the C band laser tuning it is necessary to bend the depressed-cladding fiber in order to measure a significant change in the wavelength. In particular, only for a bending diameter smaller than 27 *cm* it is possible to shift the C band laser to a wavelength lower than the one obtained without filtering, that is 1562 *nm*. As shown in Fig. 3.16b, when the bending diameter changes from 27 to 15 *cm*, the laser wavelength moves from 1558 to 1530 *nm*. A maximum output power of 3.3 *dBm* has been achieved at 1547 *nm*, while it drops to a minimum of 0 *dBm* at 1538 *nm*. A successful tuning mechanism without a significant spectrum distorsion has been thus experimentally demonstrated in a 32 *nm* wavelength range.

The same tuning mechanism has been applied to the S band laser, as shown in Fig. 3.17a. In this case it is necessary to consider bending diameter values lower than 10 *cm*, in order to obtain high bending losses in the desired wavelength range [117] and, consequently, to properly change the laser wavelength. In particular, the S band laser line has been moved to 1508, 1503, 1500, 1495 and 1491 *nm* by bending the depressed-cladding EDF with a diameter of 9, 8, 7, 6.5 and 6 *cm*, respectively. By shifting the laser towards the lower wavelengths, the output power decreases, due to the insufficient S band EDFA gain. In particular, a maximum output power of -1.8 *dBm* has been obtained at 1508 *nm*, which decreases to -6 *dBm* at 1491 *nm*.

Finally, the tunable filter for the L band laser has been designed. Due to the fundamental mode cut-off of the depressed-cladding EDF, which is around 1590 *nm*, the losses introduced in L band by the filter previously described are too high. Only with an un-bent depressed-cladding fiber a laser line has been obtained at 1573 *nm*, as shown in Fig. 3.17b. This wavelength is close to the L band lower edge, thus preventing a further tuning through the bending loss increase, as already demonstrated in S and C band. As a consequence, the depressed-cladding EDF in this filter has been shortened, in order to reduce the losses of the straight fiber and to exploit again the bending effect. Different values of the EDF length L have been considered, that is 60, 30, 15 and 10 *cm*. Fig. 3.17b reports the laser line obtained with a 15-*cm* long depressed-cladding fiber, which is at 1586 *nm* when the EDF is straight and can be tuned to 1584, 1581, 1578, 1575 and 1570 *nm* by choosing a proper bending

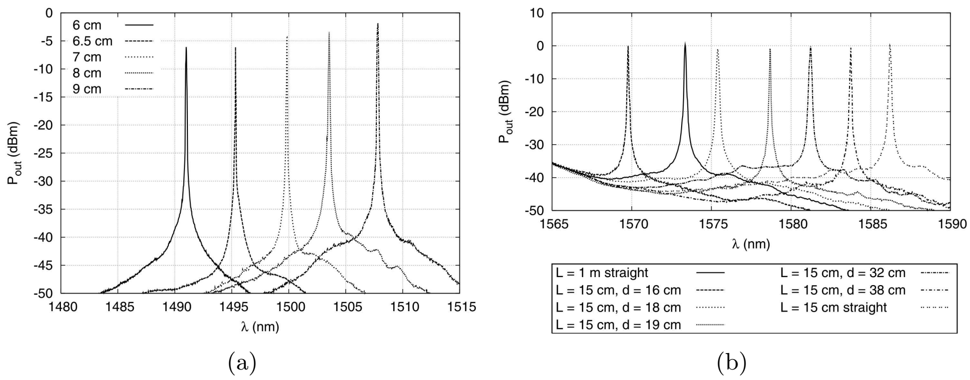

Figure **3.17**: Three-wavelength laser tuned (a) in S band and (b) in L band by using the filter based on the depressed-cladding EDF with different lengths L and bending diameters d.

value between 32 and 16 cm. A maximum output power of 0 dBm has been obtained at 1570 nm. Moreover, the output power is almost constant inside the wavelength tuning range, being the ripple lower than 1 dB. Notice that the L band laser can be moved in a wavelength range of about 30 nm, that is from 1600 nm, in the absence of the filter, to 1570 nm.

3.7 Tunable single frequency EDFRL

Many optical communication applications require EDFRLs with special features, such as a narrow linewidth, a high optical power emission and wavelength tunability easy to achieve. Several techniques have been proposed to obtain a single frequency operation for fiber ring lasers. For example, one of them employs several internal ring cavities to filter the longitudinal modes [135]. Other techniques exploit a semiconductor optical amplifier operating as a bandpass filter [136], or an intracavity phase-shifted fiber Bragg grating (FBG) narrow-band filter [137]. Moreover, by using a section of EDF as a saturable absorber [42,138], or by employing Sagnac loop filters [139] single longitudinal mode operation has been achieved. A wide tunability wavelength range is another critical point for EDFRLs. Conventionally, a fiber Fabry-Perot filter is used for wavelength tuning. However, in recent years, many

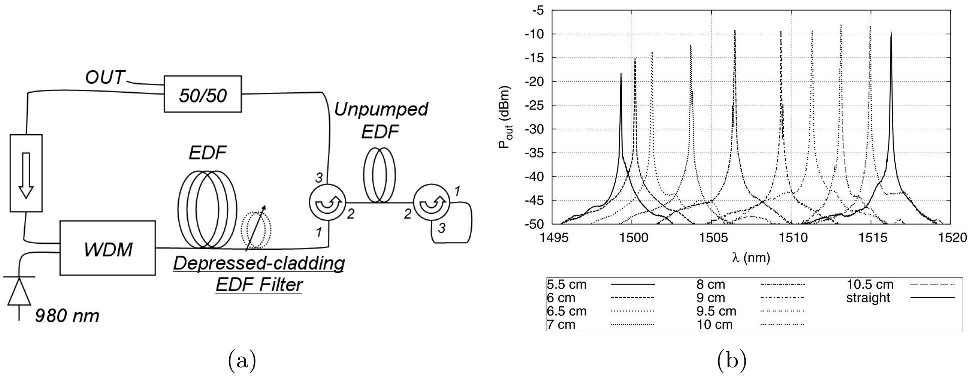

Figure **3.18**: (a) Experimental setup of the proposed tunable single frequency EDFRL. (b) Spectra of the tunable S band laser for different bending diameters of the depressed-cladding EDF filter.

other techniques have been investigated. For example, three cascaded filters have been exploited to obtain a 70 nm wide quasi-continuously tunable single frequency EDFRL [140]. As an alternative, a 40 nm continuous tuning range has been achieved using a highly stretchable FBG [141].

Differently from the previous Section, where a tunable filter based on a 1 m-long depressed-cladding EDF inserted in the ring cavity has been used to widely tune a multiwavelength EDFRL, here the same tuning mechanism has been adopted for a single frequency EDFRL in S band, as well as in C band. Moreover, the single longitudinal mode oscillation has been guaranteed by using a section of EDF as a saturable absorber [42, 138].

The configuration of the proposed EDFRL with single frequency and wavelength tuning operation is shown in Fig. 3.18a. The active region of the laser consists of an EDFA module with a classical copropagating scheme. The EDF is pumped by a 980 nm laser diode through a WDM coupler. The optical power is finally extracted using a 50:50 splitting fiber coupler. The ring cavity is unidirectional, as ensured by inserting an optical isolator, which suppresses the unwanted reflections. In order to guarantee a single longitudinal mode oscillation, an unpumped EDF is used as a saturable absorber in the cavity. This EDF is added to the cavity through a circulator, which also acts as an isolator to provide unidirectional operation. A second circulator, whose port 1 is connected to port 3, is used at the unpumped EDF end to allow the double

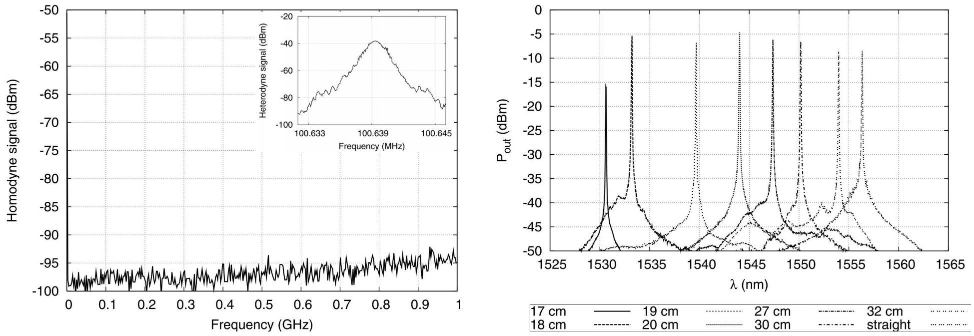

(a) (b)

Figure **3.19**: (a) RF spectrum of the fiber ring laser with the saturable absorber. Inset: self heterodyne frequency spectrum of the S band laser output at 1513 nm. (b) Spectra of the tunable C band laser for different bending diameter values of the depressed-cladding EDF filter.

passage of the signals inside the doped fiber. The tunable filter proposed has been realized with a 1 m-long depressed-cladding EDF and inserted inside the laser cavity, as reported in Fig. 3.18a. The bending diameter of the doped fiber has been properly changed to tune the laser wavelength. In order to analyze the tuning behaviour in S band, as well as in C band, the tunable filter has been inserted in two different EDFRL cavities, based on the same scheme shown in Fig 3.18a. In the first one the same depressed-cladding EDF exploited as a tunable filter has been used as the active fiber, pumped by a laser diode at 980 nm with a power of 50 mW. The length of the depressed-cladding EDF is 15 m and the bending diameter has been chosen equal to 14 cm, in order to suppress the ASE in C band, thus obtaining output lasing in S band. The second cavity is based on a 11 m-long C band EDF, pumped with 60 mW at 980 nm. An OSA with a resolution of 0.05 nm has been used to measure the emission wavelengths and powers of the proposed fiber lasers. Furthermore, the single frequency performances have been verified by using the self homodyne method by detecting the laser light with a photodetector and a Radio Frequency (RF) spectrum analyzer.

The S band single frequency EDFRL has been obtained with a 0.5 m-long unpumped EDF. Fig 3.18b reports the output power of this proposed single frequency fiber laser in a wavelength range of 17 nm. By considering

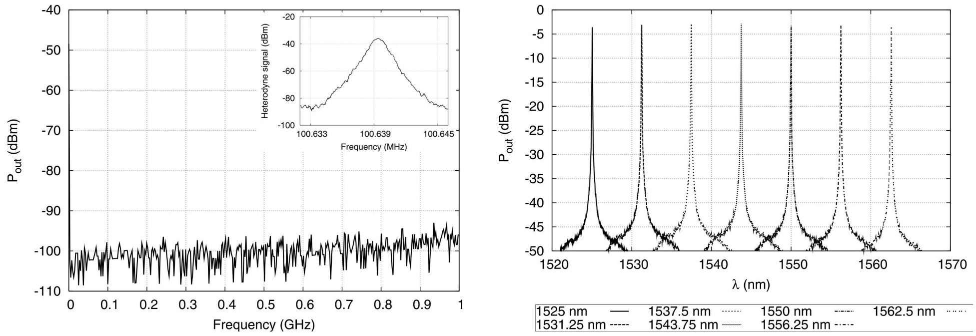

(a) (b)

Figure **3.20**: (a) RF spectrum of the fiber ring laser with the saturable absorber. Inset: self heterodyne frequency spectrum of the C band laser output at 1545 nm. (b) Spectra of the C band EDFRL tunable through a conventional filter.

the straight depressed-cladding EDF filter, a laser line at 1516 nm has been measured. In order to obtain high bending losses in the desired wavelength range and, consequently, to properly change the laser wavelength, it is necessary to consider bending diameter values lower than 10 cm. In particular, the S band laser line has been tuned from 1515 nm to 1499 nm by bending the depressed-cladding EDF filter with a diameter between 10 and 5.5 cm. When the laser shifts towards the lower wavelengths, the output power decreases, due to the insufficient S band EDFA gain. In particular, a maximum output power of -8 dBm has been obtained around 1513 nm. The emission power decreases to -18.2 dBm at 1499 nm. In order to verify the single frequency operation, the EDFRL RF spectrum has been analyzed by using the self homodyne detection technique. Fig. 3.19a reports the RF spectrum of the laser at 1513.3 nm measured with a resolution bandwidth of 1 kHz. The absence of tones corresponding to a multi-mode lasing demostrates the single frequency laser oscillation. The self heterodyne frequency spectrum of the laser output is reported in the inset of Fig. 3.19a. It is important to underline that a half width at half maximum of 0.8 kHz has been measured.

The same tuning mechanism has been then applied to the C band EDFRL, whose single frequency operation has been obtained by inserting 1.20 m-long unpumped EDF in the cavity. A single frequency laser line at 1560 nm has been obtained by considering the straight EDF filter, as shown in Fig. 3.19b. In order to measure a significant change in the laser wavelength, it is necessary to bend the depressed-cladding EDF with a diameter smaller than 32 cm. In fact, when the bending diameter changes in the range 32 $\div$ 16 cm, the laser wavelength tunes from 1554 to 1530 nm. A maximum output power of -4.6 dBm has been obtained around 1545 nm, while it drops to -15.8 dBm and -8.6 dBm at 1530 nm and 1554 nm, respectively. The homodyne frequency spectrum shown in Fig. 3.20a confirms the single longitudinal mode operation of the laser at 1545 nm, whose linewidth is 0.7 kHz, as reported in the inset of Fig. 3.20a. In order to evaluate the perfomances of the tuning method here proposed, the tunable filter realized with the depressed-cladding fiber has been substituted with a conventional one in the C band EDFRL cavity. The single longitudinal mode oscillation has been maintained by using the same saturable absorber previously exploited for the C band EDFRL. Fig. 3.20b reports the output power of the laser tuned in the wavelength range 1525 $\div$ 1565 nm. Notice that the laser linewidth, being 0.6 kHz at 1550 nm, as shown in the inset of Fig. 3.20b, is almost the same obtained with the tuning method here proposed, even if a conventional filter provides a larger tuning range.

3.8 Active fiber as tunable filter for EDFRLs

During the PhD activity, a new technique has been experimentally demonstrated in order to obtain a tunable doped fiber laser in unusual bands, different from the conventional one, that is the C band. The method here proposed exploits the bending losses of the depressed-cladding EDF, used as the active fiber, as well as the tunable filter.

The configuration of the proposed single frequency EDFRL is shown in Fig. 3.21a. The active region of the laser consists of an amplifier module with a classical co-propagating scheme. The doped fiber is pumped by a 980 nm laser diode, with a power of 50 mW, through a WDM coupler. The optical power is extracted by using a 50/50 splitting fiber coupler. The ring cavity is unidirectional, as ensured by the optical isolator, which suppresses the unwanted reflections. In order to guarantee a single longitudinal mode oscillation, an unpumped EDF, whose absorption spectrum is reported in Fig. 3.21b, is used as a saturable absorber in the cavity. This EDF is inserted into the cavity through a circulator, which acts as an isolator to provide unidirectional operation. By adding at the unpumped EDF end a second circulator,

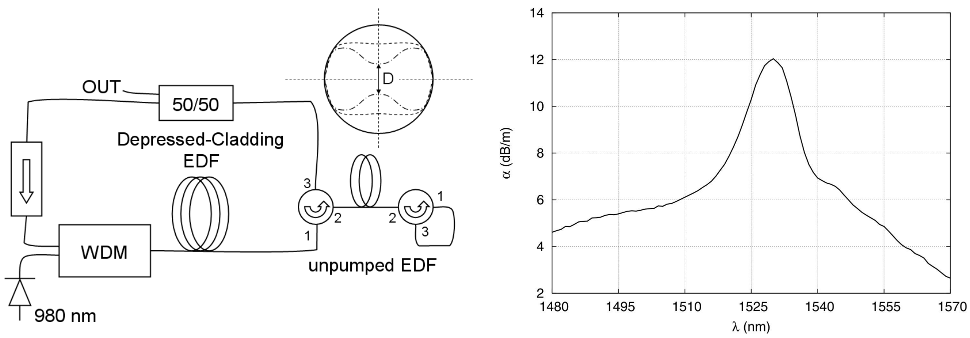

(a) (b)

Figure **3.21**: (a) Experimental setup of the proposed tunable single frequency EDFRL. Inset: elliptical structure to dinamically tune the laser wavelength. (b) Absorption spectrum of the saturable absorber EDF.

whose port 1 is connected to port 3, a standing wave is established [138]. The depressed-cladding EDF here exploited as the active fiber, as well as the filtering element is the same which has been previously used to realize the amplifiers so far described [127,134]. The 15 m-long doped fiber has been wrapped on an elliptical structure, as reported in the inset of Fig. 3.21a, with a major axis of 30 cm and a minor one D, whose value has been changed in the range $5 \div 30$ cm. In fact, by properly changing the bending losses of the depressed-cladding EDF [134], it is possible to tune the laser emission wavelength in S band. An OSA with a resolution of 0.05 nm has been used to measure the emission spectrum and the power values of the proposed fiber laser. Furthermore, the single frequency performances have been verified by using the self homodyne method by detecting the laser light with a photodetector and a RF spectrum analyzer.

Fig. 3.22a reports the output power spectra of the proposed tunable single frequency EDFRL measured by varying the diameter D. Notice that a wide tuning range of 44 nm, comprising the S band and the lower wavelengths of the C one, has been obtained. By considering the depressed-cladding EDF wrapped with a D value of 30 cm, a laser line at 1535 nm has been measured. In order to shift the laser wavelength towards the S band, it is necessary to introduce significant bending losses at the higher wavelengths, that is to reduce the D value. In particular, the laser line has been tuned from 1535

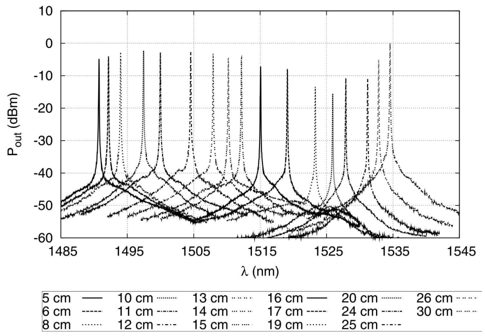

(a)

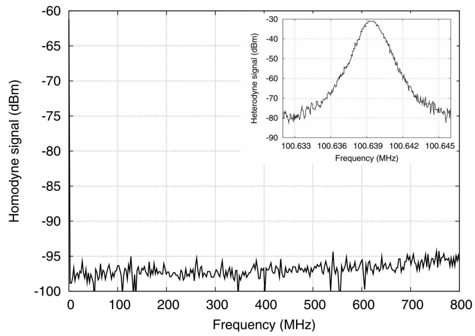

(b)

Figure **3.22**: (a) Output spectra of the proposed EDFRL for different D values. (b) RF spectrum of the fiber ring laser with the saturable absorber. Inset: self heterodyne frequency spectrum of the C band laser output at 1510 nm.

nm to 1491 nm by wrapping the doped fiber with D between 30 and 5 cm. A maximum output power of -2.2 dBm and 0.1 dBm has been obtained at 1497 nm and at 1535 nm, with a D value of 10 and 30 cm, respectively. Notice that the laser power is almost constant inside the wavelength range 1491 $\div$ 1508 nm, being the ripple lower than 3 dB. However, when the laser tunes from 1535 nm to around 1526 nm, by reducing D from 30 to 20 cm, the output power decreases reaching a minimum of -15.5 dBm. In order to explain the presence of this minimum in the laser emission power, the effect of the absorption due to the unpumped EDF has been investigated. The ASE spectra before and after the unpumped doped fiber have been measured for different D values. In particular, the saturable absorber influence has been evaluated by comparing the ASE power at the output of the first circulator, that is before the unpumped EDF, and at the input of the second one. Results demonstrate that by bending the active fiber, the ASE maximum peak power shifts towards the S band and that the unpumped attenuation is so strong that it avoids high power laser emission. In fact, by considering D = 20 cm, a significant decrease in the emitted ASE power after the unpumped EDF is observed. As a consequence, it is possible to deduce that the laser emission wavelength and its associated output power are strongly influenced by the bending losses of the depressed-cladding EDF, as well as by the absorption due to the unpumped

EDF, necessary to obtain single-mode longitudinal behaviour.

Finally, in order to verify the single frequency operation, the EDFRL RF spectrum has been analyzed by using the self homodyne detection technique. Fig. 3.22b reports the RF spectrum of the laser at 1510 nm, measured with a resolution bandwidth of 1 kHz. The absence of tones corresponding to a multi-mode lasing demonstrates the single frequency laser oscillation. The single longitudinal mode operation has been maintained inside the whole tunability range. The self heterodyne frequency spectrum of the laser output is reported in the inset of Fig. 3.22b. It is important to underline that a half-width at half-maximum of 0.6 kHz at 1510 nm has been measured.

Chapter 4

Ytterbium-doped fiber amplifiers

During the last part of the PhD course the research activity has been devoted to the design and the experimental realization, in collaboration with Quanta System S.p.A., of an amplifier based on ytterbium-doped fibers, which will be employed for the pulse pre-amplification in a Master Oscillator Power Amplifier (MOPA). The two-stage pre-amplifier is required to amplify short pulses at 1064 nm, with a peak power between 200 mW and 1 W, and a temporal duration up to 20 ns, to the kW-level, with an overall gain of about 30 dB. In order to realize the pre-amplifier with these performances, single-mode single-cladding ytterbium-doped fibers have been considered, pumped by single-mode grating-stabilized lasers at 976 nm, usually exploited in telecommunication applications.

After a brief description of the characteristics of the amplifiers based on ytterbium-doped fibers, the two stages of the pre-amplifier realized during the PhD activity will be presented in detail. Measurement results regarding the performances of each stage will be reported and discussed.

4.1 Ytterbium-doped fibers

Since its invention in 1985, the EDFA [142–144] has attracted great interest, principally by virtue of its major commercial applications in the field of communication technology. However, the uses of EDFAs have not been confined to telecommunications and there has been steadily growing interest, for example, in the amplification of pulses to provide a source of very high peak powers. In such a context, where the specific wavelength advantage of the EDFA for telecommunications is no longer relevant, amplifiers based on other rare-earth dopants offer themselves for consideration.

Ytterbium-doped fibers are a case in point. While they have been used mainly for lasers so far [145–150], their ability to provide amplification over the very broad wavelength range from 975 nm to 1200 nm is expected to generate increasing interest in the near future. Apart from their broad-gain bandwidth, Ytterbium-Doped Fiber Amplifiers (YDFAs) can offer high output power and excellent power conversion efficiency. Many of the complications which are well-known from EDFAs are avoided, that is excited state absorption and concentration quenching do not occur, and high doping levels are possible, leading to high gain in a short fiber length. The broad bandwidth is ideal for the amplification of ultrashort pulses, and the high saturation fluence allows for high pulse energies. There is also a wide range of possible pump wavelengths, from 860 nm to 1064 nm, allowing a variety of pumping schemes, including the use of diode lasers or even high-power Nd lasers. Although the Ytterbium (Yb) ions can be pumped at several wavelengths to obtain inversion for the 1064 nm transition, only the pump bands around 9XX, that is around 915 nm and 976 nm, are of practical interest because of the availability of semiconductor lasers that operate at these two wavelengths and the deleterious effects of excited state absorption at some of the other pump bands.

Recently, lasers and amplifiers have progressively replaced mechanical and electrical tools in different applications, so these devices have permanently to be improved and adapted to new requirements. Naturally, also cost- and energy-efficiency are of highest priority. Possible applications of YDFAs include power amplification at special wavelengths, for example 1083 nm, as required for spectroscopic measurements [151], small-signal amplification in fiber sensing, free-space laser communications, and chirped-pulse amplification of ultrashort pulses, which can themselves be produced in an Yb-doped fiber laser [152].

Research in laser systems based on Yb-doped fibers is progressing rapidly in continuous-wave format, as well as in pulsed configurations. The achievements so far obtained might give the impression that Yb-doped fiber laser and amplifier technology has reached a high level of maturity and that constructing ytterbium systems is a straightforward process. However, it is to be appreciated that Yb-doped fiber lasers and amplifiers are quite difficult to design and optimize in practice.

4.1.1 Ytterbium spectroscopic properties

Silica glass, the most common material for the optical fiber production, is an ideal host for Yb^{3+} ions for a lot of applications, although other host materials are subject of investigation, that is fluoride glasses in fiber form [148] and numerous crystalline hosts for use in bulk or waveguide form.

The spectroscopy of the Yb^{3+} ion is simple compared to other rare-earth ions. For all optical wavelengths, only two level manifolds are relevant, that is the $^2F_{7/2}$ ground-state manifold and the $^2F_{5/2}$ excited-state one. These consist of four and three sublevels, respectively. The corresponding transitions between sublevels are not fully resolved for Yb^{3+} ions in a glass at room temperature because of the strong homogeneous and inhomogeneous broadening.

Fig. 4.1a shows the absorption and emission cross sections of Yb^{3+} ions in a germano-silicate glass published by Paschotta et al. [152]. Notice that an efficient pumping is possible around 910 nm wavelength, or near 975 nm. In the latter case, the pump linewidth must be small, and only 50% excitation level can be achieved, due to the stimulated emission. However, the absorption length and the quantum defect are smaller. A strong three-level behavior occurs for lasing around 1030 nm, while a nearly four-level behaviour is observed beyond 1080 nm, where there is very little reabsorption. It is important to underline that the details of absorption and emission spectra depend to some extent on the host glass composition [153, 154].

Ytterbium doping is also often used together with the erbium one. Typically, the Yb^{3+} ions absorb the pump radiation and transfer the excitation energy to the erbium ones. Even though the erbium ions could directly absorb radiation at 980 nm, ytterbium codoping can be useful because of the higher ytterbium absorption cross sections and the higher possible ytterbium doping density in typical laser glasses, so that a much shorter pump absorption length and a higher gain can be achieved. Ytterbium codoping is also sometimes used for praseodymium-doped upconversion fiber lasers.

4.1.2 Photodarkening

An important detrimental effect in Yb-doped fibers is photodarkening, that is a gradual fiber degradation observed particularly in cases where a high ytterbium excitation density is required. Photodarkening is a phenomenon that induces a permanent increase in the core background loss of the doped fiber. It has been observed in silica fiber doped with different rare-earth elements, such as thulium, europium, praseodymium and cerium [155–157]. When light propagates in the core, such as for the pumping, Yb-doped fibers can exhibit severe transmission losses, which are strongest at short wavelengths and much weaker around the 1 μm spectral region, where Yb-doped fiber lasers and amplifiers operate. Such losses can occur in new fibers [158], but can also grow during operation of a fiber laser or amplifier [159, 160]. The loss growing rate appears to be proportional to the seventh power of the density of excited Yb^{3+} ions. This means that a fast degradation of Yb-doped fibers can result from operation with high fractional ytterbium excitation density, particularly for fibers with high doping concentration and poor homogeneity. On the other hand, the strong dependence on the excitation density suggests that many devices can be designed to operate in a relatively safe operation regime, where long lifetimes can be expected. Difficult cases are those where a high doping concentration is required, in order to mitigate nonlinear effects via a reduced fiber length, or where high excitation levels are inevitable.

4.1.3 Stimulated Brillouin Scattering

The power of single transverse mode fiber laser oscillators has increased dramatically in recent years with several reports in literature of powers in excess

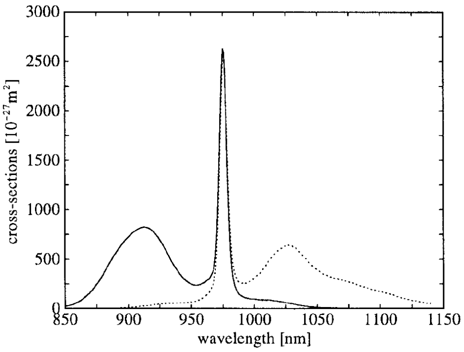

(a)

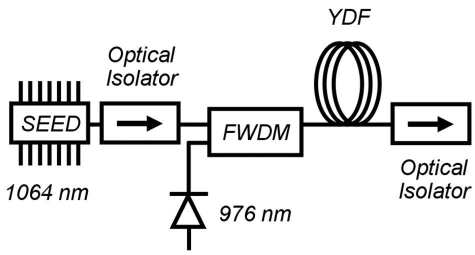

(b)

Figure **4.1**: (a) Absorption (solid) and emission (dotted) cross-sections of Yb in germano-silicate glass. (b) Experimental setup of the MOPA with a single stage.

of 1 kW [161–163]. In such laser oscillators, the linewidth is typically tens of nanometers. This broad linewidth is of no consequence for many applications, such as materials processing, where simply high power and good beam quality are desired. However, many applications, including coherent beam combination, ladar, nonlinear frequency conversion and gravitational wave detection, require high output power, good spatial beam quality and narrow linewidth operation to be combined in a single device.

Narrow linewidth signals require a MOPA configuration rather than a laser oscillator, where, due to typical cavity lengths of several meters, the discrimination of closely spaced longitudinal modes is difficult.

The primary limitation on the output power from narrow linewidth devices is the onset of Stimulated Brillouin Scattering (SBS). SBS occurs in an optical fiber when the signal propagating in the core generates an acoustic wave through the process of electrostriction. The acoustic wave scatters light in the reverse direction and reduces the forward propagating power [164]. In fact, the signal wave traveling in a fiber amplifier generates Brillouin gain for a backward traveling Stokes wave with slightly lower optical frequency [165], that is around 18 GHz for a 1 μm signal. Because of the small bandwidth of the Brillouin gain, that is 38 MHz in silica fibers for a 1 μm signal, only signals with high spectral density can lead to high Brillouin gain and to the generation of a Brillouin wave which can extract significant power. This is especially the case when a single-frequency signal is amplified to a high power level. For example, there is interest in amplifying a single-frequency beam at 1083 nm used for spectroscopy on metastable helium to high powers [151], and the consideration of Brillouin gain is important in such a case.

The use of large mode area fibers to decrease the optical intensity in the fiber core has been exploited to raise the SBS threshold. However, the maximum output power from narrow linewidth optical fiber amplifiers is still limited to approximately 100 W [166]. Power levels as high as 500 W have recently been achieved through the use of a pump induced thermal gradient in a counter-pumped fiber amplifier [167]. However, the use of temperature gradients to increase the SBS threshold is limited to single ended pumping because two-end pumping or distributed pumping will decrease the temperature gradient in the fiber [168]. By reducing the overlap between the optical and acoustic fields, it is possible to generate over 500 W of output power even in a bidirectional pumping [169].

4.2 Pre-amplifier characteristics and performances

The pronounced structure in the Yb absorption and emission spectra has some implications for the design of YDFAs which do not arise in the case of EDFAs. In fact, there are distinctly different regimes of operation depending on pump and signal wavelength. The narrow absorption peak at 975 nm, and the broader and weaker peak at 910 nm offer the obvious choices for pump wavelengths. However, longer wavelengths, like 1047 nm or 1064 nm or even the short wavelengths at 860 nm or less, may be used, provided that suitable diode lasers are available. Gain can be achieved on the 975 nm emission peak or over a range of wavelengths on the much broader peak centered at 1030 nm. Of course, gain is available only at wavelengths longer than the pump wavelength.

During the PhD activity, a two-stage pre-amplifier for a high power MOPA has been designed and realized. Single-cladding, single-mode Yb-doped fibers commercially available have been used, being the most suitable for this application. In these fibers both signal and pump have similar mode overlap with the Yb-doped core.

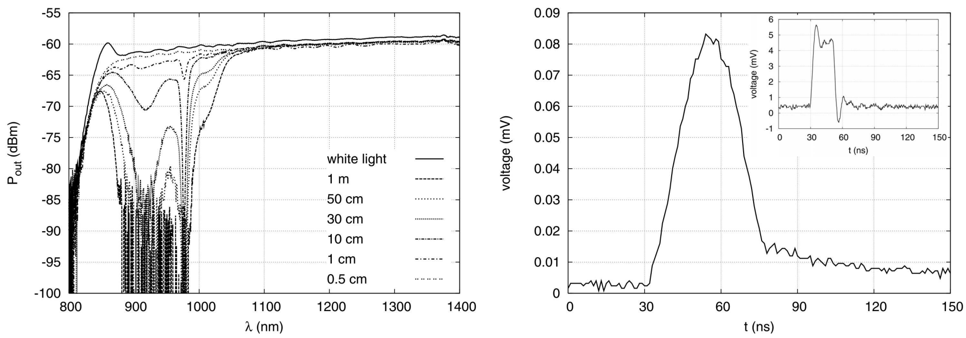

(a) (b)

Figure **4.2**: (a) Transmission spectra of different lengths of Nufern SM-YSF-HI fiber obtained with the white light source. (b) Shape of the pulse with duration of 20 ns at the seed output. Inset: shape of the corresponding electrical signal.

4.2.1 First stage

The configuration of the first stage of the pre-amplifier is shown in Fig. 4.1b. The amplifier is based on a single-mode Yb-doped fiber made by Nufern, that is Nufern SM-YSF-HI. This fiber presents a core diameter of 6 μm, a cladding diameter of 125 μm, a numerical aperture of 0.11, and an unsaturated absorption coefficient of approximately 250 dB/m at 976 nm. This peak value is confirmed by the attenuation spectra reported in Fig. 4.2a for different fiber lengths. These measurement results have been obtained by coupling a broadband white light source, whose spectrum is shown with a solid line. Looking at the behaviour of the 1 cm-long doped-fiber, it is possible to notice the attenuation peak of about 2.5 dB at 976 nm due to the Yb^{3+} ions. By considering longer fiber samples, very high attenuation values have been measured. Notice that different lengths of the Yb-doped fiber have been considered with the aim to maximize the amplifier gain while maintaining stability, as well as operation free from parasitic lasing or self-pulsations. Measurement results have demonstrated that the optimum length of the Yb-doped fiber is 3 m.

The Yb-doped fiber is pumped with a single-mode grating-stabilized fiber-pigtailed laser diode at 976 nm with a maximum output power of 300 mW. By exploiting the injection-seeding technique, a seed providing square pulses at 1064 nm with a peak power of 500 mW, duration between 5 ns and 100

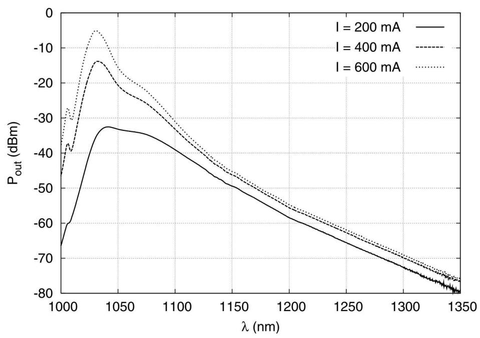

(a)

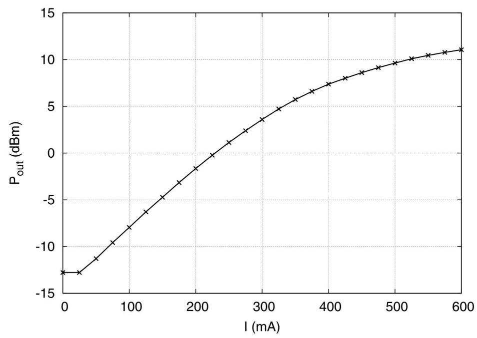

(b)

Figure **4.3**: (a) ASE spectra for different values of the pump laser current measured with the first stage amplifier setup. (b) Output power of the MOPA as a function of the pump current for 20 ns pulses.

ns and repetition rate up to 100 kHz has been used as the input signal. The 20 ns square pulse shown in Fig. 4.2b with 10 nJ of energy at a repetition rate of 20 kHz has been considered for the measurements. As a comparison, the electric signal is reported in the inset of Fig. 4.2b. As shown in Fig. 4.1b, a first isolator has been used at the seed output to prevent feedback which could affect the seed performances, while a second one has been added at the amplifier output in order to avoid power feedback into the doped-fiber. Through the first isolator, a signal power of -8.5 dBm is coupled into the amplifier when 20 ns pulses with a repetition rate of 20 kHz are considered. A single-mode filter WDM combines the seed light with the pump one into the Yb-doped fiber. The average power of the pulses at the amplifier output has been measured with a power meter, after suppressing the ASE power with a narrow-band filter centered at 1064 nm. A photodiode connected to an oscilloscope has been used to determine the temporal behaviour of the pulses.

By using the amplifier setup previously described, the ASE spectra have been measured with an OSA by turning off the signal power. As shown in Fig. 4.3a, the ASE power increases in the whole spectrum with the pump power current. In particular, a peak of -5 dBm has been obtained at 1030 nm for a pump current of 600 mA, which corresponds to a pump power of 300 mW.

Fig. 4.3b shows the average output power as a function of the pump current for the 20 ns pulses with a repetition rate of 20 kHz. Notice that the amplifier

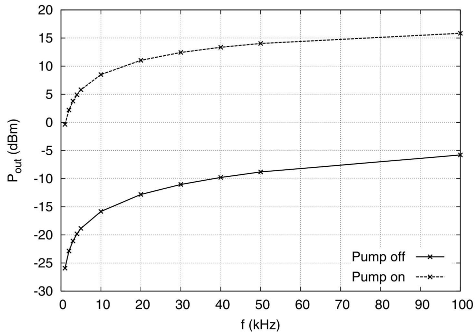

(a)

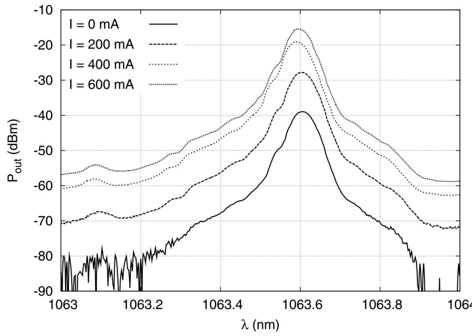

(b)

Figure **4.4**: (a) Output power of the MOPA umpumped and pumped with 300 mW of pump power as a function of the seed repetition rate for 20 ns pulses. (b) Optical spectrum of the signal at the amplifier output for different pump current values.

output power increases with the pump power, showing a maximum output power of 11.6 dBm when the pump current is 600 mA. As a consequence, a gain of 19 dB has been obtained, since the average input power of the pulses is -8.5 dBm in these conditions. Moreover, it is important to underline that, by turning off the pump power, a signal output power of -12.7 dBm has been measured, so the path loss can be estimated to be around 4 dB at 1064 nm. In order to better analyze the amplifier performances, the amplifier output power has been measured by changing the seed repetition rate. Results are reported in Fig. 4.4a. The signal output power measured by turning off the pump is plotted for comparison purpose. As expected, the signal power in the unpumped amplifier increases with a constant slope when the repetition rate becomes higher. On the contrary, a saturation can be noticed for the amplifier pumped with 300 mW when considering high repetition rate. For example, by doubling the frequency from 50 to 100 kHz, the average input power of the pulses increases of 3 dB. However, the output power of the MOPA become higher of only 1.8 dB, being $P_{out} = 14$ dBm and 15.8 dBm for the repetition rate of 50 kHz and 100 kHz, respectively.

In Fig. 4.4b the optical spectrum of the signal around 1064 nm at the MOPA output is reported for different pump power values. Notice that these spectra have been measured by using an optical attenuator at the OSA input.

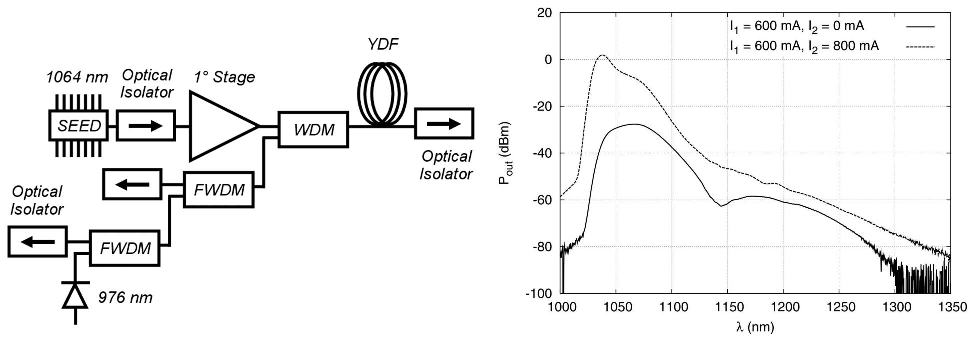

(a) (b)

Figure **4.5**: (a) Experimental setup of the two-stage MOPA. (b) ASE spectra for different pump current configurations.

4.2.2 Second stage with single-cladding Nufern fiber

In order to achieve higher output power values, a second stage has been added in the designed pre-amplifier with the setup reported in Fig. 4.5a. A fused WDM that combines the amplified seed light with the pump into the Yb-doped fiber has been used. Notice that a fused WDM has been preferred in order to exploit its lower insertion loss, as well as to avoid the filter WDM damage due to the high power values involved. The pump source is a single-mode grating-stabilized fiber-pigtailed laser operating at 976 nm, which delivers a maximum power of 500 mW for a current I_2 equal to 1 A. Two filter WDMs in series have been added on the pump path for additional protection and isolation of the laser from the high reflected power. 7 m of the same Yb-doped fiber considered in the first stage has been used. Notice that the doped-fiber length has been chosen in order to maximize the gain.

As previously reported for the first stage amplifier, the ASE spectra have been measured for different pump configurations. In particular, the ASE spectra obtained by pumping only the first stage with a current $I_1 = 600\ mA$, and by pumping both the amplifier stages with $I_1 = 600\ mA$ and $I_2 = 800\ mA$ are reported in Fig. 4.5b. A peak of -27.6 dBm at 1068 nm has been measured in the ASE spectrum. By turning on the second stage pump with a current I_2 of 800 mA, the peak value increases to 1.9 dBm and moves towards shorter wavelengths, that is 1037 nm. Notice the dip at 1145 nm in the ASE

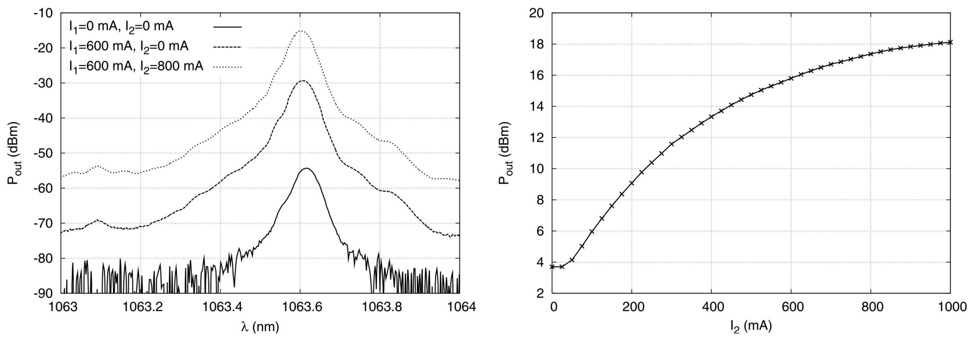

(a) (b)

Figure **4.6**: (a) Output optical spectrum for the two-stage MOPA for different pump current configurations. (b) Output power of the two-stage MOPA as a function of the second stage pump current I_2 with $I_1 = 600\ mA$. 20 ns pulses with a repetition rate of 20 kHz, and the single-cladding Nufern fiber have been considered.

spectrum obtained by pumping only the first amplifier, which is due to the filtering effect of the fused WDM. The same pump power configurations have been considered to measure the output spectrum of the seed, shown in Fig. 4.6a

The behaviour of the MOPA output power as a function of the pump current of the second amplifier is shown in Fig. 4.6b for 20 ns pulses with a repetition rate of 20 kHz, when the pump power in the first stage is maximum, that is 600 mA. Notice that a maximum output power of 18.1 dBm has been obtained for the maximum pump current $I_2 = 1\ A$. However, there is a significant saturation, since the output power is only slightly influenced by the pump power increase.

After that, a 2×2 99/1 splitting fiber coupler has been placed between the fused WDM and the doped-fiber of the pre-amplifier second stage, in order to monitor the light backward propagating in the whole amplifier. The aim of these measurements is to investigate the possible presence of a second peak, beside the signal one, due to the Brillouin scattering. Spectra measured for different pump current configurations are reported in Fig. 4.7a. Notice that, when the second stage pump is turned off, only the peak due to the signal can be identified in the spectrum, independently from the first stage pump current

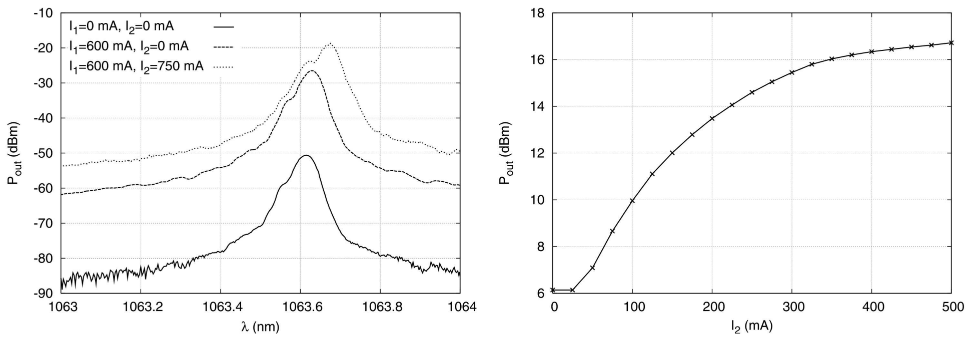

(a) (b)

Figure **4.7**: (a) Backward propagating light spectra measured with the Nufern fiber for different pump current configurations. (b) Output power of the two-stage MOPA with the single-cladding Liekki fiber as a function of the second stage pump current I_2 for the 20 ns pulses with a repetition rate of 20 kHz, and $I_1 = 600\ mA$.

value. As I_2 increases, a second spectral component, separated from the signal wavelength by 0.06 nm, which corresponds to the Brillouin frequency shift in silica near 1060 nm, appears and becomes stronger and stronger. As shown in Fig. 4.7a, when $I_2 = 750\ mA$, the peak due to the Brillouin scattering is higher in magnitude with respect to the signal one, thus indicating a significant increase in the relative level of the Brillouin scattered light.

4.2.3 Second stage with single-cladding Liekki fiber

Another single-cladding, single-mode Yb-doped fiber made by Liekki, that is Yb1200-4/125, has been considered in the pre-amplifier second stage. This fiber is characterized by a core and a cladding diameter of 4 μm and 125 μm, respectively, a numerical aperture of 0.2 and an unsaturated absorption coefficient of about 1200 dB/m at 976 nm. After numerous tests made in order to optimize the fiber length, a 2 m-long Liekki Yb-doped fiber has been chosen as the active medium.

As shown in Fig. 4.7b, the average output power increases significantly when the pump current in the second stage of the pre-amplifier becomes stronger, with a higher slope respect to the previous case. In fact, an output

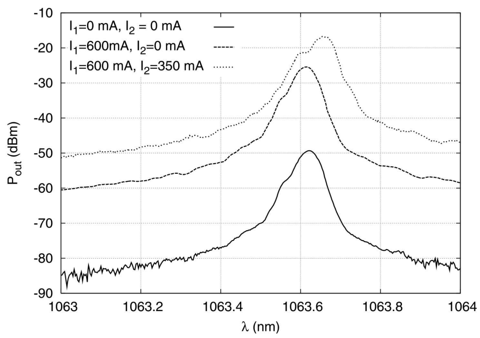

(a)

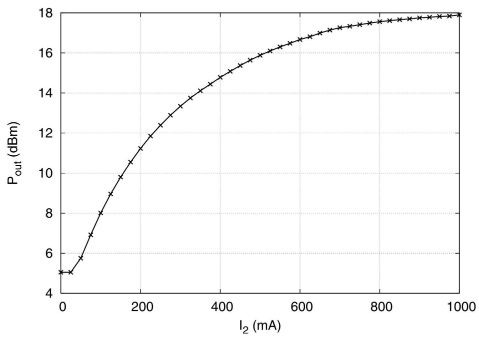

(b)

Figure **4.8**: (a) Backwards propagating light spectra measured with the Liekki single-cladding doped fiber for different pump current configurations. (b) Output power of the two-stage MOPA as a function of the second stage pump current I_2 for the 20 ns pulses with a repetition rate of 20 kHz, when $I_1 =$ 600 mA.

power of 16.7 dBm has been reached when I_2 is only 500 mA. It is important to underline that it is not worth to further increase the pump power in the second stage, due to the strong saturation behaviour, which prevents any gain improvement.

The spectra of the light backward travelling along the pre-amplifier have been measured with the Liekki Yb-doped fiber and reported in Fig. 4.8a for different pump current configurations. By considering the second stage pump turned off, the spectrum does not present any broadening. By increasing the I_2 value, the peak due to the Brillouin scattering appears and becomes higher than the signal one, being about -16.8 dBm when $I_2 = 350\ mA$

4.2.4 Second stage with double-cladding Liekki fiber

For fiber amplifiers capable of high output power operation, the so-called double-cladding fibers can be used [170]. Such fibers usually have a single-mode core in which the signal wave propagates, surrounded by a larger multi-mode undoped inner cladding into which the pump light is launched. The modes of the inner cladding have some overlap with the doped core, so that the pump light can be absorbed there. The main advantages of this kind of

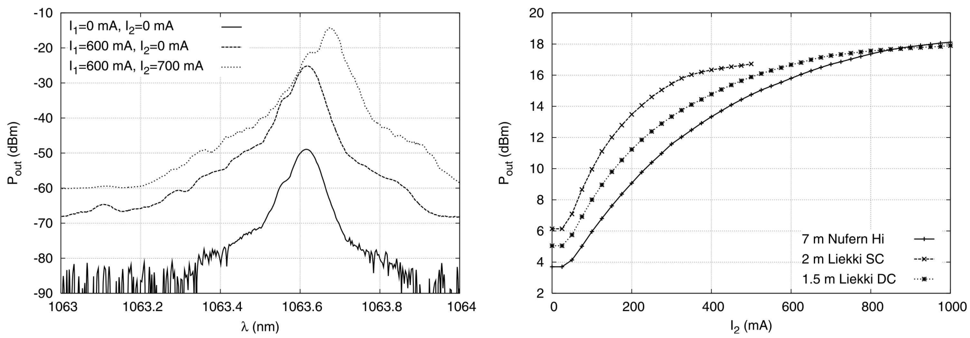

Figure **4.9**: (a) Backward propagating light spectra measured with the double-cladding Liekki fiber for different pump current configurations. (b) Comparison of the output power of the two-stage MOPA obtained with the different Yb-doped fibers as a function of the second stage pump current I_2 for the 20 ns pulses with a repetition rate of 20 kHz, and $I_1 = 600$ mA.

fiber are that higher powers can be coupled into a multi-mode pump core, due to the larger spot size, and the pump source diode does not need to emit a single spatial mode. The pump launch efficiency can be very high and the alignment tolerances relatively uncritical. As a consequence, there are prospects for several watts of output power to be obtained from such devices.

A double-cladding fiber made by Liekki, that is Yb1200-6/125DC, which is characterized by a mode field diameter of 6 μm at 1060 nm, a core and cladding numerical aperture of 0.15 and 0.46, respectively, has been considered in the second stage of the pre-amplifier. Notice that the double-cladding fiber has been used as single-cladding one, since the component for the pump coupling is the same WDM previously described. As a consequence, all the pump power is coupled in the fiber core, whose absorption coefficient at 976 nm is 1200 dB/m as in the single-cladding Yb-doped fiber.

Preliminary results obtained by considering a 1.5 m-long doped-fiber are reported in Fig 4.8b. Looking at the behaviour of the average output power as a function of the pump power in the second stage, it is possible to notice that the saturation is less significant with respect to the single-cladding Liekki fiber case. In fact, the measurements have been done by increasing the pump current up to its maximum value of 1 A, obtaining in this condition a maximum value of 17.9 dBm for the 20 ns pulses with a repetition rate of 20 kHz.

As for the configurations previously considered, the light backward propagating in the amplifier has been monitored. Similarly to the previous single-cladding fiber cases, the spectra shown in Fig. 4.9a demonstrate the presence of the peak due to the Brillouin scattering. In particular, for a 700 mA pump current on the second stage, a significant increase of the Brillouin peak can be noticed. In this condition a peak of -14.2 dBm has been measured at 1063.67 nm, while the power at the signal wavelength is about -21 dBm.

In summary, the MOPA performances obtained by considering the three Yb-doped fibers in the second stage are compared in Fig. 4.9b. Notice that the best performances for the 20 ns pulses with repetition rate of 20 kHz have been obtained with the single-cladding fiber made by Nufern, being the maximum average output power about 18 dBm for $I_2 = 1\ A$. However, it is important to underline that output power values only slightly lower have been measured with both the Liekki fibers, provided that their optimum length is considered.

Chapter 5

Plastic optical fiber sensors

Fiber optic sensors present many advantages with respect to the electronic ones. In fact, they are small and light, immune to electromagnetic interferences, due to their dielectric nature, and they allow remote opto-electronic conversion and processing [135, 171]. These sensors, which can be intrinsic or extrinsic, have a great potential to be exploited in numerous application areas, and they are now commercially available from a number of companies [172].

In this Chapter low cost sensors realized with plastic optical fibers during the PhD activity are presented, which are simple, effective and inexpensive solutions to the problem of the liquid level measurements. All the devices have been realized with a 980/1000 PMMA POF (OC-2134 Luceat), that is with a core and a cladding diameter of 980 and 1000 μm, respectively, which represents the sensing medium. It is important to underline that the sensors here proposed can be used also for applications in food-processing industries.

5.1 Plastic Optical Fibers

Plastic Optical Fibers (POFs) [173], which have been around almost as long as silica ones, have been employed for sensing [174] and a lot of other low cost applications in different fields, such as communications, data transmission, illumination, lighting and imaging [175]. In fact, POFs offer unique properties, which are suitable for industrial applications. For example, light coupling is extremely easy, due to their large core size, usually around 1 mm, and their large NA. Moreover, they can be simply connected to optical devices, like Light Emitting Diodes (LED) or Photodiodes (PD), and can be employed in low cost systems, due to the inexpensive opto-electronic components and low tolerance plastic moulded connectors which can be used [174]. Their main drawback with respect to silica optical fibers is the high attenuation, which is typically 200 dB/km at 650 nm for POFs with a Poly-Methyl-Methacrylate (PMMA) core [174].

Recently, POF-based systems have received more and more attention, becoming a valid alternative in a great number of data and audio applications for rates up to 100 $Mbps$ and distances up to 100 m. In particular, POFs have found interesting applications for lighting and sensing. Besides the same advantages offered by the sensors realized with silica optical fibers, the ones based on POFs provide other properties strictly related to their distinguishing characteristics, like large core dimension, high NA, great flexibility, easy non-skilled handling and low cost [174]. POF-based sensors have been successfully employed to obtain distance, humidity, pressure, refractive index [176], concentration [177], displacement [178] and temperature measurements.

5.2 Liquid level optical fiber sensors

Numerous techniques based on different principles have been proposed in literature in order to measure the liquid level. These sensors are usually classified as intrusive, when it is necessary to dip them into the liquid in order to obtain the measurement, or, otherwise, as non-intrusive. For example, accurate values can be obtained with mechanical float-type level indicating devices, even if some disadvantages are related to the intrusive nature of this technique. In order to avoid the direct contact with the liquid, ultrasonic detectors can be exploited [179], which present, as a drawback, inaccuracy problems due to temperature and density changes. Radar and microwave techniques [180] provide non-intrusive measurements with optimum performances, especially with high dielectric constant liquids. Among the different devices proposed to measure the liquid level, fiber optic sensors have attractive properties [181–187]. In fact, their non-electrical nature make them suitable for chemical liquid explosives or flammable fuels control, as well as for dangerous environments. These sensors, which are usually employed for point measurements [185] or for continuous ones, can be realized with either silica or plastic optical fibers [188–190], which may guarantee even better performances.

Here low cost liquid level sensors realized with POFs are presented, which are simple, effective and inexpensive. The sensors here proposed can be used also for refractive index measurements. In the next Sections the sensor design and the experimental results obtained with the prototype developed have been reported.

5.2.1 Point measurements

An intrusive POF sensor has been developed for point measurements of the liquid level, which is based on the TIR principle [185]. The liquid presence can be detected by evaluating the light back-reflected by a probe, realized with a 0.1 m long 980/1000 POF (OC-2134 Luceat), with a 2.2 mm diameter jacket. The polyethylene jacket has been removed at one fiber end, which has been then tip-shaped with a polish film for POF assembly.

By dipping the POF tip in a liquid with a refractive index higher than the air one, the probe works like a retro-reflecting prism. In order to better understand the sensor operation principle, it is useful to consider the critical angle θ_c, which is defined as

$$\theta_c = \arcsin\left(\frac{n_2}{n_1}\right) , \tag{5.1}$$

where $n_1 = 1.49$ is the PMMA fiber core refractive index and n_2 is the outstanding media one. When the incident angle θ_i of the light rays on the probe

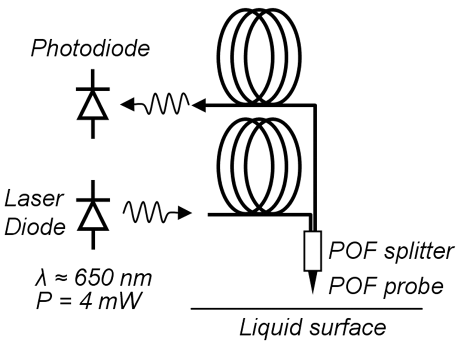

(a)

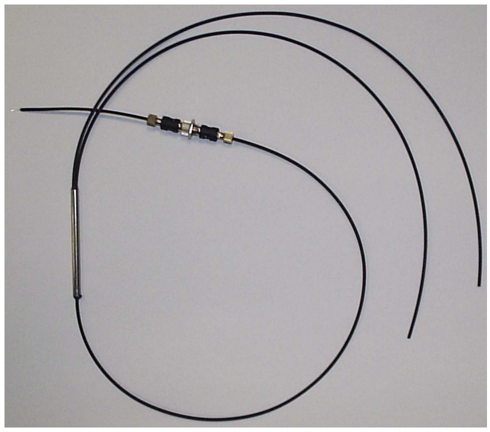

(b)

Figure **5.1**: (a) Schematic of the point level sensor setup. (b) Photo of the probe connected to the POF beam-splitter.

tip is wider than the critical angle, that is $\theta_i > \theta_c$, the TIR condition is satisfied and there is only light reflection. Otherwise, light is both reflected and transmitted. It is important to underline that the back-reflected light intensity decreases when the tip is surrounded by a high refractive index material, since a smaller number of rays satisfies the TIR condition, while the others are diffused in the liquid. A schematic representation of the liquid level sensor designed and realized during the PhD is shown in Fig. 5.1a. The light coming out from the POF probe is sent to an all-POF beam splitter, reported in Fig. 5.1b. Standard POFs have been used to connect the beam-splitter ends to a green-light LED and to a POF PD, respectively. The control electronics for the LED is driven by a simple DC polarization circuit while the PD is connected to a transimpedance amplifier plus a differential one. Notice that the electronic circuit has been properly designed so that the transimpedance amplifier output voltage is equal to the reference voltage when the POF probe is dipped into the liquid. On the contrary, if the sensor probe is in air and the light is mainly back-reflected by the tip, the output of the transimpedance amplifier increases and the one of the differential amplifier saturates high. The sensor output voltage is then processed by a Schmitt trigger, thus resulting in a digital signal.

Measurement results

In order to calculate the extinction ratio of the two realized probes, a power meter has been connected at one end of the POF beam splitter, thus measuring the intensity of the light back-reflected by the probe. The POF tip performances have been investigated by evaluating the extinction ratio E_r according to

$$E_r = -10 \log(P_1/P_2) \ , \tag{5.2}$$

being P_1 and P_2 the output optical power when the POF probe is in air and dipped into the liquid, respectively [182]. Measurement results have shown that the probe extinction ratio is the same whatever is the considered liquid. In particular, 0.38 dB and 1.09 dB have been measured for the 60° and 90° angled fiber tip, respectively. These E_r values are extremely low, but sufficient to detect the liquid presence when using a highly sensitive control electronic. It is important to underline that the proposed all-POF sensor, not requiring any lens or prism, is simple, extremely cheap and robust, and it provides good performances. Due to the plastic nature of the fiber probe, it is suitable to measure the level of flammable liquids. As a drawback, the POF probe can be used in a limited temperature range, that is from -20 to 70°C, and it is necessary to avoid substances, like toluene or methyl-ethyl-ketone, which can etch the fiber.

5.2.2 Continuous measurements

Notice that the POF sensor previously described is suitable only for point measurements. However, a continuous liquid level sensor can be realized by mounting the probe on a motor-controlled arm, or by repeating the whole sensing system N times and by using an electronic multiplexing technique to acquire the N signals. As an alternative solution for continuous liquid level measurements, a non-intrusive POF sensor has been realized too. The solution here proposed is simple, and extremely cheap and robust, even if its measuring range is almost lower than 130 cm.

Fig. 5.2a reports the experimental set-up of the realized liquid level sensor. A POF pair constituted by two standard 980/1000 POFs (OC-2134 Luceat) has been used. A red-light LED with a maximum power of 4 mW at 650 nm is connected to one of the fibers, which transmits the light towards the liquid under test. Notice that the POF pair represents the probe of the proposed sensor. The transmitted light is collimated by a lens with a diameter of 2.15

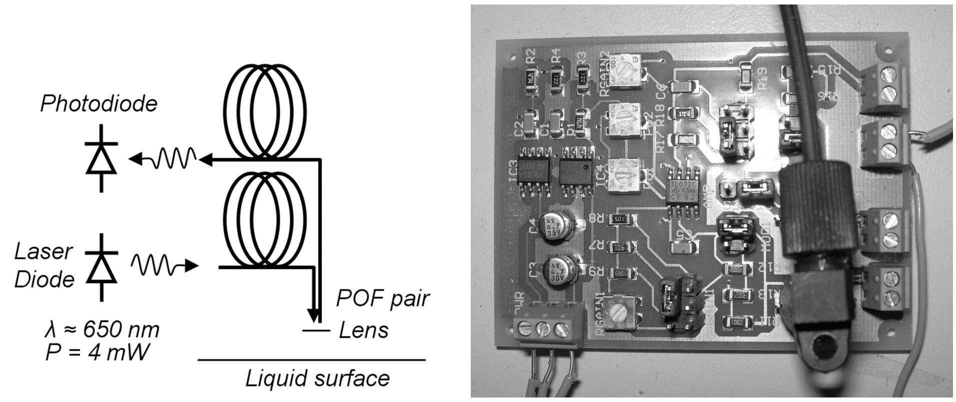

(a) (b)

Figure **5.2**: (a) Schematic of the continuous level sensor setup. (b) Photo of the sensor electronic circuit

cm and a focal distance of 10 cm. Then, the beam reaches the liquid surface and it is reflected back. After the focusing due to the lens, the reflected light is collected by the second POF belonging to the pair and it is transmitted to a PD, where it is converted into an electronic signal. This is amplified through a transimpedance amplifier and sent to a processing electronic circuit whose photo is reported in Fig. 5.2b. The output voltage value, measured with a voltmeter, depends on the distance between the liquid surface and the probe. In fact, the reflection of the light on the surface of the liquid under test can be described by the Fresnel coefficient. In particular, liquids with higher refractive index values presents also higher values of the Fresnel reflection coefficient. As a consequence, their surface can better reflect the incident light, thus causing higher values of the back reflected intensity and of the sensor output voltage.

Level measurements

At first, in order to understand the sensor behaviour, the photodiode current has been initially measured by a source-measurement unit having, in the 100 μA range, an accuracy better than 10 nA. In Fig. 5.3a the photodiode current is reported as a function of the distance of the liquid in the vessel from the collimating lens for different reverse bias voltages. As expected, the photodiode bias voltage slightly affects the sensor sensibility. The maximum

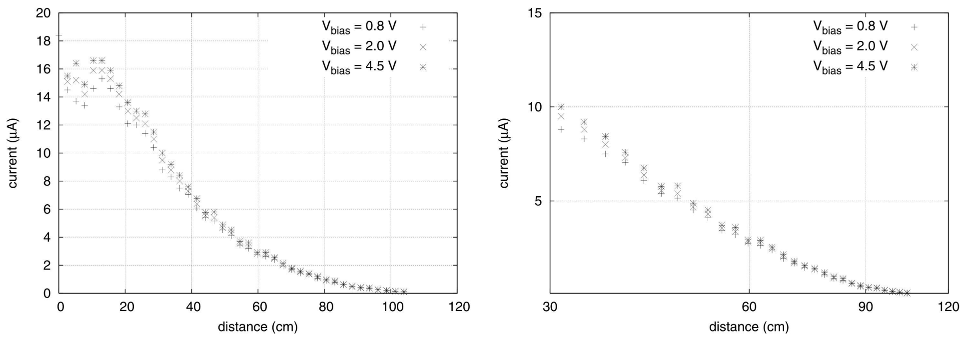

Figure **5.3**: (a) Photodiode current measured at three bias voltages versus the liquid level. (b) Detail of the previous curves for a distance between 30 cm and 120 cm.

distance, in the photoconductive mode, is limited by the maximum power of the emitting LED and by the dark current of the PD which, in this case, is of the order of 100 nA. As represented in Fig. 5.3b, the current values obey the inverse-square law except for the region just below the lens.

After testing the sensor behaviour, the source-measurement unit has been substituted with an electronic circuit, in order to convert the photodiode current into a voltage. The circuit is based on a low-cost JFET-input operational amplifier, with a total input-referred noise of approximately 5 pA and offset compensation. The photodiode bias is maintained at zero Volts by the virtual ground of the operational amplifier.

The performances of the liquid level sensor have been tested by considering six liquids, that is water, milk, fruit juice, olive oil, honey and a solution of 80% sugar in water, which present, for example, different density and transparency. In particular, all these liquids are characterized by different values of the refractive index. In this way it has been possible to investigate how the refractive index of the liquid under test changes the sensor performances. In Fig. 5.4a the measured output voltage is reported as a function of the distance of the liquid under test from the collimating lens. Notice that the maximum distance which can be measured with the proposed sensor is slightly influenced by the kind of liquid considered for the measurements, being in the

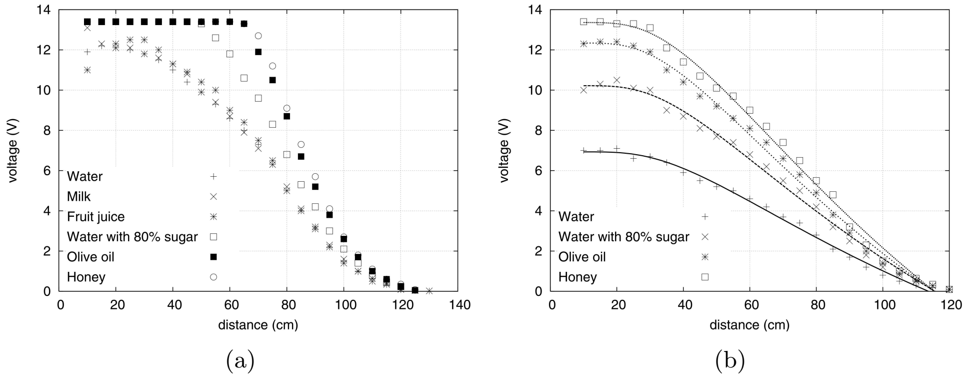

Figure **5.4**: Behaviour of the proposed continuous liquid-level sensor for different liquids with (a) high and (b) low gain of the electronic amplification circuit, in order to prevent saturation.

range between 120 cm and 130 cm for all the considered fluids. In particular, the maximum value of 130 cm has been obtained for water and olive oil, with a corresponding output voltage of 0.012 V and 0.02 V, respectively. As expected, differences in the sensor behaviour have been observed for lower distance values, that is the output voltage measured at a certain separation between the collimating lens and the liquid surface depends on the fluid taken into account.

In particular, the voltage values obtained for milk and fruit juice are similar to the ones reached for water, since the difference between their refractive

Liquid	**a**	**b**	**c**
Water	6.93	0.008794	0.007606
Water with 80% sugar	10.22	0.00864	0.007821
Olive oil	12.34	0.008668	0.008046
Honey	13.36	0.00866	0.007607

Table 5.1: Fitting curves parameters as a function of the different liquids considered.

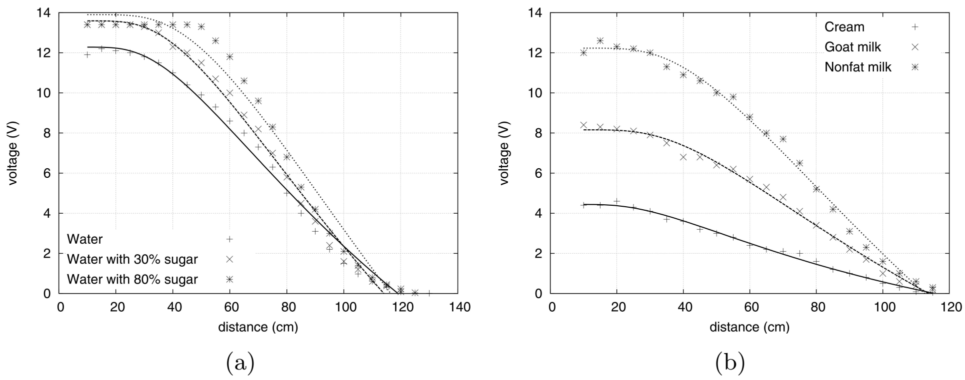

Figure **5.5**: Comparison of the proposed liquid level sensor behaviour for (a) water solutions with different sugar concentrations and (b) different kinds of milk.

indices and the water one, that is 1.33, is quite low. On the contrary, higher output voltage values have been measured for the 80% sugar solution, the olive oil and the honey, which are all characterized by a refractive index higher than 1.49. Also the minimum distance which can be measured with the realized POF-based level sensor is affected in a significant way by the liquid under test. In fact, with the three low-index liquids here considered, a distance of 10 *cm* can be obtained, which corresponds to a voltage of 11.9 V, 13.1 V and 11 V for water, milk and fruit juice, respectively. As a consequence, it is possible to accurately evaluate a lens-liquid separation in a range of about 120 *cm*. This range becomes shorter if the remaining three liquids are considered, that is the ones with higher refractive index. In fact, the output voltage saturates to a value of 13.4 V when the measured distance decreases below 50 *cm* for

Liquid	**Water**	**Water with 80% sugar**	**Olive oil**	**Honey**
$\mathbf{n_l}$	1.33	1.35	1.466	1.494
R	2.04%	2.22%	3.57%	3.92%

Table 5.2: Refractive indices and Fresnel reflection coefficient of the liquids used for the experiments.

the 80% sugar water solution, and 65 cm for olive oil and honey.

In order to enlarge the range of distance values which can be evaluated with the realized sensor, the measurements have been repeated for the three fluids with refractive index higher than 1.49 and for water, as a comparison, with a lower gain in the electronic amplification circuit. As reported in Fig. 5.4b, the voltage saturation is avoided and a minimum distance of 10 cm has been measured for all the liquids under test. Notice that this value corresponds to an output voltage of 7 V when water is considered, with a decrease of 4.1 V with respect to the previous case. As a drawback, the gain decrease in the amplification circuit causes a slight reduction of the maximum measurable distance, which becomes 115 cm for water and 120 cm for all the other high-index fluids here considered.

In order to obtain the best representation of the measured values, each data set in Fig. 5.4b has been fitted to a function of the form

$$f(x) = a \cdot \left(1 - exp\left(-\left(\frac{1}{x} - b\right)/c\right)\right), \tag{5.3}$$

where x is the distance, a is associated to the liquid refractive index, b is a function of sensor noise and c depends on the air attenuation of the light. In Tab. 5.1 the values of a, b, and c are reported as a function of the liquid considered. In particular, the a value for honey is the highest, that is 13.36. As a consequence, the honey surface can better reflect the incident light with respect to the other liquids, thus causing higher values of the back reflected intensity and of the sensor output voltage. On the contrary, b and c values for different liquids do not present a considerable difference, due to their relation with the sensor behaviour and not with the liquid characteristics.

Finally, notice that the range of distance values which can be successfully measured with the continuous liquid level sensor here proposed, that is about 120 cm, can be improved, by employing higher emitting power LEDs or PDs with better performances, as well as by further optimizing the electronic circuits by using a micro-controller for the data acquisition and the system control [189, 190].

5.3 Refractive index measurements

The behaviour of the sensor here proposed is strictly related to the reflection of the light on the surface of the liquid under test, which is described by the

Fresnel coefficient. In case of normal incidence of the beam on the boundary surface between air and the liquid considered for the measurements, the reflection coefficient can be expressed as

$$R = \left(\frac{n_{air} - n_l}{n_{air} + n_l} \right)^2 , \tag{5.4}$$

where n_l is the liquid refractive index, reported in Tab. 5.2 for the liquid of Fig. 5.4b, and $n_{air} = 1$ is the air one. R values for water and milk are almost the same, while the one for olive oil or honey are the highest, that is 3.57% and 3.92%, respectively. The honey surface can thus better reflect the incident light with respect to the other liquids, thus causing higher values of the back reflected intensity and of the sensor output voltage. As a consequence, the difference in the sensor behaviour which has been demonstrated with different liquids can be successfully exploited to identify fluids, according to their refractive index. For example, the sugar presence causes an increase in the water refractive index, which changes from 1.33 to 1.49 as the concentration approaches the 80%. Consequently, a higher voltage at the sensor output is obtained, at a fixed distance, as shown in Fig. 5.5a. The figure also reports an intermediate sugar concentration, that is 30%, corresponding to a water solution with a refractive index of 1.38. The difference between the output voltage obtained with this latter solution and the water reaches a maximum of about 1.6 V around 45 cm, and then decreases for higher distance values. These results confirm that a proper sensor design allows to distinguish solutions with different refractive index, that is, in this case, to evaluate the sugar percentage in water.

Liquid	a	b	c
Water	12.28	0.008402	0.007508
Water with 30% sugar	13.59	0.008767	0.006525
Water with 80% sugar	13.9	0.008587	0.005427
Cream	4.44	0.008645	0.009682
Goat milk	8.157	0.008785	0.006924
Nonfat milk	12.23	0.008882	0.006342

Table 5.3: Fitting curves parameters as a function of different sugar concentrations in water and of different kinds of milk.

In a similar way, different kinds of milk can be discriminated. Fig. 5.5b reports the output voltage values obtained as a function of the distance by considering nonfat milk, goat milk and cream, which are characterized by 0.05 *mg*, 4 *mg* and 35 *mg* of fat in 100 *ml* of fluid, respectively. Notice that, for a fixed distance, the light reflection is better, and consequently the output voltage is higher, when the fat quantity in milk is low. Note that the difference among the output voltage values measured for the three different kinds of milk is higher with respect to the case of the sugar solutions, being about 4 *V* when the distance is 20 *cm* and still around 1 *V* for a lens-liquid separation of 90 *cm*. As a consequence, in this case it is easier to evaluate which liquid presents the lower fat quantity.

Each data set of Fig. 5.5 has been fitted with a function of the form of Eq. (5.3), whose coefficient values are reported in Tab. 5.3.

Conclusions

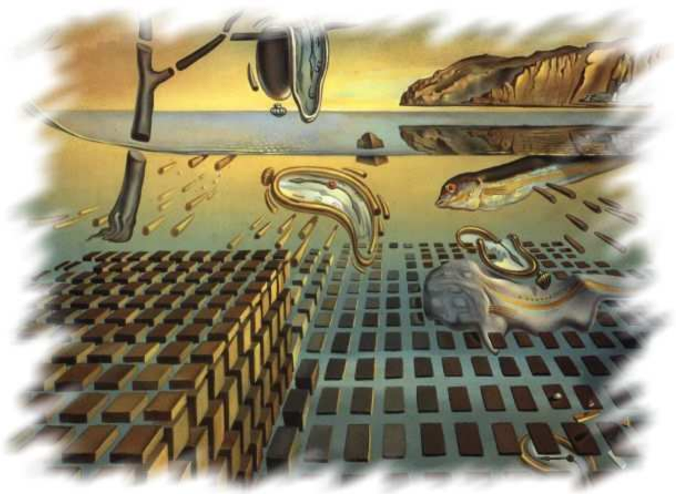

Modern optical fibers are one of the major technological successes of the 20th century, and they have become the most important method of communicating information. This technology has developed at an incredible rate, from the first low-loss ($< 20\ dB/km$) single-mode waveguides in 1970 to being key components of the present sophisticated global telecommunication network. Nowadays optical fibers, which transmit information in the form of short optical pulses over long distances at exceptionally high speeds, have become an integral part of life in the information age. There are non-telecom applications for fibers, too, for example in beam delivery for medicine, machining and diagnostics, sensing and a lot of other fields.

Amazingly, the basic physics of optical fibers has remained unchanged since the 19th century. This, in part, may be a direct result of the fast initial implementation of the fiber optic technology. The system was established early on, and all future developments were incremental improvements to individual components. State-of-the-art optical fibers represent a careful trade-off between optical losses, optical nonlinearity, group-velocity dispersion and polarization effects. Optical losses are inherent in the raw material used to make the fibers, which is usually synthetically produced silica, SiO_2. Other effects, such as nonlinearity and dispersion, are strongly affected by the material properties, but can be significantly influenced by the fiber design. Properties like polarization-mode dispersion result from imperfections in the fabrication processes. After 30 years of intensive research, incremental steps have refined the capabilities of the system and the fabrication technology nearly as far as they can go.

Could current optical fibers become obsolete? It seems an unlikely proposition. However, researchers and engineers are still working hard to develop new optical fibers, which could outperform conventional fibers in many fields, and to exploit the advantages offered by traditional ones for more and more innovative applications. The activity carried out during the PhD course and reported in the present thesis is set in this extremely active research field. In fact, optical fibers with unusual geometric and dielectric properties, like photonic crystal fibers or erbium-doped depressed-cladding fibers, have been thoroughly studied. Moreover, new applications have been proposed for both silica and plastic optical fibers, which can be interesting for different industrial areas.

Photonic crystal fibres (PCFs) rely on the unusual properties of photonic crystals, which present a regular morphological microstructure on the scale of the optical wavelength, radically altering their optical properties, to deliver previously unimaginable performances from an optical waveguide. These new fibers, usually made of silica, are characterized by air-holes in their cross-section, travelling all along their length. By properly designing the position and the dimension of the air-holes, which can be organized in regular lattices or not, PCFs with diametrically opposite properties can be obtained. It has been widely demonstrated that PCFs are superior with respect to conventional optical fibers in several aspects, thus leading to new applications. Since PCFs exploit new mechanisms to guide light and present unusual properties, a whole Chapter, that is the first one, has been dedicated in the present PhD thesis to the description of their characteristics, included their fabrication process.

By exploiting a full-vector modal solver based on the finite element method, the PCF guiding properties have been deeply analyzed, as described in Chapter 2. Interesting results have been obtained by studying, for the first time, PCFs characterized by a square-lattice of air-holes in the transverse section. The comparison with the most common triangular PCFs with the same characteristics, that is the same hole-to-hole spacing and air-hole diameter, has shown the influence of the air-hole lattice geometry on the fiber properties, in particular on the single-mode behaviour. In fact, it has been demonstrated that square-lattice PCFs can be endlessly single-mode in a wider range of the geometric parameter values with respect to triangular ones, and so they can be successfully used in applications which need large mode area fibers. As an alternative for this kind of applications, triangular PCFs with a wide effective area can be obtained by removing the air-holes belonging to the first ring, besides the central one, from the fiber cross-section. The cut-off properties of these large-core fibers, called 7-rod PCFs, have been deeply analyzed, showing that their single-mode region is significantly smaller than that of traditional triangular fibers, especially for the lower air-filling fraction values. However, it has been demonstrated the possibility to find a successful compromise between the achievable effective area and the number of modes that these large mode area triangular PCFs guide over the wavelength range of interest. The accuracy of the guided mode effective area values numerically calculated through the simulations has been checked by comparing the results obtained with the finite element method with those of the experimental measurements made with a Scanning Near-Field Optical Microscope (SNOM) for some samples of large mode area PCFs available in laboratory. Moreover, other experimental measurements have been made to evaluate the spectral broadening of fs pulses of a Ti:Sapphire laser into a short length of a nonlinear highly birefringent PCF made of silicate glass. In the final part of the Chapter the study of the guiding properties of a hollow-core fiber, different from the PCFs previously considered, all characterized by a solid core, has been reported. In particular, air-guiding has been studied in a realistic air-silica hollow-core Bragg fiber. The dispersion curves, the confinement loss spectra and the field distribution of the guided modes have been calculated, showing the significant influence of the silica bridges on the fundamental mode characteristics. Then, it has been deeply investigated how each geometric characteristic in the hollow-core Bragg fiber cross-section influences the fiber guiding properties, showing which parameter it is better to change in order to properly modify the values or the spectral behaviour of the losses. Finally, among the different possible applications, the feasibility of a DNA bio-sensor based on a hollow-core Bragg fiber has been demonstrated.

During the PhD course an interesting activity has concerned a depressed-cladding fiber doped with erbium ions. Fibers with this kind of refractive index profile are usually considered for their particular dispersion properties. On the contrary, in the present research its bending losses have been exploited, for the first time, in order to obtain amplification of signals in an unconventional band with respect to the well-established erbium-doped fiber amplifiers (EDFAs), that is in S band, 1450 $nm \div 1530\ nm$. In fact, through the doped-fiber bending losses the amplified spontaneous emission in the C band can be properly suppressed. Results of the research activity concerning the study of EDFAs for S band in single pass configuration and in double pass one have been summarized in Chapter 3. The amplifier performances have been measured by changing the signal input power, the pump power, the fiber bending diameter and the fiber length. Moreover, by combining in a new parallel scheme a S band amplifier and a C band one, both with a double pass configuration and realized with the same depressed-cladding erbium-doped fiber, bent with two different diameter values, an EDFA for S+C band has been demonstrated. By adding a L band module, a triple band all-silica EDFAs has been developed. In the second part of the Chapter, a tunable narrow-linewidth triple-wavelength EDF Ring Laser (EDFRL) has been experimentally demonstrated, where the bending losses of the depressed-cladding fiber have been exploited to tune the laser wavelength in S, C and L band. This tuning method has been also exploited to shift the wavelength of a single frequency EDFRL in S band and in C band. Finally, a tunable single frequency S band depressed-cladding EDFRL, where the doped fiber has been used as the active medium, as well as the tunable filter, has been proposed and experimentally demonstrated.

Optical fibers doped with another rare-earth element, that is ytterbium, have been considered during the PhD course. This kind of doped-fiber is usually used to develop lasers and amplifiers for high power industrial applications, due to the several unique advantages offered by the ytterbium ions. Since recently high-power fiber lasers and amplifiers have progressively replaced mechanical and electrical tools in many important applications, a significant part of the PhD research activity, discussed in Chapter 4, has concerned the design and the experimental realization of a pre-amplifier, which will be employed in a master oscillator power amplifier for the amplification of pulses at 1064 nm to high power levels. The output power of the two-stage pre-amplifier realized has been measured by considering different ytterbium-doped single-mode fibers, both with a single- and a double-cladding, and by changing the active fiber length and the pump power of single-mode grating-stabilized lasers at 976 nm, in order to optimize the gain performances for 20 ns pulses with a repetition rate of 20 kHz.

Another interesting application of optical fibers which has been considered during the PhD research activity is sensing. In particular, as reported in Chapter 5, plastic optical fibers (POFs) have been used to realize low-cost sensors, which are simple, effective and inexpensive solutions to the problem of the liquid level measurements. Notice that POFs have been chosen instead of silica optical fibers since they offer many important advantages. In fact, light coupling into the POF core is extremely easy, due to the high numerical aperture value and the large core diameter. Moreover, POFs can be exploited to realize low-cost devices, since inexpensive opto-electronic components and low tolerance plastic connectors can be used. An intrusive POF sensor based on the total internal reflection principle has been developed for point measurements of the liquid level. Moreover, a non-intrusive sensor based on a POF pair has been realized for continuous liquid level measurements. It is important to underline that the last sensor can be used also to distinguish different fluids according to their refractive index.

Will optical fibers as they are now known become obsolete? Probably not, but *fantasy* will make them to become just one string in a far more powerful bow.

Appendix A

Finite Element Method

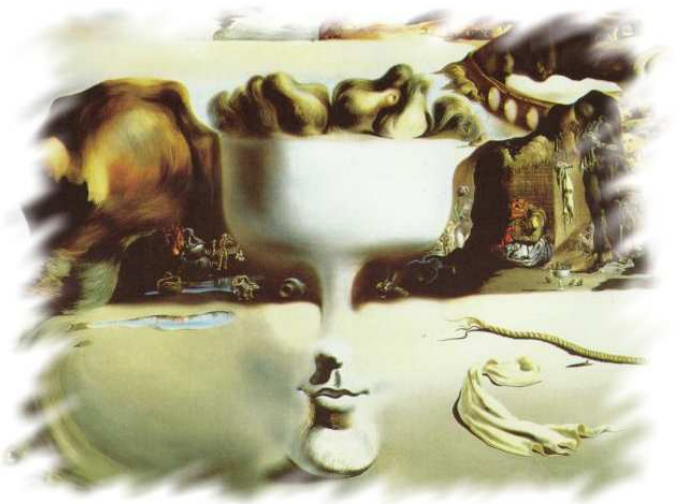

All the analyses of the PCF properties presented in this thesis have been performed by using the Finite Element Method (FEM). The FEM allows the PCF cross-section in the transverse $x-y$ plane to be divided into a patchwork of triangular elements, which can be of different sizes, shapes and refractive indices. In this way any kind of geometry, including PCF holes, as well as medium characteristic, can be accurately described. In particular, the FEM is suited for studying fibers with non-periodic air-hole arrangements. Moreover, it provides a full-vector analysis which is necessary to model PCFs with large air-holes and large index variations, and to accurately predict their properties [191].

The formulation of the FEM here considered is based on the curl-curl equation. For a medium described by the complex tensors of the relative dielectric permittivity $\bar{\bar{\epsilon}}_r$ and the magnetic permeability $\bar{\bar{\mu}}_r$ it reads

$$\overline{\nabla} \times (\bar{\bar{\varepsilon}}_r^{-1} \overline{\nabla} \times \overline{h}) - k_0^2 \bar{\bar{\mu}}_r \overline{h} = 0 \ , \tag{A.1}$$

where $\overline{h}$ is the magnetic field, and $k_0 = 2\pi/\lambda$ is the wave number in the vacuum, λ being the wavelength.

The magnetic field of the modal solution is expressed as $\overline{h} = \overline{H} e^{-\gamma z}$, where $\overline{H}$ is the field distribution on the transverse plane and

$$\gamma = \alpha + j k_0 n_{eff} \tag{A.2}$$

is the complex propagation constant, with α the attenuation constant and n_{eff} the effective index.

By applying the variational finite element procedure, Eq. (A.1) yields the algebraic problem [192]

$$([A] - (\frac{\gamma}{k_0})^2 [B])\{H\} = 0 \ , \tag{A.3}$$

where the eigenvector $\{H\}$ is the discretized magnetic field vector distribution of the mode. The matrices $[A]$ and $[B]$ are sparse and symmetric, thus allowing an efficient resolution of Eq. (A.3) by means of high performance algebraic solvers.

In order to enclose the computational domain without affecting the numerical solution, anisotropic Perfectly Matched Layers (PML) are placed before the outer boundary [45, 193]. This formulation is able to deal with anisotropic material both in terms of dielectric permittivity and magnetic permeability, allowing anisotropic PML to be directly implemented.

The FEM has allowed the successful investigation of PCF dispersion [194–197], amplification [66, 198] and nonlinear properties [199–201]. Moreover, the complex FEM formulation has been very useful, for instance, to evaluate the PCF leakage or confinement losses, due to the finite number of air-hole rings in the cladding lattice [45, 47].

Moreover, the high flexibility of the method results in solutions whose accuracy has been thoroughly checked, either considering different FEM formulations or through comparisons with different numerical approaches [202, 203].

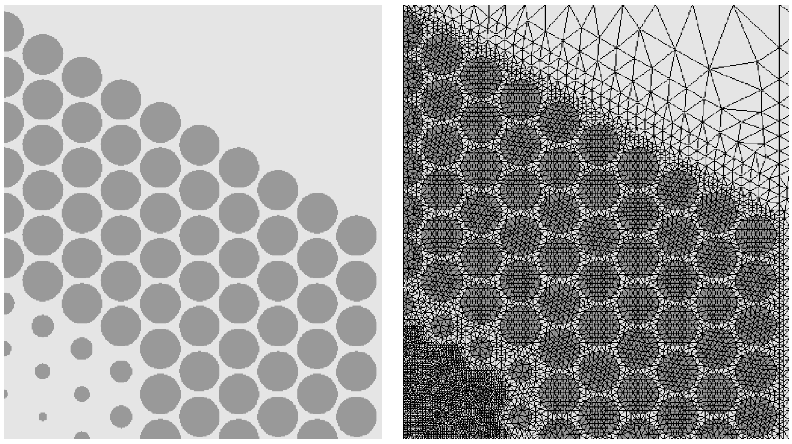

(a) (b)

Figure **A.1**: (a) Geometry and (b) mesh of a quarter of the cross-section of a PCF with enlarging air-holes used for the FEM simulations.

Furthermore, fiber symmetry can be used to reduce the computational domain and, consequently, both time and memory required, without affecting the accuracy of the computed solution.

As an example, a PCF cross-section quarter and the corresponding mesh used for the simulations are reported in Fig. A.1a and b, respectively. Notice that, by properly changing the dimension of the triangular elements which constitute the mesh, it is possible to accurately describe all the regions with different geometric and dielectric properties in the fiber transverse section. In particular, as shown in Fig. A.1b, the silica core region, where the guided-mode field is mainly confined, and the small air-holes belonging to the first three rings are described with a lot of triangles of reduced dimensions. The fundamental component of the guided mode at 1550 nm of the PCF shown in Fig. A.1, which has been calculated with the FEM-based full-vector modal solver, is reported in Fig. A.2.

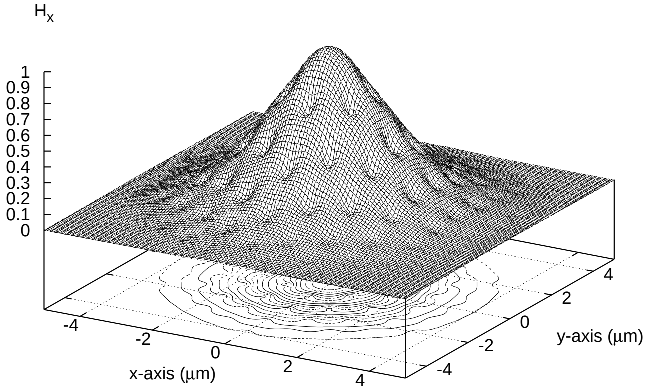

Figure **A.2**: Fundamental component of the magnetic field at 1550 nm evaluated with the FEM-based full-vector modal solver.

Dispersion properties

Starting from the knowledge of the effective refractive index n_{eff} versus the wavelength obtained with the FEM approach [197], the dispersion parameter

$$D(\lambda) = -\frac{\lambda}{c}\frac{d^2 n_{eff}}{d\lambda^2} \tag{A.4}$$

can be derived using simple finite difference formulas. The chromatic dispersion of silica is taken into account through the Sellmeier equation [164], so the refractive index of the structure is changed, according to the working wavelength, before using the FEM solver to get the modal field and n_{eff}, as in Eq. (A.2).

In an optical fiber with high birefringence the effective index of the guided mode is different for the two orthogonal polarizations. As a consequence, a dispersion curve for each polarization can be calculated. Starting from the two dispersion curves, it is possible to calculate the modal birefringence B defined as

$$B = \frac{|\beta_x - \beta_y|}{k_0} = |n_x - n_y| \ , \tag{A.5}$$

where n_x e n_y are the effective indices of the guided mode of the two polarizations. It is possible to demonstrate that, for a given B value, there is a power exchange between the two guided modes which are propagating along the fiber. This happens periodically after a length L_B, evaluated as

$$L_B = \frac{2\pi}{|\beta_x - \beta_y|} = \frac{\lambda}{B} \ . \tag{A.6}$$

Nonlinear properties

The FEM can be exploited to evaluate the guided-mode field distribution in PCFs, necessary to compute the effective area and the nonlinear coefficient.

In order to accurately evaluate the effective area and, consequently, to compute the nonlinear coefficient, the fundamental mode intensity distribution is calculated from the Poynting vector definition, which involves the three components of both the electric and the magnetic fields of the guided mode, obtained with the FEM vectorial modal solver [66].

First, the magnetic field $\overline{H} = (H_x, H_y, H_z)$ on the fiber cross-section is calculated and then, from the expression of $\overline{H}$, the electric field $\overline{E} = (E_x, E_y, E_z)$ is obtained through the Maxwell equation.

Hence, from the definition of the Poynting vector, the normalized intensity is given by

$$i(x,y) = \frac{1}{P}\mathcal{R}e\left[\frac{\overline{E}\times\overline{H}^*}{2}\cdot\hat{z}\right] \ , \tag{A.7}$$

where P is the integral of the intensity over the section of the PCF, that is

$$\begin{aligned} P &= \iint_S \mathcal{R}e\left[\frac{\overline{E}\times\overline{H}^*}{2}\cdot\hat{z}\right] dx\,dy = \\ &= \iint_S \mathcal{R}e\left[\frac{E_x\,H_y^* - E_y^* H_x}{2}\right] dx\,dy \ . \end{aligned} \tag{A.8}$$

Then, the effective area of the PCF fundamental guided mode can be calculated according to

$$A_{eff} = \frac{1}{\iint_S i^2(x,y)dxdy} \ , \tag{A.9}$$

where $i(x,y)$ is the guided-mode normalized intensity distribution, as in Eq. (A.7) [66].

As a consequence, the nonlinear coefficient can be evaluated as

$$\gamma = (2\pi/\lambda) \cdot \iint_S n_2(x,y) i^2(x,y) dx dy \ , \tag{A.10}$$

where $n_2(x,y)$ is $3 \cdot 10^{-20}$ m^2/W in the silica bulk and 0 in the air-holes, and $i(x,y)$ is the normalized intensity, according Eq. (A.7) [66].

Confinement losses

In a PCF with an infinite number of air-holes in the photonic crystal cladding, the propagation is theoretically loss-less. However, in the fabricated fibers the number of air-holes is finite, so the guided modes are leaky.

The Confinement Loss (CL) of the mode is deduced from the attenuation constant α in Eq. (A.2) as

$$CL = 20\alpha \log_{10} e = 8.686\alpha \quad (dB/m) \ . \tag{A.11}$$

Acknowledgements

And now that it is finished, let's go back to italian...

Il corso di dottorato appena terminato ha rappresentato per me un'opportunità importante per fare un significativo passo avanti non solo nel mio percorso professionale, ma anche nella mia crescita personale.
È venuto il momento di ringraziare le persone che hanno condiviso con me questa esperienza.......

Thank
you

Bibliography

[1] J. C. Knight, "Photonic crystal fibres," *Nature*, vol. 424, pp. 847–851, Aug. 2003.

[2] P. St. J. Russell and R. Dettmer, "A neat idea [photonic crystal fibre]," *IEE Review*, vol. 47, pp. 19–23, Sept. 2001.

[3] S. G. Johnson. (2005) Photonic Crystals: Principles, Techniques, and Applications. Tutorial for a Photonic Crystal Workshop sponsored by the IEEE Laser and Electro-Optics Society. [Online]. Available: http://ab-initio.mit.edu/photons/tutorial/leos-course.pdf

[4] K. P. Hansen and R. E. Kristiansen, "Supercontinuum Generation in Photonic Crystal Fibers," Crystal Fibre A/S, Tech. Rep., 2005.

[5] A. Bjarklev, "Photonic Crystal Fibers and their Applications," in *Proc. European Conference on Optical Communication ECOC 2003*, Rimini, Italy, Sept. 21–25, 2003, paper We3.3.

[6] P. St. J. Russell, "Photonic Crystal Fibers," *Science*, vol. 299, pp. 358–362, Jan. 2003.

[7] B. T. Kuhlmey, R. C. McPhedran, C. M. de Sterke, P. A. Robinson, G. Renversez, and D. Maystre, "Microstructured optical fibers: where's the edge?" *Optics Express*, vol. 10, pp. 1285–1290, Nov. 2002. [Online]. Available: http://www.opticsexpress.org/abstract.cfm?URI=OPEX-10-22-1285

[8] N. A. Mortensen, J. R. Folkenberg, M. D. Nielsen, and K. P. Hansen, "Modal cutoff and the V parameter in photonic crystal fibers," *Optics Letters*, vol. 28, pp. 1879–1881, Oct. 2003.

[9] J. C. Knight, J. Broeng, T. A. Birks, and P. St. J. Russell, "Photonic Band Gap Guidance in Optical Fibers," *Science*, vol. 282, pp. 1476–1478, Nov. 1998.

[10] Nonlinear photonic crystal fibers - Crystal Fibre A/S. [Online]. Available: http://www.crystal-fibre.com/products/nonlinear.shtm

[11] W. H. Reeves, J. C. Knight, P. St. J. Russell, and P. J. Roberts, "Demonstration of ultra-flattened dispersion in photonic crystal fibers," *Optics Express*, vol. 10, pp. 609–613, July 2002. [Online]. Available: http://www.opticsexpress.org/abstract.cfm?URI=OPEX-10-14-609

[12] R. E. Kristiansen, K. P. Hansen, J. Broeng, P. M. W. Skovgaard, M. D. Nielsen, A. Petersson, T. P. Hansen, B. Mangan, C. Jakobsen, and H. R. Simonsen, "Microstructured fibers and their applications," in *Proc. Reuniòn Española de Optoelectrònica OPTOEL 2005*, Elche, Spain, July 13–15, 2005.

[13] J. Limpert, N. Deguil-Robin, I. Manek-Hönninger, F. Salin, F. Röser, A. Liem, T. Schreiber, S. Nolte, H. Zellmer, A. Tünnermann, J. Broeng, A. Petersson, and C. Jakobsen, "High power rod-type photonic crystal fiber laser," *Optics Express*, vol. 13, pp. 1055–1058, Feb. 2005. [Online]. Available: http://www.opticsexpress.org/abstract.cfm?URI=OPEX-13-4-1055

[14] D. G. Ouzounov, F. R. Ahmad, D. Müller, N. Venkataraman, M. T. Gallagher, M. G. Thomas, J. Silcox, K. W. Koch, and A. L. Gaeta, "Generation of Megawatt Optical Solitons in Hollow-Core Photonic Band-Gap Fibers," *Science*, vol. 301, pp. 1702–1704, Sept. 2003.

[15] C. J. S. de Matos, J. R. Taylor, T. P. Hansen, K. P. Hansen, and J. Broeng, "All-fiber chirped pulse amplification using highly-dispersive air-core photonic bandgap fiber," *Optics Express*, vol. 11, pp. 2832–2837, Nov. 2003. [Online]. Available: http://www.opticsexpress.org/abstract.cfm?URI=OPEX-11-22-2832

[16] J. Limpert, T. Schreiber, S. Nolte, H. Zellmer, and A. Tünnermann, "All fiber chirped-pulse amplification system based on compression in air-guiding photonic bandgap fiber," *Optics Express*, vol. 11, pp. 3332–3337, Dec. 2003. [Online]. Available: http://www.opticsexpress.org/abstract.cfm?URI=OPEX-11-24-3332

[17] C. J. S. de Matos and J. R. Taylor, “Chirped pulse Raman amplification with compression in air-core photonic bandgap fiber,” *Optics Express*, vol. 13, pp. 2828–2834, Apr. 2005. [Online]. Available: http://www.opticsexpress.org/abstract.cfm?URI=OPEX-13-8-2828

[18] F. Benabid, J. C. Knight, G. Antonopoulos, and P. St. J. Russell, “Stimulated Raman scattering in hydrogen-filled hollow-core photonic crystal fiber,” *Science*, vol. 298, pp. 399–402, Oct. 2002.

[19] F. Benabid, J. C. Knight, and P. St. J. Russell, “Particle levitation and guidance in hollow-core photonic crystal fiber,” *Optics Express*, vol. 10, pp. 1195–1203, Oct. 2002. [Online]. Available: http://www.opticsexpress.org/abstract.cfm?URI=OPEX-10-21-1195

[20] K. Kurokawa, K. Tajima, K. Tsujikawa, and K. Nakajima, “Reducing the Losses in Photonic Crystal Fibres,” in *Proc. European Conference on Optical Communication ECOC 2005*, Glasgow, Scotland, Sept. 25–29, 2005.

[21] B. J. Mangan, L. Farr, A. Langford, P. J. Roberts, D. P. Williams, F. Couny, M. Lawman, M. Mason, S. Coupland, R. Flea, H. Sabert, T. A. Birks, J. C. Knight, and P. St. J. Russell, “Low loss (1.7 dB/km) hollow core photonic bandgap fiber,” in *Proc. Optical Fiber Communications Conference OFC 2004*, Anaheim, California, USA, 2004, paper PDP24.

[22] P. J. Bennett, T. M. Monro, and D. J. Richardson, “Toward practical holey fiber technology: fabrication, splicing, modeling, and characterization,” *Optics Letters*, vol. 24, pp. 1203–1205, Sept. 1999.

[23] K. Tajima, K. Nakajima, K. Kurokawa, N. Yoshizawa, and M. Ohashi, “Low-loss photonic crystal fibers,” in *Proc. Optical Fiber Communications Conference OFC 2002*, Anaheim, California, USA, 2002, pp. 523–524.

[24] L. Farr, J. C. Knight, B. J. Mangan, and P. J. Roberts, “Low loss photonic crystal fiber,” in *Proc. European Conference on Optical Communication ECOC 2002*, Copenhagen, Denmark, Sept. 8 –12, 2002, paper PD1.3.

[25] K. Tajima, J. Zhou, K. Nakajima, and K. Sato, “Ultra low loss and long length photonic crystal fiber,” in *Proc. Optical Fiber Communications*

Conference OFC 2003, Atlanta, Georgia, USA, Mar. 23–28, 2003, pp. PD1–1–PD1–3.

[26] K. Tajima, J. Zhou, K. Kurokawa, and K. Nakajima, "Low water peak photonic crystal fibers," in *Proc. European Conference on Optical Communication ECOC 2003*, Rimini, Italy, Sept. 21–25, 2003, paper Th4.1.6.

[27] K. Kurokawa, K. Tajima, J. Zhou, K. Nakajima, T. Matsui, and L. Sankawa, "Penalty-free dispersion-managed soliton transmission over 100 *km* low loss PCF," in *Proc. Optical Fiber Communications Conference OFC 2005*, Anaheim, California, USA, Mar. 6–11, 2005.

[28] G. Vienne, Y. Xu, C. Jakobsen, H. J. Deyerl, T. P. Hansen, B. H. Larsen, J. B. Jensen, T. Sørensen, M. Terrel, Y. Huang, R. K. Lee, N. A. Mortensen, J. Broeng, H. Simonsen, A. Bjarklev, and A. Yariv, "First demonstration of air-silica Bragg fiber," in *Proc. Optical Fiber Communications Conference OFC 2004*, Anaheim, California, USA, 2004, paper PDP25.

[29] G. Vienne, Y. Xu, C. Jakobsen, H. J. Deyerl, J. B. Jensen, T. Sørensen, T. P. Hansen, Y. Huang, M. Terrel, R. K. Lee, N. A. Mortensen, J. Broeng, H. Simonsen, A. Bjarklev, and A. Yariv, "Ultra-large bandwidth hollow-core guiding in all-silica Bragg fibers with nano-support," *Optics Express*, vol. 12, pp. 3500–3508, July 2004. [Online]. Available: http://www.opticsinfobase.org/abstract.cfm?URI=oe-12-15-3500

[30] J. C. Knight, "Optical fibres using microstructured optical materials," in *Proc. European Conference on Optical Communication ECOC 2005*, Glasgow, Scotland, Sept. 25–29, 2005, paper We3.1.

[31] P. Yeh, A. Yariv, and E. Marom, "Theory of Bragg fiber," *Journal of Optical Society of America*, vol. 68, pp. 1196–1201, Sept. 1978.

[32] J. A. West, C. M. Smith, N. F. Borrelli, D. C. Allan, and K. W. Koch, "Surface modes in air-core photonic band-gap fibers," *Optics Express*, vol. 12, pp. 1485–1496, Apr. 2004. [Online]. Available: http://www.opticsinfobase.org/abstract.cfm?URI=oe-12-8-1485

[33] Technology and Fabrication - Crystal Fibre A/S. [Online]. Available: http://www.crystal-fibre.com

[34] P. St. J. Russell, "Photonic Crystal Fibres," in *Proc. Summer-School on Advanced Glass-Based Nano-Photonics POWAG 2004*, Bath, United Kingdom, July 12–16, 2004.

[35] A. H. Bouk, A. Cucinotta, F. Poli, and S. Selleri, "Dispersion properties of square-lattice photonic crystal fibers," *Optics Express*, vol. 12, pp. 941–946, Mar. 2004. [Online]. Available: http://www.opticsexpress.org/abstract.cfm?URI=OPEX-12-5-941

[36] F. Poli, M. Foroni, M. Bottacini, M. Fuochi, N. Burani, L. Rosa, A. Cucinotta, and S. Selleri, "Single-mode regime of square-lattice photonic crystal fibers," *Journal of Optical Society of America A*, vol. 22, pp. 1655–1661, Aug. 2005.

[37] F. Poli, M. Bottacini, M. Foroni, N. Burani, M. Fuochi, L. Rosa, A. Cucinotta, and S. Selleri, "Analisi del regime di monomodalità per fibre a cristallo fotonico con reticolo quadrato," in *Proc. FOTONICA 2005*, Trani, Italy, May 30 - 1 June 2005.

[38] M. Foroni, F. Poli, L. Rosa, A. Cucinotta, and S. Selleri, "Cut-off properties of large-mode-area photonic crystal fibers," in *Proc. IEEE/LEOS Workshop on Fibres and Optical Passive Components WFOPC 2005*, Palermo, Italy, June 22–24, 2005.

[39] S. Selleri, A. Cucinotta, M. Foroni, F. Poli, and M. Bottacini, "New design of single-mode large-mode-area photonic crystal fibers," in *Proc. International Congress on Optics and Optoelectronics SPIE-COO 2005*, Warsaw, Poland, Aug. 28 - 2 Sept. 2005.

[40] P. St. J. Russell, E. Marin, A. Díez, S. Guenneau, and A. B. Movchan, "Sonic band gaps in PCF preforms: enhancing the interaction of sound and light," *Optics Express*, vol. 11, pp. 2555–2560, Oct. 2003. [Online]. Available: http://www.opticsexpress.org/abstract.cfm?URI=OPEX-11-20-2555

[41] M. G. Franczyk, J. C. Knight, T. A. Birks, P. St. J. Russell, and A. Ferrando, "Birefringent photonic crystal fiber with square lattice," in *Light-guides and their Applications II*, J. Wojcik and W. Wojcik, Eds. Proc. SPIE, 2004, vol. 5576, pp. 25–28.

[42] Y. C. Liu and Y. Lai, "Optical birefringence and polarization dependent loss of square- and rectangular-lattice holey fibers with elliptical air holes: numerical analysis," *Optics Express*, vol. 13, pp. 225–235, Jan. 2005. [Online]. Available: http://www.opticsexpress.org/abstract.cfm?URI=OPEX-13-1-225

[43] J. C. Knight, T. A. Birks, P. St. J. Russell, and D. M. Atkin, "All-silica single-mode optical fiber with photonic crystal cladding," *Optics Letters*, vol. 21, pp. 1547–1549, Oct. 1996.

[44] T. A. Birks, J. C. Knight, and P. St. J. Russell, "Endlessly single-mode photonic crystal fiber," *Optics Letters*, vol. 22, pp. 961–963, July 1997.

[45] D. Ferrarini, L. Vincetti, M. Zoboli, A. Cucinotta, and S. Selleri, "Leakage properties of photonic crystal fibers," *Optics Express*, vol. 10, pp. 1314–1319, Nov. 2002. [Online]. Available: http://www.opticsexpress.org/abstract.cfm?URI=OPEX-10-23-1314

[46] B. Kuhlmey, G. Renversez, and D. Maystre, "Chromatic dispersion and losses of microstructured optical fibers," *Applied Optics*, vol. 42, pp. 634–639, Feb. 2003.

[47] L. Vincetti, "Confinement Losses in Honeycomb Fibers," *IEEE Photonics Technology Letters*, vol. 16, pp. 2048–2050, Sept. 2004.

[48] B. T. Kuhlmey, R. C. McPhedran, and C. M. de Sterke, "Modal cutoff in microstructured optical fibers,," *Optics Letters*, vol. 27, pp. 1684–1686, Oct. 2002.

[49] N. A. Mortensen, "Effective area of photonic crystal fiber," *Optics Express*, vol. 10, pp. 341–348, Apr. 2002. [Online]. Available: http://www.opticsexpress.org/abstract.cfm?URI=OPEX-10-7-341

[50] T. P. White, B. T. Kuhlmey, R. C. McPhedran, D. Maystre, G. Renversez, C. M. de Sterke, and L. Botten, "Multipole method for microstructured optical fibers I. Formulation," *Journal of Optical Society of America B*, vol. 19, pp. 2322–2330, Oct. 2002.

[51] ——, "Multipole method for microstructured optical fibers II. Implementation and results," *Journal of Optical Society of America B*, vol. 19, pp. 2331–2340, Oct. 2002.

[52] T. A. Birks, D. Mogilevstev, J. C. Knight, P. St. J. Russell, J. Broeng, P. J. Roberts, J. A. West, D. J. Allan, and J. C. Fajardo, "The analogy between photonic crystal fibres and step index fibres," in *Proc. Optical Fiber Communications Conference OFC 1999*, 1999, paper FG4-1.

[53] F. Brechet, J. Marcou, D. Pagnoux, and P. Roy, "Complete analysis of the characteristics of propagation into photonic crystal fibers, by the finite element method," *Optical Fiber Technology*, vol. 6, pp. 181–191, Apr. 2000.

[54] M. Koshiba, "Full-vector analysis of photonic crystal fibers using the finite element method," *IEICE Transactions on Electronics*, vol. E85-C, pp. 881–888, 2002.

[55] M. Koshiba and K. Saitoh, "Applicability of classical optical fiber theories to holey fibers," *Optics Letters*, vol. 29, pp. 1739–1741, Aug. 2004.

[56] M. D. Nielsen and N. A. Mortensen, "Photonic crystal fiber design based on the V-parameter," *Optics Express*, vol. 11, pp. 2762–2767, Oct. 2003. [Online]. Available: http://www.opticsexpress.org/abstract.cfm?URI=OPEX-11-21-2762

[57] S. G. Johnson and J. D. Joannopoulos, "Block-iterative frequency-domain methods for Maxwell's equations in a planewave basis," *Optics Express*, vol. 8, pp. 173–179, Jan. 2001. [Online]. Available: http://www.opticsexpress.org/abstract.cfm?URI=OPEX-8-3-173

[58] A. Ferrando, E. Silvestre, J. J. Miret, and P. Andrés, "Full-vector analysis of a realistic photonic crystal fiber," *Journal of Optical Society of America A*, vol. 17, pp. 1333–1340, July 2000.

[59] J. C. Baggett, T. M. Monro, K. Furusawa, and D. J. Richardson, "Comparative study of large-mode holey and conventional fibers," *Optics Letters*, vol. 26, pp. 1045–1047, July 2001.

[60] N. A. Mortensen, M. D. Nielsen, J. R. Folkenberg, A. Petersson, and H. Simonsen, "Improved large-mode-area endlessly single-mode photonic crystal fibers," *Optics Letters*, vol. 28, pp. 393–395, Mar. 2003.

[61] M. Nielsen, N. A. Mortensen, J. Folkenberg, A. Petersson, and A. Bjarklev, "Improved All-Silica Endlessly Single-Mode Photonic Crystal Fiber," in *Proc. Optical Fiber Communications Conference OFC 2003*, Atlanta, Georgia, USA, Mar. 23–28, 2003.

[62] B. Vohnsen and S. I. Boshevolnyi, "Characterization of near field optical probes," *Applied Optics*, vol. 38, pp. 1792–1797, Mar. 1999.

[63] P. Hoffmann, B. Dutoit, and R. P. Salathé, "Comparison of mechanically drawn and protection layer chemically etched optical fiber tip," *Ultramicroscopy*, vol. 61, pp. 165–170, Dec. 1995.

[64] R. Micheletto, N. Yoshimatsu, and S. Okazaki, "A simple method for the fabrication of low cost scanning near field optical microscope probes with acrylic paint as coating element," *Optics Communications*, vol. 188, pp. 11–15, Feb. 2001.

[65] K. Karrai and R. D. Grober, "Piezo-electric tip-sample distance control for near-field optical microscope," *Applied Physics Letters*, vol. 66, pp. 1842–1844, Apr. 1995.

[66] A. Cucinotta, F. Poli, S. Selleri, L. Vincetti, and M. Zoboli, "Amplification Properties of Er^{3+}-doped Photonic Crystal Fibers," *IEEE/OSA Journal of Lightwave Technology*, vol. 21, pp. 782–788, Mar. 2003.

[67] M. Foroni, M. Bottacini, F. Poli, S. Selleri, and A. Cucinotta, "Scanning Near-Field Optical Microscope for characterization of Single Mode Fibers," in *Proc. Optical Fibre Sensors Conference OFS-17*, Bruges, Belgium, May 23–27, 2005.

[68] ——, "Effective area measurement of photonic crystal fibers through Scanning Near-Field Optical Microscope," in *Proc. ICONIC 2005*, Barcelona, Spain, June 8–10, 2005.

[69] M. Foroni, F. Poli, M. Bottacini, A. Cucinotta, and S. Selleri, "Misura di area efficace in fibre a cristallo fotonico mediante tecnica SNOM," in *Proc. FOTONICA 2005*, Trani, Italy, May 30 - 1 June 2005.

[70] W. Belardi, J. H. Lee, K. Furusawa, A. Yusoff, P. Petropoulos, M. Ibsen, T. M. Monro, and D. J. Richardson, "A 10 $Gbit/s$ tunable wavelength converter based on four-wave-mixing in higly nonlinear holey fiber,"

in *Proc. European Conference on Optical Communication ECOC 2002*, Copenhagen, Denmark, Sept. 8 –12, 2002, paper PD 1.2.

[71] R. Tang, J. Lasri, P. Devgan, J. E. Sharping, and P. Kumar, "Microstructure-fibre-based optical parametric amplifier with gain slope of $\simeq$200 $dB/W/km$ in the telecom range," *Electronics Letters*, vol. 39, pp. 195–196, Jan. 2003.

[72] J. K. Ranka, R. S. Windeler, and A. J. Stentz, "Visible continuum generation in air silica microstructure optical fibers with anomalous dispersion at 800 nm," *Optics Letters*, vol. 25, pp. 25–27, Jan. 2000.

[73] A. Ortigosa-Blanch, J. C. Knight, W. J. Wadsworth, J. Arriaga, B. J. Mangan, T. A. Birks, and P. St. J. Russell, "Highly birefringent photonic crystal fiber," *Optics Letters*, vol. 25, pp. 1325–1327, Sept. 2000.

[74] M. Lehtonen, G. Genty, H. Ludvigsen, and M. Kaivola, "Supercontinuum generation in a highly birefringent microstructured fiber," *Applied Physics Letters*, vol. 82, pp. 2197–2199, Apr. 2003.

[75] Z. Zhu and T. G. Brown, "Polarization properties of supercontinuum spectra generated in birefringent photonic crystal fibers," *Journal of Optical Society of America B*, vol. 21, pp. 249–257, Feb. 2004.

[76] A. V. Husakou and J. Herrmann, "Supercontinuum generation in photonic crystal fibers made from highly nonlinear glasses," *Applied Physics B*, vol. 77, pp. 227–234, Sept. 2003.

[77] D. Pysz, R. Stepien, P. Szarniak, R. Buczynski, and T. Szoplik, "Comparing characteristics and prospects of fabrication of multicomponent photonic crystal fibres with different lattice structures," in *Lightguides and their Applications II*, J. Wojcik and W. Wojcik, Eds. Proc. SPIE, 2004, vol. 5576, pp. 78–84.

[78] P. St. J. Russell, "Photonic-Crystal Fibers," *IEEE/OSA Journal of Lightwave Technology*, vol. 24, pp. 4729–4749, Dec. 2006.

[79] R. F. Cregan, B. J. Mangan, J. C. Knight, T. A. Birks, P. St. J. Russell, P. J. Roberts, and D. C. Allan, "Single-mode photonic bandgap guidance of light in air," *Science*, vol. 285, pp. 1537–1539, Sept. 1999.

[80] B. Temelkuran, S. D. Hart, G. Benoit, J. D. Joannopoulos, and Y. Fink, "Wavelength-scalable hollow optical fibres with large photonic bandgaps for CO_2 laser transmission," *Nature*, vol. 420, pp. 650–653, Dec. 2002.

[81] J. Shephard, J. Jones, D. Hand, G. Bouwmans, J. C. Knight, P. St. J. Russell, and B. J. Mangan, "High energy nanosecond laser pulses delivered single-mode through hollow-core PBG fiber," *Optics Express*, vol. 12, pp. 717–723, Feb. 2004. [Online]. Available: http://www.opticsinfobase.org/abstract.cfm?URI=oe-12-4-717

[82] T. Ritari, J. Tuominen, H. Ludvigsen, J. Petersen, T. Sørensen, T. Hansen, and H. Simonsen, "Gas sensing using air-guiding photonic bandgap fibers," *Optics Express*, vol. 12, pp. 4080–4087, Aug. 2004. [Online]. Available: http://www.opticsinfobase.org/abstract.cfm?URI=oe-12-17-4080

[83] Y. L. Hoo, W. Jin, C. Shi, H. L. Ho, D. N. Wang, and S. C. Ruan, "Design and modeling of a photonic crystal fiber gas sensor," *Applied Optics*, vol. 42, pp. 3509–3515, June 2003.

[84] J. B. Jensen, L. H. Pedersen, P. E. Hoiby, L. B. Nielsen, T. P. Hansen, J. R. Folkenberg, J. Riishede, D. Noordegraaf, K. Nielsen, A. Carlsen, and A. Bjarklev, "Photonic crystal fiber based evanescent-wave sensor for detection of biomolecules in aqueous solutions," *Optics Letters*, vol. 29, pp. 1974–1976, Sept. 2004.

[85] F. M. Cox, A. Argyros, and M. C. Large, "Liquid-filled hollow core microstructured polymer optical fiber," *Optics Express*, vol. 14, pp. 4135–4140, Apr. 2006. [Online]. Available: http://www.opticsinfobase.org/abstract.cfm?URI=oe-14-9-4135

[86] Y. Fink, D. J. Ripin, S. Fan, C. Chen, J. D. Joannopoulos, and E. L. Thomas, "Guiding optical light in air using an all-dielectric structure," *IEEE/OSA Journal of Lightwave Technology*, vol. 17, pp. 2039–2041, Nov. 1999.

[87] S. G. Johnson, M. Ibanescu, M. Skorobogatiy, O. Weisberg, T. D. Engeness, M. Soljačič, S. A. Jacobs, J. D. Joannopoulos, and Y. Fink, "Low-loss asymptotically single-mode propagation in large-core OmniGuide fibers," *Optics Express*, vol. 9, pp. 748–779, Dec. 2001. [Online].

Available: http://www.opticsinfobase.org/abstract.cfm?URI=oe-9-13-748

[88] T. D. Engeness, M. Ibanescu, S. G. Johnson, O. Weisberg, M. Skorobogatiy, S. Jacobs, and Y.Fink, "Dispersion tailoring and compensation by modal interactions in OmniGuide fibers," *Optics Express*, vol. 11, pp. 1175–1196, May 2003. [Online]. Available: http://www.opticsinfobase.org/abstract.cfm?URI=oe-11-10-1175

[89] M. Skorobogatiy, "Efficient antiguiding of TE and TM polarizations in low-index core waveguides without the need for an omnidirectional reflector," *Optics Letters*, vol. 30, pp. 2991–2993, Nov. 2005.

[90] M. E. Likhachev, S. L. Semjonov, M. M. Bubnov, E. M. Dianov, V. F. Khopin, M. Yu. Salganskii, M. A. Gurjanov, A. N. Gurjanov, R. Jamier, P. Viale, S. Février, and J.-M. Blondy, "Development and study of Bragg fibres with a large mode field and low optical losses," *Quantum Electronics*, vol. 36, pp. 581–586, July 2006.

[91] P. Viale, S. Février, P. Leproux, Y. Jaouën, and A.-F. Obaton, "Modal properties of solid-core photonic bandgap fibers," *Photonics and Nanostructures - Fundamentals and Applications*, vol. 4, pp. 116–122, May 2006.

[92] E. Pone, C. Dubois, N. Gu, Y. Gao, A. Dupuis, F. Boismenu, S. Lacroix, and M. Skorobogatiy, "Drawing of the hollow all-polymer Bragg fibers," *Optics Express*, vol. 14, pp. 5838–5852, June 2006. [Online]. Available: http://www.opticsinfobase.org/abstract.cfm?URI=oe-14-13-5838

[93] M. Mignanelli, K. Wani, J. Ballato, S. Foulger, and P. Brown, "Polymer microstructured fibers by one-step extrusion," *Optics Express*, vol. 15, pp. 6183–6189, May 2007. [Online]. Available: http://www.opticsinfobase.org/abstract.cfm?URI=oe-14-13-5838

[94] A. Dupuis, N. Guo, B. Gauvreau, A. Hassani, E. Pone, F. Boismenu, and M. Skorobogatiy, "Guiding in the visible with "colorful" solid-core Bragg fibers," *Optics Letters*, vol. 32, pp. 2882–2884, Oct. 2007.

[95] M. Skorobogatiy and A. Dupuis, "Ferroelectric all-polymer hollow Bragg fibers for terahertz guidance," *Applied Physics Letters*, vol. 90, pp. 113 514–1–113 514–3, Mar. 2007.

[96] Y. Xu, A. Yariv, J. G. Fleming, and S. Lin, "Asymptotic analysis of silicon based Bragg fibers," *Optics Express*, vol. 11, pp. 1039–1049, May 2003. [Online]. Available: http://www.opticsinfobase.org/abstract.cfm?URI=oe-11-9-1039

[97] K. J. Rowland, S. Afshar, and T. M. Monro, "Reducing confinement loss in all-silica Bragg bandgap fibers," in *Proc. Optical Fiber Communications Conference OFC 2007*, Anaheim, California, USA, 2007, paper PDP41.

[98] H. Uranus and H.Hoekstra, "Modelling of microstructured waveguides using a finite-element-based vectorial mode solver with transparent boundary conditions," *Optics Express*, vol. 12, pp. 2795–2809, June 2004. [Online]. Available: http://www.opticsinfobase.org/abstract.cfm?URI=oe-12-12-2795

[99] L. Vincetti, F. Poli, and S. Selleri, "Confinement loss and nonlinearity analysis of air-guiding modified honeycomb photonic bandgap fiber," *IEEE Photonics Technology Letters*, vol. 18, pp. 508–510, Feb. 2006.

[100] N. Burani and J. Lægsgaard, "Perturbative modeling of Bragg-grating-based biosensors in photonic-crystal fibers," *Journal of Optical Society of America B*, vol. 22, pp. 2487–2493, Nov. 2005.

[101] R. Amezcua-Correa, N. G. Broderick, M. N. Petrovich, F. Poletti, and D. J. Richardson, "Optimizing the usable bandwidth and loss through core design in realistic hollow-core photonic bandgap fibers," *Optics Express*, vol. 14, pp. 7974–7985, Aug. 2006. [Online]. Available: http://www.opticsinfobase.org/abstract.cfm?URI=oe-14-17-7974

[102] L. Vincetti, D. Ferrarini, M. Zoboli, A. Cucinotta, F. Poli, and S. Selleri, "Leakage Losses in Photonic Band Fap Fibers," in *Proc. European Conference on Optical Communication ECOC 2003*, Rimini, Italy, Sept. 21–25, 2003.

[103] F. Poli, M. Foroni, D. Giovanelli, A. Cucinotta, S. Selleri, J. B. Jensen, J. Lægsgaard, A. Bjarklev, G. Vienne, C. Jakobsen, and J. Broeng, "Silica bridge impact on hollow-core Bragg fiber transmission properties," in *Proc. Optical Fiber Communications Conference OFC 2007*, Anaheim, California, USA, 2007, paper OML8.

[104] P. E. Hoiby, L. B. Nielsen, L. H. Pedersen, J. B. Jensen, A. Bjarklev, and T. P. Hansen, "Molecular immobilization and detection in a photonic crystal fiber," in *Optical Fibers and Sensors for Medical Applications IV*, I. Gannot, Ed. Proc. SPIE, 2004, vol. 5317, pp. 220–223.

[105] T. Sakamoto, S. Aozasa, and M. Shimizu, "Recent Progress on S-band Fiber Amplifiers," in *Proc. European Conference on Optical Communication ECOC 2002*, Copenhagen, Denmark, Sept. 8 –12, 2002, paper Doped Fiber Amplifiers 2.2.1.

[106] S. Aozasa, H. Masuda, H. Ono, T. Sakamoto, T. Kanamori, Y. Ohishi, and M. Shimizu, "1480-1510 nm-band Tm doped fiber amplifier (TDFA) with high power conversion efficiency of 42%," in *Proc. Optical Fiber Communications Conference OFC 2001*, Anaheim, California, USA, 2001, pp. PD1–1–PD1–3.

[107] A. Cucinotta, F. Poli, and S. Selleri, "Dual-Pumping Scheme for Efficient Thulium-Doped Tellurite Fiber Amplifiers," in *Proc. European Conference on Optical Communication ECOC 2003*, Rimini, Italy, Sept. 21–25, 2003.

[108] A. S. L. Gomes and S. R. Lüthi, "Dual-wavelength pumped TDFAs for S-band optical telecommunication - an evaluation," in *Proc. Optical Fiber Communications Conference OFC 2005*, Anaheim, California, USA, Mar. 6–11, 2005, paper JWA13.

[109] J. Bromage, J. C. Bouteiller, H. J. Thielen, K. Brar, J. H. Park, C. Headley, L. E. Nelson, Y. Qian, J. DeMarco, S. Stulz, L. Leng, and B. Z. B. J. Eggleton, "S-band all-Raman amplifiers for 40 $\times$ 10 Gb/s transmission over 6 $\times$ 100 km of non-zero dispersion fiber," in *Proc. Optical Fiber Communications Conference OFC 2001*, Anaheim, California, USA, 2001, pp. PD4–1–PD4–3.

[110] S. R. Lüthi, C. J. A. Bastos-Filho, M. B. Costa e Silva, J. F. Martins-Filho, and A. S. L. Gomes, "Single-Pump Raman/TDFA Hybrid Amplifier Covering the Entire S-Band," in *Proc. European Conference on Optical Communication ECOC 2004*, Stockholm, Sweden, Sept. 5–9, 2004, pp. 302–303.

[111] M. Kakui, M. Takagi, S. Endo, S. Ishikawa, and M. Shigematsu, "S-band optical amplification employing silica-based phosphorous/alumina-codoped EDF," in *Proc. Optical Fiber Communications Conference OFC 2004*, Anaheim, California, USA, 2004, paper FB3.

[112] H. Ono, M. Yamada, and M. Shimizu, "S-band Erbium-Doped Fiber Amplifiers With a Multistage Configuration - Design, Characterization, and Gain Tilt Compensation," *IEEE/OSA Journal of Lightwave Technology*, vol. 21, pp. 2240–2246, Oct. 2003.

[113] M. A. Arbore, "Application of fundamental-mode cutoff for novel amplifiers and lasers," in *Proc. Optical Fiber Communications Conference OFC 2005*, Anaheim, California, USA, Mar. 6–11, 2005, paper OFB4.

[114] M. A. Arbore, Y. Zhou, G. Keaton, and T. Kane, "34dB gain at 1500nm in S-band EDFA with distributed ASE suppression," in *Proc. European Conference on Optical Communication ECOC 2002*, Copenhagen, Denmark, Sept. 8 –12, 2002, paper Doped Fiber Amplifiers 2.2.2.

[115] M. A. Arbore, Y. Zhou, H. Thiele, J. Bromage, and L. Nelson, "S-band Erbium-doped Fiber Amplifiers for WDM Transmission Between 1488 and 1508 nm," in *Proc. Optical Fiber Communications Conference OFC 2003*, Atlanta, Georgia, USA, Mar. 23–28, 2003, paper FI5, pp. 374–376.

[116] C. H. Yeh, C. C. Lee, and S. Ch, "120-nm Bandwidth Erbium-Doped Fiber Amplifier in parallel Configuration," *IEEE Photonics Technology Letters*, vol. 16, pp. 1637–1639, July 2004.

[117] P. Vavassori, M. Foroni, F. Poli, A. Cucinotta, and S. Selleri, "S-band EDFA with ASE suppression induced by bending loss of depressed-cladding active fiber," in *Proc. Optical Amplifier and their Applications - OSA Topical Meeting OAA 2005*, Budapest, Hungary, Aug. 7–10, 2005.

[118] J. B. Rosolem, A. A. Juriollo, R. Arradi, A. D. Coral, J. C. R. F. Oliveira, and M. A. Romero, "All silica S-band double-pass erbium-doped fiber amplifier," *IEEE Photonics Technology Letters*, vol. 17, pp. 1399–1401, July 2005.

[119] K. Thyagarajan and C. Kakkar, "S-Band Single-Stage EDFA With 25-dB Gain Using Distributed ASE Suppression," *IEEE Photonics Technology Letters*, vol. 16, pp. 2448–2450, Nov. 2004.

[120] D. Marcuse, "Influence of curvature on the losses of doubly clad fiber," *Applied Optics*, vol. 21, pp. 4208–4213, Dec. 1982.

[121] A. Oguri, Y. Emori, and S. Namiki, "1 THz-step bandwidth upgrades in broadband Raman amplifier by adding pump laser diodes," in *Proc. Optical Fiber Communications Conference OFC 2003*, Atlanta, Georgia, USA, Mar. 23–28, 2003.

[122] M. Yamada, A. Mori, K. Kobayashi, H. Ono, T. Kanamori, K. Oikawa, Y. Nishida, and Y. Ohishi, "Gain-flattened tellurite-based EDFA with a flat amplification bandwidth of 76 nm," *IEEE Photonics Technology Letters*, vol. 10, pp. 1244–1246, Sept. 1998.

[123] H. Masuda, S. Kawai, and K. Aida, "Wideband erbium-doped fiber amplifiers with three-stage amplification," *Electronics Letters*, vol. 34, pp. 567–568, Mar. 1998.

[124] B. Min, H. Yoon, W. J. Lee, and N. Park, "Coupled structure for wideband EDFA with gain and noise figure improvement from C to L-band ASE injection," *IEEE Photonics Technology Letters*, vol. 12, pp. 480–482, May 2000.

[125] M. Yamada, H. Ono, T. Kanamori, S. Sudo, and Y. Ohishi, "Broadband and gain-flattened amplifier composed of a 1.55 μm-band and a 1.58 μm-band Er^{3+}-doped fiber amplifier in a parallel configuration," *Electronics Letters*, vol. 33, pp. 710–711, Apr. 1997.

[126] S. W. Harun, P. Poopalan, and H. Ahmad, "Gain enhancement in L-band EDFA through a double-pass technique," *IEEE Photonics Technology Letters*, vol. 14, pp. 296–297, Mar. 2002.

[127] M. Foroni, L. Ruggeri, F. Poli, P. Gaboardi, A. Cucinotta, S. Selleri, and P. Vavassori, "40 dB gain S-band depressed-cladding EDFA with double-pass configuration," in *Proc. Optical Fiber Communications Conference OFC 2006*, Anaheim, California, USA, Mar. 5–10, 2006, paper OWI37.

[128] Q. Mao and J. W. Y. Lit, "Multiwavelength Erbium-Doped Fiber Lasers With Active Overlapping Linear Cavities," *IEEE/OSA Journal of Lightwave Technology*, vol. 21, pp. 160–169, Jan. 2003.

[129] J. Chow, G. Town, B. Eggleton, M. Ibsen, K. Sugden, and I. Bennion, "Multiwavelength generation in an erbium doped fiber laser using in-fiber comb filters," *IEEE Photonics Technology Letters*, vol. 8, pp. 60–62, Jan. 1996.

[130] Z. G. Lu, F. G. Sun, G. Z. Xiao, and C. P. Grover, "A tunable multi-wavelength fiber ring laser for measuring polarization mode dispersion in optical fibers," *IEEE Photonics Technology Letters*, vol. 16, pp. 1280–1282, May 2004.

[131] X. P. Dong, L. Shenping, K. S. Chiang, M. N. Ng, and B. C. B. Chu, "Multiwavelength erbium-doped fibre laser based on a high-birefringence fibre loop mirror," *Electronics Letters*, vol. 36, pp. 1609–1610, Sept. 2000.

[132] J. Yang, S. C. Tjin, and N. Q. Ngo, "Multiwavelength tunable fiber ring laser based on sampled chirp fiber Bragg grating," *IEEE Photonics Technology Letters*, vol. 16, pp. 1026–1028, Apr. 2004.

[133] P. C. Peng, H. Y. Tseng, and S. Chi, "A tunable dual-wavelength erbium-doped fiber ring laser using a self-seeded Fabry-Pérot laser diode," *IEEE Photonics Technology Letters*, vol. 15, pp. 661–663, May 2003.

[134] F. Poli, M. Foroni, A. Cucinotta, L. Ruggeri, L. Rosa, S. Selleri, , and P. Vavassori, "Tunability of the Gain Spectrum in an Erbium-Doped Fiber with Depressed-Cladding," in *Proc. Optical Fiber Communications Conference OFC 2006*, Anaheim, California, USA, Mar. 5–10, 2006, paper OWI23.

[135] C. C. Lee, Y. K. Chen, and S. K. Liaw, "Single-longitudinal-mode fiber laser with a passive multiple-ring cavity and its application for video transmission," *Optics Letters*, vol. 23, pp. 358–360, Mar. 1998.

[136] H. Chen, "Dynamics of widely tunable single-frequency semiconductor fiber ring laser," *Physics Letters A*, vol. 320, pp. 333–337, Jan. 2004.

[137] M. J. Guy, J. R. Taylor, and R. Kashyap, "Single-frequency erbium fibre ring laser with intracavity phase-shifted fibre Bragg grating narrowband filter," *Electronics Letters*, vol. 31, pp. 1924–1925, Oct. 1995.

[138] Y. Cheng, J. T. Kringlebotn, W. H. Loh, R. I. Laming, and D. N. Payne, "Stable single-frequency traveling-wave fiber loop laser with integral saturable-absorber-based tracking narrow-band filter," *Optics Letters*, vol. 20, pp. 875–877, Apr. 1995.

[139] C. S. Kim, F. Farokhrooz, U. Sharma, R. M. Sova, and J. U. Kang, "Wavelength-switching single-longitudinal-mode fiber ring laser based on cascaded composite Sagnac loop filters," in *Proc. Optical Fiber Communications Conference OFC 2004*, Anaheim, California, USA, 2004, paper ThB6.

[140] H. Chen, F. Babin, M. Leblanc, and G. W. Schinn, "Widely tunable single-frequency erbium-doped fiber lasers," *IEEE Photonics Technology Letters*, vol. 15, pp. 185–187, Feb. 2003.

[141] Y. W. Song, S. A. Havstad, D. Starodubov, Y. Xie, A. E. Willner, and J. Feinberg, "40-nm-wide tunable fiber ring laser with single-mode operation using a highly stretchable FBG," *IEEE Photonics Technology Letters*, vol. 13, pp. 1167–1169, Nov. 2001.

[142] R. J. Mears, L. Reekie, I. M. Jauncey, and D. N. Payne, "Low-noise erbium-doped fiber amplifier operating at 1.54 μm," *Electronics Letters*, vol. 23, pp. 1026–1028, Sept. 1987.

[143] E. Desurvire, *Erbium-Doped Fiber Amplifiers*. New York: Wiley, 1994.

[144] M. J. F. Digonnet, *Ed. Rare Earth Doped Fiber Lasers and Amplifiers*. New York: Marcel Dekker, 1993.

[145] D. C. Hanna, R. M. Percival, I. R. Perry, R. G. Smart, P. J. Suni, J. E. Townsend, and A. C. Troppe, "Continuous-wave oscillation of a monomode ytterbium-doped fiber laser," *Electronics Letters*, vol. 24, pp. 1111–1113, Aug. 1988.

[146] D. C. Hanna, R. M. Percival, I. R. Perry, R. G. Smart, P. J. Suni, and A. C. Tropper, "An ytterbium-doped monomode fiber laser: broadband tunable operation from 1.010 μm to 1.162 μm," *Journal of Modern Optics*, vol. 37, pp. 517–525, 1990.

[147] J. C. Mackechnie, W. L. Barnes, D. C. Hanna, and J. E. Townsend, "High power ytterbium (Yb^{3+})-doped fiber laser operating in the 1.12 μm region," *Electronics Letters*, vol. 29, pp. 52–53, Jan. 1993.

[148] J. Y. Allain, M. Monerie, H. Poignant, and T. Georges, "High-efficiency ytterbium-doped fluoride fibre laser," *Journal of Non-Crystalline Solids*, vol. 161, pp. 270–273, Aug. 1993.

[149] S. Magne, M. Druetta, J. P. Goure, J. C. Thevenin, P. Ferdinand, and G. Monnom, "An ytterbium-doped monomode fiber laser: amplified spontaneous emission, modeling of the gain and tunability in an external cavity," *Journal of Luminescence*, vol. 60-61, pp. 647–650, Apr. 1993.

[150] H. M. Pask, R. J. Carman, D. C. Hanna, A. C. Tropper, C. J. Mackechnie, P. R. Barber, and J. M. Dawes, "Ytterbium-doped silica fiber lasers: versatile sources for the 1-1.2 μm region," *IEEE Journal of Selected Topics in Quantum Electronics*, vol. 1, pp. 2–13, Apr. 1995.

[151] R. Paschotta, D. C. Hanna, P. DeNatale, G. Modugno, M. Inguscio, and P. Laporta, "Power amplifier for 1083 nm using ytterbium doped fiber," *Optics Communications*, vol. 136, pp. 243–246, Mar. 1997.

[152] V. Cautaerts, D. J. Richardson, R. Paschotta, and D. C. Hanna, "Stretched pulse Yb^{3+} silica fiber laser," *Optics Letters*, vol. 22, pp. 316–318, Mar. 1997.

[153] H. Takebe, T. Murata, and K. Morinaga, "Compositional dependence of absorption and fluorescence of Yb^{3+} in oxide glasses," *Journal of the American Ceramic Society*, vol. 79, pp. 681–687, 1996.

[154] M. J. Weber, J. E. Lynch, D. H. Blackburn, and D. J. Cronin, "Dependence of the stimulated emission cross section of Yb^{3+} on host glass composition," *IEEE Journal of Quantum Electronics*, vol. 19, pp. 1600–1608, Oct. 1983.

[155] M. M. Broer, D. M. Krol, and D. J. DiGiovanni, "Highly nonlinear near-resonant photodarkening in a thulium-doped aluminosilicate glass fiber," *Optics Letters*, vol. 18, pp. 799–801, May 1993.

[156] M. M. Broer, R. L. Cone, and J. R. Simpson, "Ultraviolet-induced distributed-feedback gratings in Ce^{3+}-doped silica optical fibers," *Optics Letters*, vol. 16, pp. 1391–1393, Sept. 1991.

[157] E. G. Behrens, R. C. Powell, and D. H. Blackburn, "Characteristics of laser-induced gratings in Pr^{3+}- and Eu^{3+}-doped silicate glasses," *Journal of Optical Society of America B*, vol. 7, pp. 1437–1444, Aug. 1990.

[158] R. Paschotta, J. Nilsson, P. R. Barber, J. E. Caplen, A. C. Tropper, and D. C. Hanna, "Lifetime quenching in Yb-doped fibres," *Optics Communications*, vol. 136, pp. 375–378, Apr. 1997.

[159] J. J. Koponen, M. J. Sderlund, S. K. T. Tammela, and H. Po, "Photodarkening in ytterbium-doped silica fibers," in *Proc. SPIE Europe Symposium Optics/Photonics in Security and Defence 2005*, 2005.

[160] J. J. Koponen, M. J. Soderlund, H. J. Hoffman, and S. K. T. Tammela, "Measuring photodarkening from single-mode ytterbium doped silica fibers," *Optics Express*, vol. 14, pp. 11 539–11 544, Nov. 2006. [Online]. Available: http://www.opticsinfobase.org/abstract.cfm?URI=oe-14-24-11539

[161] Y. Jeong, J. Sahu, D. N. Payne, and J. Nilsson, "Ytterbium-doped large-core fiber laser with 1.36 kW continuous-wave output power," *Optics Express*, vol. 12, pp. 6088–6092, Dec. 2004. [Online]. Available: http://www.opticsinfobase.org/abstract.cfm?URI=oe-12-25-6088

[162] V. Reichel, K. W. Moerl, S. Unger, S. Jetschke, H. R. Mueller, J. Kirchof, T. Sandrock, A. Harschack, A. Liem, J. Limpert, H. Zellmer, and A. Tuennermann, "Fiber-laser power scaling beyond the 1-kilowatt level by Nd:Yb co-doping," in *XV International Symposium on Gas Flow, Chemical Lasers, and High-Power Lasers*, J. Kodymova, Ed. Proc. SPIE, 2005, vol. 5777, pp. 404–407.

[163] *Technical papers.* [Online]. Available: http://www.ipgphotonics.com/

[164] G. P. Agrawal, *Nonlinear Fiber Optics.* New York: Academic, 2001.

[165] D. Cotter, "Stimulated Brillouin Scattering in monomode optical fiber," *Journal of Optical Communications*, vol. 4, pp. 10–19, 1983.

[166] A. Liem, J. Limpert, H. Zellmer, and A. Tnnermann, "100-W single-frequency master-oscillator fiber power amplifier," *Optics Letters*, vol. 28, pp. 1537–1539, Sept. 2003.

[167] D. N. Payne, Y. Jeong, J. Nilsson, J. K. Sahu, D. B. S. Soh, C. Alegria, P. Dupriez, C. A. Codemard, V. N. Philippov, V. Hernandez, R. Horley, L. Hickey, L. Wanzcyk, C. E. Chryssou, J. A. Alvarez-Chavez, and P. W. Turner, "Kilowatt-class single-frequency fiber sources," in *Fiber Lasers II: Technology, Systems, and Applications*, L. N. Durvasula, A. J. W.Brown, and J. Nilsson, Eds. Proc. SPIE, 2005, vol. 5709, pp. 133–141.

[168] Y. Wang, C.-Q. Xu, and H. Po, "Thermal effects in kilowatt fiber lasers," *IEEE Photonics Technology Letters*, vol. 16, pp. 63–65, Jan. 2004.

[169] S. Gray, D. Walton, J. Wang, A. Liu, M. J. Li, X. Chen, A. B. Ruffin, J. DeMeritt, and L. Zenteno, "Suppression of Stimulated Brillouin Scattering in High Power, Narrow Linewidth Fiber Amplifiers," in *Proc. Nonlinear Optics: Materials, Fundamentals and Applications NLO 2007*, 2007, paper WB2.

[170] E. Snitzer, H. Po, F. Hakimi, R. Tumminelli, and B. C. McCollum, "Double-clad offset core Nd fiber laser," in *Optical Fiber Sensors - OSA Technical Digest Serie*. Optical Society of America, 1988, vol. 2.

[171] B. Culshaw, "Optical Fiber Sensor Technologies: Opportunities and - Perhaps - Pitfalls," *IEEE/OSA Journal of Lightwave Technology*, vol. 22, pp. 39–50, Jan. 2004.

[172] A. D. Kersey and A. Dandridge, "Applications of Fiber-Optic Sensors," *IEEE Transactions on Components, Hybrids and Manufacturing Technology*, vol. 13, pp. 137–143, Mar. 1990.

[173] J. Zubia and J. Arrue, "Plastic Optical Fibers: An Introduction to Their Technological Processes and Applications," *Optical Fiber Technology*, vol. 7, pp. 101–140, Apr. 2001.

[174] D. Kalymnios, "Plastic optical fibres (POF) in sensing: current status and prospects," in *17th International Conference on Optical Fibre Sensors*, M. Voet, R. Willsch, W. Ecke, J. Jones, and B. Culshaw, Eds. Proc. SPIE, 2005, vol. 5855, pp. 1–4.

[175] I. A. S. de Oliveira and M. Bonfim, "Plastic Optical Fibers in Telecommunications: Analysis, Comparison and Applications," in *Proc.*

SBMO/IEEE MTT-S International IMOC 2003, Foz do Iguacu, Brazil, Sept. 20–23, 2003.

[176] J. J. Bayle and J. Mateo, “Plastic optical fiber sensor of refractive index, based on evanescent field,” in *Proc. Fifth International Conference on Plastic Optical Fibres and Applications POF 1996*, Paris, France, Oct. 22–24, 1996, pp. 220–227.

[177] M. Lomer, J. Zobia, O. M. Conde, J. Mirapeix, A. M. Qubillas, and J. M. Lopes-Higuera, “In situ refraction index of liquid measurement using polymer optical fibers,” in *Second European Workshop on Optical Fibre Sensors*, J. M. Lopez-Higuera and B. Culshaw, Eds. Proc. SPIE, 2004, vol. 5502, pp. 325–328.

[178] N. Ioannides, D. Kalymnios, and I. W. Rogers, “An optimised plastic optical fiber (POF) displacement sensor,” in *Proc. Fifth International Conference on Plastic Optical Fibres and Applications POF 1996*, Paris, France, Oct. 22–24, 1996, pp. 251–255.

[179] M. Meribout, M. Habli, A. Al-Naamany, and K. Al-Busaid, “A new ultrasonic-based device for accurate measurement of oil, emulsion, and water levels in oil tanks,” in *Proc. Instrumentation and Measurement Technology Conference IMTC 2004*, Como, Italy, May 18–20, 2004, pp. 1942–1947.

[180] M. Weiss and R. Knochel, “A sub-millimeter accurate microwave multilevel gauging system for liquids in tanks,” *IEEE Transactions on Microwave Theory and Techniques*, vol. 49, pp. 381–384, Feb. 2001.

[181] C. P. Yakymyshyn and C. R. Pollock, “Differential Absorption Fiber-Optic Liquid Level Sensor,” *IEEE/OSA Journal of Lightwave Technology*, vol. LT-5, pp. 941–946, 1987.

[182] K. Iwamoto and I. Kamata, “Liquid-level sensor with optical fibers,” *Applied Optics*, vol. 31, pp. 51–54, Jan. 1992.

[183] A. Wang, M. F. Gunber, K. A. Murphy, and R. O. Claus, “Fiber-optic liquid-level sensor,” *Sensors and Actuators A: Physical*, vol. 35, pp. 161–164, Dec. 1992.

[184] G. Betta, L. Ippolito, A. Pietrosanto, and A. Scaglione, "An optical fiber-based technique for continuous-level sensing," *IEEE Transactions on Instrumentation and Measurement*, vol. 44, pp. 686–689, June 1995.

[185] P. Raatikainen, I. Kassamakov, R. Kakanakov, and M. Lukkala, "Fiber-optic liquid-level sensor," *Sensors and Actuators A: Physical*, vol. 58, pp. 93–97, Feb. 1997.

[186] I. K. Ilev and R. W. Waynant, "Selective detection of labeled DNA using an air-clad photonic crystal fiber," in *Proc. Conference on Lasers and Electro-Optics CLEO 1999*, Baltimore, Maryland, USA, May 18–23, 1999, pp. 157–158.

[187] S. Khaliq, S. W. James, and R. P. Tatam, "Fiber-optic liquid-level sensor using a long-period grating," *Optics Letters*, vol. 26, pp. 1224–1226, Aug. 2001.

[188] J. D. Weiss, "The pressure approach to fiber liquid level sensors," in *Proc. Fifth International Conference on Plastic Optical Fibres and Applications POF 1995*, Boston, MA, USA, Oct. 17–19, 1995, pp. 167–170.

[189] S. Vargas, C. Vázquez, A. B. Gonzalo, and J. M. S. Pena, "A plastic fiber-optic liquid level sensor," in *Second European Workshop on Optical Fibre Sensors*, J. M. Lopez-Higuera and B. Culshaw, Eds. Proc. SPIE, 2004, vol. 5502, pp. 148–151.

[190] C. Vázquez, A. B. Ponzalo, S. Vargas, and J. Montalvo, "Multi-sensor system using plastic optical fibers for intrinsically safe level measurements," *Sensors and Actuators A: Physical*, vol. 116, pp. 22–32, Oct. 2004.

[191] T. M. Monro, D. J. Richardson, N. G. R. Broderick, and P. J. Bennett, "Modeling Large Air Fraction Holey Optical Fibers," *IEEE/OSA Journal of Lightwave Technology*, vol. 18, pp. 50–56, Jan. 2000.

[192] S. Selleri, L. Vincetti, A. Cucinotta, and M. Zoboli, "Complex FEM modal solver of optical waveguides with PML boundary conditions," *Optical and Quantum Electronics*, vol. 33, pp. 359–371, Apr. 2001.

[193] A. Cucinotta, G. Pelosi, S. Selleri, L. Vincetti, and M. Zoboli, "Perfectly Matched Anisotropic Layers for Optical Waveguides Analysis through

the Finite Element Beam Propagation Method," *Microwave and Optical Technology Letters*, vol. 23, pp. 67–69, Oct. 1999.

[194] F. Poli, A. Cucinotta, M. Fuochi, S. Selleri, and L. Vincetti, "Characterization of microstructured optical fibers for wideband dispersion compensation," *Journal of Optical Society of America A*, vol. 20, pp. 1958–1962, Oct. 2003.

[195] A. Cucinotta, S. Selleri, L. Vincetti, and M. Zoboli, "Holey Fiber Analysis Through the Finite-Element Method," *IEEE Photonics Technology Letters*, vol. 14, pp. 1530–1532, Nov. 2002.

[196] F. Poli, A. Cucinotta, S. Selleri, and A. H. Bouk, "Tailoring of flattened dispersion in highly nonlinear photonic crystal fibers," *IEEE Photonics Technology Letters*, vol. 16, pp. 1065–1067, Apr. 2004.

[197] A. Cucinotta, S. Selleri, L. Vincetti, and M. Zoboli, "Perturbation Analysis of Dispersion Properties in Photonic Crystal Fibers Through the Finite Element Method," *IEEE/OSA Journal of Lightwave Technology*, vol. 20, pp. 1433–1442, Aug. 2002.

[198] A. Cucinotta, F. Poli, and S. Selleri, "Design of Erbium-doped Triangular Photonic Crystal Fiber Based Amplifiers," *IEEE Photonics Technology Letters*, vol. 16, pp. 2027–2029, Sept. 2004.

[199] F. Poli, F. Adami, M. Foroni, L. Rosa, A. Cucinotta, and S. Selleri, "Optical parametric amplification in all-silica triangular-core photonic crystal fibers," *Applied Physics B*, vol. 81, pp. 251–255, July 2005.

[200] M. Fuochi, F. Poli, S. Selleri, A. Cucinotta, and L. Vincetti, "Study of Raman Amplification Properties in Triangular Photonic Crystal Fibers," *IEEE/OSA Journal of Lightwave Technology*, vol. 21, pp. 2247–2254, July 2003.

[201] M. Bottacini, F. Poli, A. Cucinotta, and S. Selleri, "Modeling of Photonic Crystal Fiber Raman Amplifiers," *IEEE/OSA Journal of Lightwave Technology*, vol. 22, pp. 1707–1713, July 2004.

[202] S. Selleri and M. Zoboli, "Performance Comparison of Finite Element Approaches for Electromagnetic Waveguides," *Journal of Optical Society of America A*, vol. 14, pp. 1460–1466, July 1997.

[203] S. Selleri and J. Petracek, "Modal analysis of rib waveguide through finite element and mode matching methods," *Optical and Quantum Electronics*, vol. 33, pp. 373–386, Apr. 2001.